JETP Letters, Vol. 76, No. 7, 2002, pp. 409–413. From Pis'ma v Zhurnal Éksperimental'noĭ i Teoreticheskoĭ Fiziki, Vol. 76, No. 7, 2002, pp. 483–487.

Search for Neutrino Radiative Decay with a Prototype Borexino Detector¶

A. V. Derbin[1] and O. Ju. Smirnov[2]

[1] *St. Petersburg Nuclear Physics Institute, Russian Academy of Sciences, Gatchina, Leningrad region, 188350 Russia*
e-mail: derbin@lngs.infn.it

[2] *Joint Institute for Nuclear Research, Dubna, Moscow region, 141980 Russia*
e-mail: smirnov@lngs.infn.it

Received July 16, 2002; in final form, August 22, 2002

Results of background measurements with a prototype of the Borexino detector were used to obtain bounds on the lifetime of radiative neutrino decay $\nu_H \longrightarrow \nu_L + \gamma$. The new lower limit for the lifetime of *pp* and ^{7}Be neutrinos is $\tau_{c.m.}(\nu_H \longrightarrow \nu_L + \gamma)/m_\nu \geq 4.2 \times 10^3$ s eV^{-1} ($\alpha = 0$). It is more than an order of magnitude stronger than the value obtained in previous experiments using nuclear reactors and accelerators. © *2002 MAIK "Nauka/Interperiodica"*.

PACS numbers: 13.15.+g; 14.60.Pq

1. If neutrinos have mass, then a heavier neutrino may decay to the lighter one $\nu_H \longrightarrow \nu_L + \gamma$. In the Standard model (SM), the lifetime of a neutrino expressed in terms of the transition magnetic moment μ_{HL}^{tr} is [1–4]:

$$\tau[\text{s}] \approx 0.19\left(\frac{\mu_B}{\mu_{HL}^{tr}}\right)^2\left(\frac{m_{\nu_H}^2}{m_{\nu_H}^2 - m_{\nu_L}^2}\right)\left(\frac{1eV}{m_{\nu_H}}\right)^3, \qquad (1)$$

where μ_{HL}^{tr} is in Bohr magneton (μ_B) units. The probability of radiative decay in SM is very low. If the neutrino transition moment μ_{HL}^{tr} has a value close to that expected for a diagonal magnetic moment $\mu_\nu \approx 3.2 \times 10^{-19}(m_\nu/1\text{ eV})\mu_B$, then from Eq. (1) the lifetime of a neutrino is $\tau \sim 10^{29}$ years. At the same time, the reasons (the same as for a right boson) that lead to a large magnetic moment also lead to an increase in the probability of radiative neutrino decay [5–9].

The radiative decay of reactor antineutrinos $\bar{\nu}_e$ was studied in [10–14]; the latter gives the best lower limit of $\tau_{c.m}/m_\nu \geq 200$ s eV^{-1} (90% c.l.) for the lifetime. A search for the ν_μ and $\bar{\nu}_\mu$ decays was performed in high-intensity neutrino beams from π^+ and μ^+ decaying at rest; the lifetime of the muon (anti)neutrino was bounded as $\tau_{c.m}/m_{\nu_\mu} \geq 15.4$ s eV^{-1} [15]. A much more restrictive limit was obtained from the solar γ-ray flux, $\tau_{c.m}/m_{\nu_e} \geq 7 \times 10^9$ s eV^{-1} [16]. The astrophysical limits are even stronger and lie in the region 10^9–10^{20} s/eV (see [17–19] and references therein).

In this paper, we present the results of the search for neutrino radiative decay with a prototype of the Borexino detector.

2. Experimental setup and results of measurements. Borexino, a real-time detector for low-energy neutrino spectroscopy, is near completion in the underground laboratory at Gran Sasso (see [20] and references therein). The main goal of the detector is a direct measurement of the flux of ^{7}Be solar neutrinos of all flavors via neutrino–electron scattering in an ultrapure liquid scintillator.

The prototype of the Borexino detector—Counting Test Facility (CTF)—was constructed to test the key concept of Borexino, namely, the possibility to purify a large mass of liquid scintillator at the level of contamination for U and Th of a few units of 10^{-16} g/g. As a simplified scaled version of the Borexino detector, a volume of liquid scintillator is contained in a 2-m-diameter transparent inner nylon vessel mounted at the center of an open structure that supports 100 phototubes (PMT) [21]. The whole system is placed within a cylindrical tank (11 m in diameter and 10 m height) that contains 1000 tons of ultrapure water, which provides a 4.5-m shielding against neutrons originating from the rock and against external γ rays from PMTs and other construction materials. Detailed reports on the CTF have been published [20–25].

The energy of an event in the CTF detector is defined using the total collected charge from all PMTs. The coefficient linking the event energy and the total collected charge is called light yield (or photoelectron yield). The light yield for the electrons can be considered linear with respect to its energy only for energies above 1 MeV. At lower energies, the phenomenon of

¶This article was submitted by the authors in English.

"ionization quenching" violates the linear dependence of the light yield on energy [26]. The deviations from the linear law can be taken into account by the ionization deficit function $f(k_B, E)$, where k_B depends on the scintillator properties. The total collected charge in this equals $Q \sim Ef(k_B, E)$.

Because of the nonlinear dependence of the light yield on the energy released due to the ionization-quenching effect, the CTF resolution should be expressed in terms of the total registered charge, which is directly measured in the experiment.

A study with radioactive sources placed at different positions inside the CTF inner vessel showed that the CTF response can be approximated by a Gaussian, with sigma defined by the following formula:

$$\sigma_Q = \sqrt{(1 + \overline{\nu_1})Q + \nu_p Q^2}, \qquad (2)$$

where $Q = AEf(k_B, E)\nu_f$ is the mean total registered charge for events of energy E distributed over the detector's volume; ν_1 is the relative variance of the PMT single photoelectron charge spectrum ($\overline{\nu_1} = 0.34$); A is the scintillator specific light yield measured in photoelectrons per MeV ($A = 350$ p.e/MeV is CTF-2 for the event at the detector's center); and ν_f is the volume factor, coming from the averaging of the signals over the CTF volume. The parameters $\nu_p = 0.0023$ and $\nu_f = 1.005$ give additional signal variance for the source distributed over the detector's volume in comparison to the point-like source at the detector's center. The last case will naturally yield $\nu_p = 0$ and $\nu_f = 1$. All the parameters in (2) were defined with satisfactory precision from the CTF-II data (see [27, 28] for the details). For estimates of the energy resolution, one can use the approximation $\sigma_E/E \approx \sigma_Q/Q$.

The experimental spectra of the CTF-II setup in the energy region up to 450 keV accumulated during 32.1 days of measurements are shown in Fig. 1. The spectrum without any cuts is shown on the top. The next distribution is obtained with the muon veto, which suppressed the background rate only 25% in this energy region. Time-correlated events (occurring in the time window $\Delta t \leq 8$ ms) and events with reconstructed radius $r \geq 100$ cm (i.e., outside of the inner vessel) were also removed. Additional α/β discrimination was applied to eliminate contribution from α particles. The remaining background rate at 300 keV of 0.05 counts/keV kg yr is the lowest value achieved at any large-scale low-background installation.

The major part of the remaining background in the energy region up to 200 keV is induced by the β activity of ^{14}C. Another source of background is the soft part of the spectra of β and γ coming from the decay of ^{40}K present in construction materials (decays occur out of the scintillator volume).

The β decay of ^{14}C is an allowed ground-state to ground-state ($0^+ \longrightarrow 1^+$) Gamow–Teller transition with an endpoint energy of $E_0 = 156$ keV and half life of 5730 years. Deviations from the allowed shape of the ^{14}C spectrum are usually parametrized as $C(E) = 1 + \alpha E$. Although the β decay of ^{14}C was investigated by many groups over almost 50 years, the situation with the shape factor is still unclear [29]; we leave this parameter free in our estimations.

The model function for the remaining background was selected as the sum of the ^{14}C spectrum and a first-order polynomial for the underlying background,

$$S^{\text{Model}}(Q) = N_0 S^{\beta}(Q, \{A, k_B, \alpha\}) + a + bQ, \qquad (3)$$

with six free parameters: N_0 is the number of ^{14}C decays; A is the scintillator light yield; k_B is the quenching factor; α is the ^{14}C shape factor; and a, b are the parameters describing the linear underlying part of the residual spectrum.

The end-point energy of the ^{14}C spectrum was defined in other experiments with high accuracy, $E_0 = (156 \pm 0.5)$ keV, and is fixed in the calculations.

In any case, this parameter is in strong correlation with the parameter A, and its uncertainty is masked by the uncertainty in the parameter A. The maximum-likelihood method was used to find the best values of the free parameters of the model function. A good agreement of the proposed model with the experimental data in the energy region 138–380 keV was obtained ($\chi^2 = 205/214$).

3. Analysis. The analysis is performed with the assumptions that the decaying neutrino ν_H is dominantly coupled to the electron ($U_{eH} \approx 1$), and in the final state ν_L the neutrino mass is vanishing (i.e., $m_{\nu_L} \ll m_{\nu_H}$). The expected laboratory gamma spectrum is defined by a photon moment distribution in the center-of-mass system. For the common case, one can write the photon angular distribution in the general form [11]:

$$dN = \frac{1}{2}(1 + \alpha\cos(\theta))d\cos(\theta). \qquad (4)$$

The anisotropy parameter α defines the angular distribution of the photon relative to the spin of the decaying neutrino in the neutrino rest frame and is related to the space–time structure of the decay vertex. For the Majorana neutrino, α is identically zero ($\alpha = 0$) but can take on any value $-1 \leq \alpha \leq 1$ for the Dirac neutrino. With the assumption of total parity violation, the generated left (right)-handed Dirac neutrinos correspond to the case $\alpha = -1(+1)$. The lab-frame energy of the decay gamma E_γ in terms of the lab-frame energy of the neutrino E_ν and the center-of-mass angle θ is

$$E_\gamma = \frac{E_\nu}{2}\left(1 + \frac{P_\nu}{E_\nu}\cos(\theta)\right). \qquad (5)$$

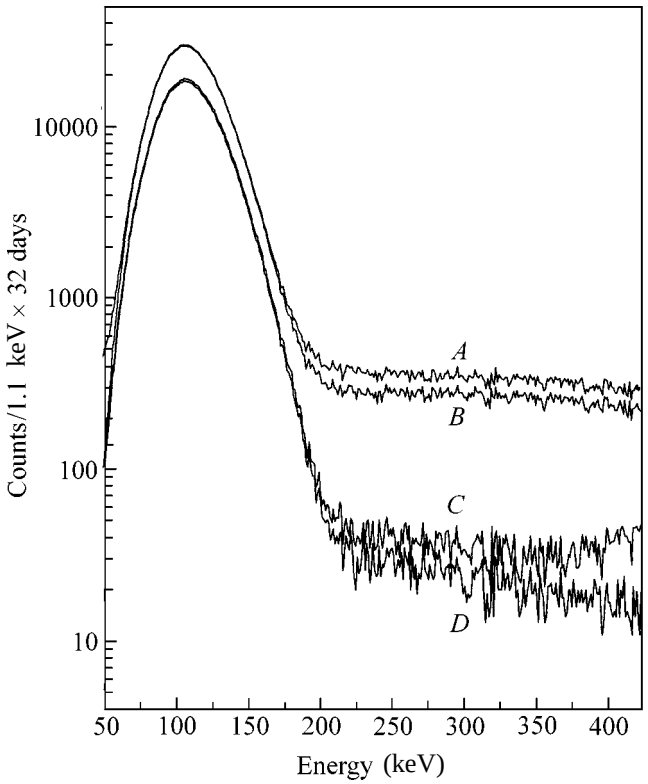

Fig. 1. CTF-II background in the low-energy region and the result of the sequential cuts applied in order to reduce the background: *A*) raw data; *B*) unions cut; *C*) radial cut (with 100 cm radius); *D*) α/β discrimination.

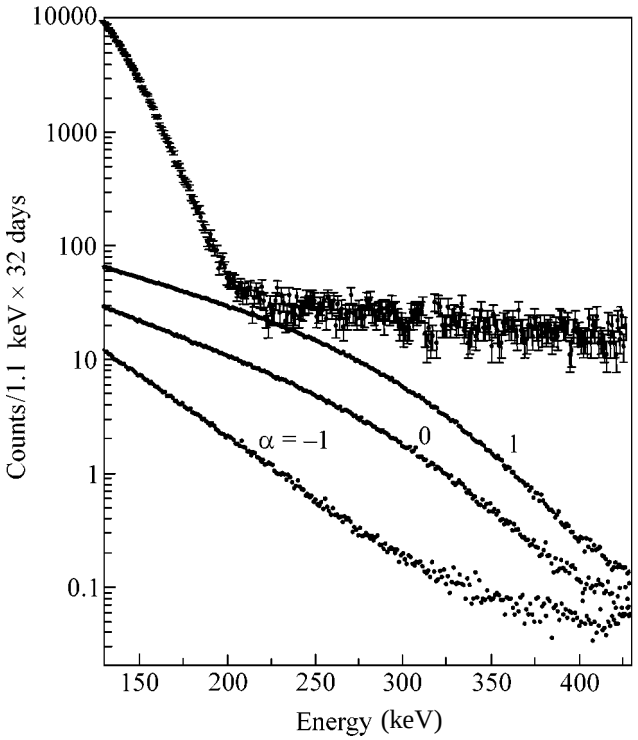

Fig. 2. The experimental spectrum measured by CTF-II (upper plot with error bars) and the expected energy spectra from gammas appearing in radiative decay of the neutrino $\nu_H \longrightarrow \nu_L + \gamma$ calculated by the M-C method with $\tau_{c.m.}/m_\nu = 5.0 \times 10^3$ s eV^{-1} for 3 values of the parameter.

After relativistic time dilation one obtains the gamma energy spectrum E_γ due to the decay of the neutrino with energy E_ν:

$$\frac{dN}{dE_\gamma}(E_\gamma, E_\nu) = \frac{m_\nu}{\tau_{c.m.}}\frac{1}{E_\nu^2}\left(1 - \alpha + 2\alpha\frac{E_\gamma}{E_\nu}\right), \qquad (6)$$

where $\tau_{c.m.}$ represents the center-of-mass neutrino lifetime. Taking into account the solar neutrino energy spectrum $\phi_\nu(E_\nu)$, one can write the expected gamma spectrum in the detector as

$$\frac{dN}{dE_\gamma}(E_\gamma) = \frac{VT}{c}\int_{E_\gamma}^{E_{\nu_{max}}}\frac{dN}{dE_\gamma}(E_\gamma, E_\nu)\phi_\nu(E_\nu)dE_\nu, \qquad (7)$$

where V is detector volume, T is the time of measurement, and c is the speed of light in vacuum.

In the calculations, we used the neutrino fluxes given by the standard solar model (SSM)[30] and the neutrino energy spectra from [31]. Signal shapes (7) were convolved with the detector response function:

$$S(Q) = \int\frac{dN}{dT_e}(T_e(Q'))\frac{dT_e}{dQ}\mathrm{Res}(Q, Q')dQ', \qquad (8)$$

where Res(Q, Q') is the detector response function and σ_Q is defined by (2).

The Monte-Carlo method was used in order to simulate the CTF response to gammas. The events were generated according to the spectrum given by Eq. (7) inside the inner vessel and in the adjacent water layer of 50 cm. The gamma-electron showers were followed using the EGS-4 code [32]. As soon as an electron of energy E_e appears inside the scintillator, the corresponding charge is added to the running sum, taking into account the quenching factor and the dependence of the registered charge on the distance from the detector's center. The obtained results for different a values are shown in Fig. 2.

Taking into account the best ratio of the expected effect to background and in order to avoid systematic errors caused by the uncertainty of the linear part of the background at lower energies, the range 185–380 keV was chosen for the analysis. The maximum-likelihood method was used to find the possible contribution from the radiative decay of the SSM solar neutrino in the measured spectrum. The likelihood function was found with the assumption that the number of counts in each channel of the measured spectrum S_i^{exp} obeys a normal distribution and represents the sum of the model func-

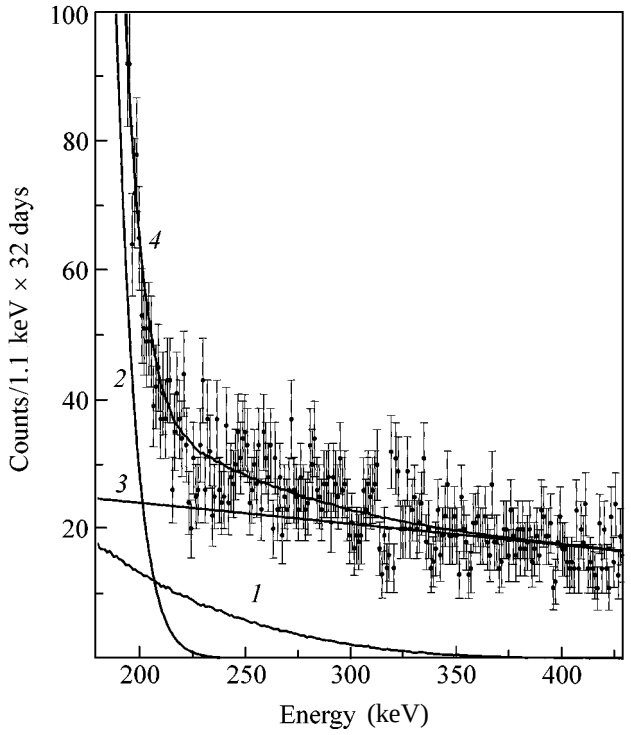

Fig. 3. The fit in the region 185–380 keV for radiative neutrino decay: (*1*) M-C calculation of the gamma spectrum from $\nu_H \longrightarrow \nu_L + \gamma$ decay with $\tau_{c.m.}/m_\nu = 4.2 \times 10^3$ s eV^{-1} ($\alpha = 0$); (*2*) ^{14}C β-spectrum; (*3*) linear background; (*4*) total fit.

tion describing the residual background (3) and the spectrum due to the neutrino decay calculated using Eqs. (6)–(8).

The A, k_B, and α parameters were fixed in the analysis at the values found during the data fitting in the wider region 138–380 keV with better statistics. The other three parameters were free. The changes in α and k_B practically do not influence the results of the analysis. The parameter A was also estimated independently from the measurements with a radon source.

The analysis of the upper limit on the lifetime of the neutrino was performed in the following way. First, we minimized the $\chi^2(N_0, a, b, \tau_{c.m.}/m_\nu)$ value for different values of $\tau_{c.m.}/m_\nu$. The integration of the probability function gives a value of 0.9 (90% c.l.) for $\tau_{c.m.}/m_\nu = 4.2 \times 10^3$ s eV^{-1} ($\alpha = 0$). This limit is practically independent of the lower bound of the analyzed region. The results of the optimal fit for value $\tau_{c.m.}/m_\nu = 4.2 \times 10^3$ s eV^{-1} ($\alpha = 0$) are shown in Fig. 3. In the same way, the upper limits $\tau_{c.m.}/m_\nu \geq 1.5 \times 10^3$ s eV^{-1} ($\alpha = -1$) and $\tau_{c.m.}/m_\nu \geq 9.7 \times 10^3$ s eV^{-1} ($\alpha = 1$) were obtained. Actually, the analysis of the CTF-II gives a 25% limit on the part of the background in the region 200–250 keV attributed to possible neutrino decay. The low sensitivity is explained by the similar behavior of the background and the effect (small negatively sloped linear function). In principle, correct modeling of the ^{40}K background, can eliminate the major part of the background, which will finally lead to better results. The obtained values are more than one order of magnitude stronger than those obtained for low-energy neutrinos in direct experiments.

4. Using the data obtained with the prototype of the Borexino detector, the lower limit on the mean lifetime of pp- and ^{7}Be-neutrino relative radiative decay is obtained: $\tau_{c.m.}(\nu_H \longrightarrow \nu_L + \gamma)/m_\nu \geq 4.2 \times 10^3$ s · eV^{-1} ($\alpha = 0$). It is more than one order of magnitude stronger than that obtained in previous experiments using nuclear reactors and accelerators. The CTF data can be used in the search for $\nu_H \longrightarrow \nu_L + e^+ + e^-$ decays as well.

This work was supported by the INFN Milano section in accordance with the scientific agreement on Borexino between INFN and JINR (Dubna). We thank Prof. G. Bellini and Dr. G. Ranucci, who organized our stay at the LNGS laboratory. Thanks to all our colleagues from the Borexino collaboration. We are very grateful to Richard Ford for careful reading of the manuscript.

REFERENCES

1. B. W. Lee and R. E. Shrock, Phys. Rev. D **16**, 1444 (1977).
2. S. T. Petkov, Yad. Fiz. **25**, 641 (1977) [Sov. J. Nucl. Phys. **25**, 340 (1977)].
3. E. Sato and M. Kobayashi, Prog. Theor. Phys. **58**, 1775 (1977).
4. M. A. Beg, W. J. Marciano, and M. Ruderman, Phys. Rev. D **17**, 1395 (1978).
5. A. De Rujula and S. L. Glashow, Phys. Rev. Lett. **45**, 942 (1980).
6. W. J. Marciano and A. Sirlin, Phys. Rev. D **22**, 2695 (1980).
7. P. B. Pal and L. Wolfenstein, Phys. Rev. D **25**, 766 (1982).
8. R. E. Shrock, Nucl. Phys. B **296**, 359 (1982).
9. F. Boem and P. Vogel, *Physics of Massive Neutrinos* (Cambridge Univ. Press, Cambridge, 1992).
10. F. Reines *et al.*, Phys. Rev. Lett. **32**, 180 (1974).
11. P. Vogel, Phys. Rev. D **30**, 1505 (1984).
12. G. Zacek, F. von Feilitzsch, R. L. Mossbauer, *et al.*, Phys. Rev. D **34**, 2621 (1986).
13. L. Oberauer, F. von Feilitzsch, and R. L. Mossbauer, Phys. Lett. B **198**, 113 (1987).
14. A. V. Derbin, A. V. Chernyĭ, L. A. Popeko, *et al.*, Pis'ma Zh. Éksp. Teor. Fiz. **57**, 755 (1993) [JETP Lett. **57**, 768 (1993)].
15. D. A. Krakauer, R. L. Talaga, R. C. Allen, *et al.*, Phys. Rev. D **44**, R6 (1991).
16. G. G. Raffelt, Phys. Rev. D **31**, 3002 (1985).
17. D. E. Groom *et al.* (Particle Data Group), Eur. Phys. J. C **15**, 1 (2000).

18. L. Oberauer, C. Hagner, G. Raffelt, and E. Rieger, Astropart. Phys. **1**, 377 (1993).
19. G. G. Raffelt, Phys. Rep. **320**, 319 (1999).
20. G. Alimonti *et al.* (Borexino Collab.), Astropart. Phys. **18**, 1 (2002).
21. G. Ranucci *et al.*, Nucl. Instrum. Methods Phys. Res. A **333**, 553 (1993).
22. G. Alimonti *et al.* (Borexino Collab.), Nucl. Instrum. Methods Phys. Res. A **406**, 411 (1998).
23. G. Alimonti *et al.* (Borexino Collab.), Phys. Lett. B **422**, 349 (1998).
24. G. Alimonti *et al.* (Borexino Collab.), Astropart. Phys. **8**, 141 (1998).
25. G. Alimonti *et al.* (Borexino Collab.), Nucl. Instrum. Methods Phys. Res. A **440**, 360 (2000).
26. J. B. Birks, Proc. Phys. Soc. London, Sect. A **64**, 874 (1951).
27. H. O. Back *et al.* (Borexino Collab.), Phys. Lett. B **525**, 29 (2002).
28. O. Ju. Smirnov, LNGS Preprint INFN TC/00/17, accepted by PTE (2002).
29. V. V. Kuzminov and N. Ja. Osetrova, Yad. Fiz. **63**, 1365 (2000) [Phys. At. Nucl. **63**, 1292 (2000)].
30. J. N. Bahcall, H. Pinsonneault, and S. Basu, Astrophys. J. **555**, 990 (2001).
31. J. N. Bahcall, Phys. Rev. C **56**, 3391 (1997).
32. W. R. Nelson, H. Hirayama, and D. W. O. Rogers, The EGS4 Code System, SLAC-265 (1985).

JETP Letters, Vol. 76, No. 7, 2002, pp. 414–418. Translated from Pis'ma v Zhurnal Éksperimental'noĭ i Teoreticheskoĭ Fiziki, Vol. 76, No. 7, 2002, pp. 488–492.

Nontrivial Class of Composite $U(\sigma + \mu)$ Vector Solitons

A. M. Agalarov[1, *] and R. M. Magomedmirzaev[2]

[1] *Moscow State University, Vorob'evy gory, Moscow, 119899 Russia*

**e-mail: agalarov@itp.ac.ru*

[2] *Institute of Physics, Dagestan Scientific Center, Russian Academy of Sciences, Makhachkala, 367025 Russia*

Received July 5, 2002; in final from, September 12, 2002

A mixed problem for the compact $U(m)$ vector nonlinear Schrödinger model with an arbitrary sign of coupling constant is exactly solved. It is shown that a new class of solutions—composite $U(\sigma + \mu)$ vector solitons with inelastic interaction (changing shape without energy loss) at $\sigma > 1$ and strictly elastic interaction at $\sigma = 1$—exists for $m \geq 3$. These solitons are color structures consisting of σ bright and μ dark solitons ($\sigma + \mu = m$) and capable of existing in both self-focusing and defocusing media. The N-soliton formula universal for attraction and repulsion is derived by the Hirota method. © *2002 MAIK "Nauka/Interperiodica".*

PACS numbers: 03.50.Kk; 11.10.Lm; 42.65.Tg

The evolution system of m coupled nonlinear Schrödinger equations (CNSE-m)

$$i\hat{L}_j\psi_j^* = \sum_{k=1}^{m} a_{jk}|\psi_k|^2\psi_j^*, \quad j = \overline{1, m},$$
$$\psi_j \in \mathbf{C}, \quad \hat{L}_j = \partial_\zeta + ic_j\partial_{\xi\xi}; \quad a_{jk}, c_j \in \mathbf{R}, \tag{1}$$

arises in the weak-coupling limit in various nonrelativistic models of nonlinear field theory. The conditions for integrability and exact solutions of CNSE-m are of both practical and academic interest (nonlinear optics, plasma, ferromagnetism, hydrodynamics, atomic Bose–Einstein condensates, etc. [1–6]). Two coupled parabolic equations of motion that are equivalent to set (1) with $m = 2$ and $c_1 = c_2$ were rigorously derived in [7], where the self-action of differently polarized waves in nonlinear media with tensor response was studied. In Eqs. (1), parameters c_j determine dispersion, and coefficients a_{jk} with $j \neq k$ and $j = k$ determine the nonlinear interaction and self-actions of fields ψ_j, respectively. For different variables ζ and ξ and different $\kappa_k = \mathrm{sgn}(c_j a_{jk})$, Eqs. (1) describe, at the classical level, the spatial or time evolution of an m-component field in a cubic nonlinear medium [7, 8] and, at the quantum level, a Bose gas with m color degrees of freedom [9, 10] with the attractive ($\kappa_k > 0$) or repulsive ($\kappa_k < 0$) point interaction.

Set (1) is exactly integrable in the Liouville sense only in a few cases, where strict conditions are satisfied for the driving parameters c_j and a_{jk}. Using Zakharov theorems on the additional motion invariants, we can prove (proof will be given elsewhere) that set (1) with $a_{jk} = \pm a_{kk}$ and $c_j = \pm c$ allows the zero-curvature representation (Lax pair) and can be treated by the method of the inverse scattering problem (MISP). In this case, the integrable reductions of the CNSE-m form a set of vector models of solitons with unitary $U(m)$ and pseudounitary $U(m, n)$ symmetry groups. The known exact solutions to this set of models, e.g., the Manakov U(2) vector model [8] ($L_0 = L_1 = L_2$, $\sigma = 2$, and $\mu = 0$)

$$i\hat{L}_0\psi_j^* = \kappa(|\psi_1|^2 + |\psi_2|^2)\psi_j^*, \; j = \overline{1, 2}, \tag{2}$$

are single-color multisolitons, bright ($\psi_{1, 2, \ldots} \sim \mathrm{sech}\alpha$) [8] and dark ($\psi_{1, 2, \ldots} \sim \tanh\beta$) [11, 12] in self-focusing ($\kappa > 0$) and defocusing media ($\kappa < 0$), respectively. In this sense, bright [8] and dark [11, 12] vector soliton solutions constructed on the basis of U(1) scalar bright [$\psi(\pm\infty) = 0$] and dark [$\psi(\pm\infty) = \rho\exp(i\Theta)$] solitons [5, 13] of the conventional boundary problems can be associated with the trivial class. Exact solutions to the pseudo-Euclidean U(1, 1) model (by the MISP) [9] and Euclidean U(1 + 1) model (2) with defocusing nonlinearity ($\kappa < 0$) (by the Hirota method) [12] indicate that the composite vector solitons, as well as U(1) scalar solitons, interact elastically (trivially).

In this study, we demonstrate that the set of $U(m)$ vector nonlinear Schrödinger models [integrable reductions of set (1)]

$$i\hat{L}_0\psi_j^* = \kappa\sum_{k=1}^{m}|\psi_k|^2\psi_j^*, \quad j = \overline{1, m} \tag{3}$$

with the mixed-density boundary conditions

$$\psi_\sigma(\zeta, \xi)|_{|\xi|\to\infty} \longrightarrow 0, \quad \psi_\mu(\zeta, \xi)|_{|\xi|\to\infty} \longrightarrow \rho_\mu e^{i\Theta_\mu} \tag{4}$$

with $m \geq 3$ has the class of exact solutions—color $U(\sigma + \mu)$ vector solitons, where $\sigma = 1, 2, \ldots, m$ and $\mu = m - \sigma$, with nontrivial interaction (intermode exchange). Conditions (4) mean that each degree of freedom $\psi_n (1 \leq n \leq m)$ in set (3) has its zero-density,

$\rho_n = 0$, or nonzero-density, $\rho_n \neq 0$, vacuum (condensate) with asymptotic phase ρ_n^2.

The *N*-soliton formula of *m*-component set (3) and (4) is universal for self-focusing (attractive; $\mathrm{sgn}\kappa = +1$) and defocusing (repulsive; $\mathrm{sgn}\kappa = -1$) media with cubic nonlinearity.

Applying MISP to set (3) and (4), one must analyze the structure of $(m + 1)$-sheet Reimann surfaces. For this reason, we obtained the *N*-soliton solution by the Hirota method [14], which is mathematically less cumbersome. The elastic (trivial) type of interaction between composite (bright and dark) U(1 + 1) vector solitons [9, 12] was shown to follow from the factorization of the *N*-soliton solution of set (3) and (4) in the particular case of $m = 2$. In the general case, the *N*-soliton solution is nonfactorable, and the interaction of color multisolitons is inelastic (changes the shape with conserving energy). We found special cases where the exchange between nonlinear modes does not arise and *N*-soliton scattering is factorable.

1. We introduce the Hirota functions

$$G_j = H\psi_j, \quad G_j \in \mathbf{C}, \quad H \in \mathbf{R}, \quad j = \overline{1, m}$$

and change ($\hat{L}_j \longrightarrow \hat{D}_j$) linear operators $\hat{L}$ to bilinear operators $\hat{D}$ defined as

$$\hat{D}(UV) = (\hat{D}U)V - U(\hat{D}V).$$

In what follows, we consider variables ζ and ξ in Eqs. (1), (3), and (4) as time *t* and coordinate *x*.

With scaling changes $|\kappa| = 2$, $c_j = c(>0)$, and $x \longrightarrow x\sqrt{c}$, set (1) in the Hirota representation forms a bilinear set of the compact $U(m)$ symmetry:

$$\hat{D}_1 G_j H = 0, \quad j = \overline{1, m},$$

$$\hat{D}_2 HH = 2\delta \sum_k^m |G_k|^2 \tag{5}$$

$$(\hat{D}_1 = i\hat{D}_t + \hat{D}_2, \hat{D}_2 = \hat{D}_x^2 - \lambda),$$

where $\lambda \in \mathbf{R}$ is an arbitrary parameter determined below and $\delta = \mathrm{sgn}\kappa$.

In terms of bilinear operators, the functions G_j and *H* can be represented as a series in powers of the formal parameter ε. We choose this representation so that it is consistent with boundary conditions (4):

$$G_j = \sum_{\nu=0}^{\infty} \varepsilon^{2\nu}(g_{0\mu} g_{2\nu}^{\mu} \delta_{j\mu} + \varepsilon g_{0\sigma} g_{2\nu+1}^{\sigma} \delta_{j\sigma}),$$

$$H = \sum_{\nu=0}^{\infty} \varepsilon^{2\nu} h_{2\nu}; \quad g_0^{\mu} = h_0 = g_{0\sigma} = 1, \tag{6}$$

where $\delta_{\alpha\beta}$ is the Kronecker delta and $j = \overline{1, m}$. Functions G_j obviously specify an *m*-component field ($m = \sigma + \mu$) for an arbitrary combination of σ and μ (e.g., σ bright solitons and μ dark solitons). The *N*-soliton solution describing the evolution of solitons in set (5) is obtained according to the standard Hirota scheme ($R \sim G_j, H; j = \overline{1, m}$)

$$R = R_0 \xrightarrow{\varepsilon^0} R_1 \xrightarrow{\varepsilon^1} R_2 \xrightarrow{\varepsilon^2} \ldots \xrightarrow{\varepsilon^{N-1}} R_N. \tag{7}$$

To zero order in ε, we take the vacuum solution $g_{0\mu} = \rho_\mu \exp(i\Theta_\mu)$, where $\Theta_\mu = k_\mu x - (k_\mu^2 + \lambda)t$ with

$$\lambda = -2\delta \sum_{\mu}^{m-\sigma} \rho_\mu^2$$

found from Eqs. (5). In the physics of optical solitons, $\delta = \mathrm{sgn}\kappa = +1$ and -1 correspond to the self-focusing and defocusing media, respectively. To the first order in ε, we have

$$g_1^{(j)} = \sum_{n=1}^{N} \gamma_n^{(j)} \exp(\eta_n),$$

$$\eta_n = \zeta_n x + i\left(\zeta_n^2 + 2\delta \sum_{\mu}^{m-\sigma} \rho_\mu^2\right)t,$$

where $\gamma_n^{(j)}$ and ζ_n are arbitrary complex parameters. In the single-soliton ($N = 1$), two-soliton ($N = 2$), etc. sectors, series (6) in scheme (7) terminate in the second, fourth, etc. orders in ε, respectively. Solutions (to sixth order in ε) of set (5) describing the evolution of *N* solitons in two σ and μ sectors of the $U(m)$ vector ψ space have the form

$$H\psi_\sigma = \sum_{n=1}^{N} \hat{\eta}_n \left\{ \varepsilon^1 \gamma_n^{\sigma} + \sum_{ij}^{N} \hat{\eta}_i \hat{\eta}_j^* (\varepsilon^3 a_{nij}^{\sigma} + \varepsilon^5 \sum_{l,m}^{N} a_{nijlm}^{\sigma} \hat{\eta}_l \hat{\eta}_m^* + \ldots, \right. \tag{8}$$

$$H\psi_\mu = g_{0\mu} \left\{ \varepsilon^0 + \sum_{ij}^{N} \hat{\eta}_i \hat{\eta}_j^* \left[\varepsilon^2 a_{ij}^{\mu} + \sum_{lm}^{N} \hat{\eta}_l \hat{\eta}_m^* (\varepsilon^4 a_{ijlm}^{\mu} + \varepsilon^6 \sum_{q,r}^{N} a_{ijlmqr}^{\mu} \hat{\eta}_q \hat{\eta}_r^* + \ldots, \right. \right. \tag{9}$$

$$H = \varepsilon^0 + \sum_{ij}^{N} \hat{\eta}_i \hat{\eta}_j^* \left[\varepsilon^2 a_{ij} + \sum_{lm}^{N} \hat{\eta}_l \hat{\eta}_m^* (\varepsilon^4 a_{ijlm} + \varepsilon^6 \sum_{q,r}^{N} a_{ijlmqr} \hat{\eta}_q \hat{\eta}_r^* + \ldots . \right.$$

Here, parameter $\varepsilon = 1$ (Hirota), $\hat{\eta}_n = \exp(\eta_n)$,

$$a^{\sigma}_{nij} = \frac{\zeta^{-}_{ni}}{\zeta_{nj}\zeta_{ij}}(\gamma^{\sigma}_{n}\tilde{a}_{ij} - \gamma^{\sigma}_{i}\tilde{a}_{nj}),$$

$$a_{ijlm} = \frac{\zeta^{-}_{il}\bar{\zeta}^{-}_{jm}}{\zeta_{ij}\zeta_{im}\zeta_{lj}\zeta_{lm}}(\tilde{a}_{ij}\tilde{a}_{lm} - \tilde{a}_{im}\tilde{a}_{lj}),$$

$$a^{\sigma}_{nijlm} = \frac{\zeta^{-}_{ni}\zeta^{-}_{nl}}{\zeta_{nj}\zeta_{nm}}\gamma^{\sigma}_{n}a_{ijlm} + \left\{ \begin{array}{c} n \leftrightarrow i \leftrightarrow l \\ j \leftrightarrow m \end{array} \right\},$$

$$a_{ijlmqr} = \frac{\zeta^{-}_{qi}\zeta^{-}_{ql}\bar{\zeta}^{-}_{rj}\bar{\zeta}^{-}_{rm}}{\zeta_{qj}\zeta_{qm}\zeta_{ir}\zeta_{lr}}a_{ijlm}a_{qr} + \left\{ \begin{array}{c} q \leftrightarrow i \leftrightarrow l \\ r \leftrightarrow j \leftrightarrow m \end{array} \right\}, \quad (10)$$

$$a^{\mu}_{\ldots ij\ldots} = z^{\mu}_{ij}a_{\ldots ij\ldots}, \quad z^{\mu}_{ij} = -\frac{z_{i\mu}}{\bar{z}_{j\mu}}, \quad z_{j\mu} = \zeta_j - ik_{\mu},$$

$$\tilde{a}_{ij} = \frac{\sum_{\sigma=1}^{m-\mu}\gamma^{\sigma}_{i}\bar{\gamma}^{\sigma}_{j}}{\zeta_{ij}\left(\delta + \sum_{\mu}^{m-\sigma}\rho^{2}_{\mu}/z_{i\mu}\bar{z}_{j\mu}\right)}, \quad a_{ij} = \frac{\tilde{a}_{ij}}{\zeta_{ij}},$$

$$\zeta_{lm} = \zeta_l + \bar{\zeta}_m, \quad \zeta^{-}_{lm} = \zeta_l - \zeta_m, \quad \bar{O} \equiv O^{*}, \quad k_{\mu} \in \mathbf{R}.$$

One can clearly see from these formulas that the two-soliton ($N = 2$) solution terminates in the fourth order in ε. At the same time, Eqs. (8) and (9) correspond to the exact three-soliton ($N = 3$) solution of set (5). Higher order solutions are not presented because of their awkwardness.

2. Single-soliton ($N = 1$) solution of the mixed nonlinear $U(\sigma + \mu)$ vector Schrödinger model (3) and (4), according to Eqs. (8)–(10), has the form

$$\begin{pmatrix} \psi_{\{\sigma\}} \\ \psi_{\{\mu\}} \end{pmatrix} = H^{-1}\begin{pmatrix} \gamma^{\sigma}_{1}e^{\eta_1} \\ g_{0\mu}(1 + a^{\mu}_{11}e^{\eta_1 + \bar{\eta}_1}) \end{pmatrix}, \quad (11)$$

where the Hirota function has the form $H = 1 + a_{11}e^{\eta_1 + \bar{\eta}_1}$ with

$$a^{-1}_{11} = \zeta^{2}_{11}\left(\delta + \sum_{\mu}^{m-\sigma}\rho^{2}_{\mu}|z_{1\mu}|^{-2}\right)\Big/\sum_{\sigma}^{m-\mu}|\gamma^{\sigma}_{1}|^{2},$$

$$a^{\mu}_{11} = z^{\mu}_{11}a_{11}, \quad z^{\mu}_{11} = -\exp(2i\phi_{1\mu}),$$

$$\phi_{1\mu} = \arctan((\mathrm{Im}\zeta_1 - k_{\mu})/\mathrm{Re}\zeta_1).$$

As is seen, mixed-color $U(\sigma + \mu)$ vector soliton (11) is a dynamic topological formation, and its particular cases coincide with the known single-color bright ($\psi_{\{\mu\}} = 0$, $\delta = +1$) [8] and dark ($\psi_{\{\sigma\}} = 0$, $\delta = -1$) [11, 12] solitons. However, in contrast to vector solitons [8, 11, 12], exact solution (11) satisfies set (3) for both attraction (self-focusing; $\delta = +1$) and repulsion (defocusing; $\delta = -1$). Moreover, universal color $U(\sigma + \mu)$ vector soliton (11) can be determined in some states by its dynamic topological origin. It is convenient to treat these states in terms of particles. Let $\{\sigma, \mu\}$, where $\sigma + \mu = m$, specifies the possible isotopic states of the color $U(\sigma + \mu)$ vector soliton given by Eq. (11). Then, by analogy with QCD, the state with mixed color $\{\sigma \neq 0, \mu \neq 0\}$ can be considered as flavor, whereas the state without mixing ($\{0, \mu\}$), $\{\sigma, 0\}$), as flavorless (single-color). By this analogy, the mixed-color $U(m)$ vector soliton has an internal structure, and the existence of various states is reasonable for this composite particle. In particular, for the U(5) vector nonlinear Schrödinger model, solution (11) for one ($\{3, 2\}$) of four possible flavor states ($\{1, 4\}$, $\{2, 3\}$, $\{3, 2\}$, $\{4, 1\}$) of the color U(3 + 2) vector soliton has the form

$$\begin{pmatrix} \psi_1 \\ \psi_2 \\ (\psi_3\psi_4\psi_5)^{t} \end{pmatrix} = \begin{pmatrix} A_1(\tanh X + i\tan\phi_1)e^{i\Theta_1} \\ A_2(\tanh X + i\tan\phi_2)e^{i\Theta_2} \\ (B_3B_4B_5)^{t}\,\mathrm{sech}\,Xe^{i\Theta} \end{pmatrix}. \quad (12)$$

Here,

$$A_{\mu} = \rho_{\mu}\cos\phi_{\mu}, \quad \Theta_{\mu} = k_{\mu}x - \left(k^{2}_{\mu} - 2\delta\sum_{\mu=1}^{2}\rho^{2}_{\mu}\right)t + \phi_{\mu},$$

$$\phi_{\mu} = \arctan((v - 2k_{\mu})/u); \quad 2X = u(x - vt - x_0),$$

$$B_{\sigma} = \gamma^{\sigma}\left[\left(\sum_{\mu=1}^{2}A^{2}_{\mu} + \delta u^{2}/4\right)\Big/\sum_{\sigma=3}^{5}|\gamma^{\sigma}|^{2}\right]^{\frac{1}{2}},$$

$$2\Theta = vx + \left(u^{2} - v^{2} + 8\delta\sum_{\mu=1}^{2}\rho^{2}_{\mu}\right)t/2,$$

$$\mu = 1, 2, \quad \sigma = 3, 4, 5,$$

where $u = 2\mathrm{Re}\zeta_1$ and $v = 2\mathrm{Im}\zeta_1$ are the inverse width and velocity of the soliton, respectively. It is seen that the composite U(5) vector soliton given by Eq. (12) consists of two dark (ψ_1, ψ_2) and three bright (ψ_3, ψ_4, ψ_5) components (nonlinear modes). The U(5) vector soliton has six possible states. However, two of them are flavorless (single-color) vector solitons—bright {5, 0} and dark {0, 5} vector solitons in self-focusing ($\delta = +1$) and defocusing ($\delta = -1$) media, respectively. A change in the refractive index of the medium induced by the interaction of the $\psi_1, \ldots, \psi_5$ components $\Delta n^2 \sim |\psi_1|^2 + |\psi_2|^2 + \ldots + |\psi_5|^2$ can be calculated by directly substituting explicit solution (12). However, the universal formula

$$\Delta n^{2} = \sum_{\mu}\rho^{2}_{\mu} + \delta\frac{d^{2}}{dx^{2}}\ln H, \quad (13)$$

following for the whole set of $U(m)$ vector nonlinear Schrödinger models from Eqs. (5), expresses Δn^2 in terms of the common Hirota function H. In particular, for the above U(5) model with $\mu = \overline{1, 2}$ one has $H = 1 + a_{11}e^{\eta_1 + \bar{\eta}_1}$. Then Eq. (13) yields

$$\Delta n^2 = \rho_1^2 + \rho_2^2 \pm \left(\frac{u^2}{4}\right)\mathrm{sech}^2\left[\frac{u(x - vt - x_0)}{2}\right]$$

with signs + and – for the self-focusing and defocusing media, respectively.

The presence of a vacuum–condensate with nonzero density ρ_μ^2—in a defocusing medium ($\delta = -1$) poses the following reasonable restriction on the characteristics of the color vector soliton:

$$u^2 \le 4\sum_\mu \rho_\mu^2 \cos^2\phi_\mu.$$

Nevertheless, since the color $U(m)$ vector soliton has $(m - 1)$ possible flavor states, the observation of these states in multimode optical systems may be more probable than the observation of single-color states, whose number equals two.

3. Two-soliton ($N = 2$) solution and the interaction dynamics of mixed-color multisolitons. Let us demonstrate that the interaction of color multisolitons specified by Eqs. (8) and (9) in the mixed $U(m)$ vector nonlinear Schrödinger model given by Eqs. (3) and (4) is nontrivial (changing the shape without energy loss) at $m \ge 3$, and the intermode (energy) exchange occurs proportional to the intensities of the soliton nonlinear modes. Without loss of generality, we analyze the asymptotic behavior ($t \longrightarrow \pm\infty$) of color multisolitons specified by Eqs. (8) and (9) for $N = 2$.

Two-soliton solution (N = 2) given by Eqs. (8) and (9) takes the form

$$\begin{pmatrix} \psi_{\{\sigma\}} \\ \psi_{\{\mu\}} \end{pmatrix} = H^{-1}\begin{pmatrix} \gamma_1^\sigma e^{\eta_1} + \gamma_2^\sigma e^{\eta_2} + \sum_j^2 a_{12j}^\sigma e^{\eta_1 + \eta_2 + \bar{\eta}_j} \\ g_{0\mu}\left(1 + \sum_{i,j}^2 a_{ij}^\mu e^{\eta_i + \bar{\eta}_j} + a_{1122}^\mu e^{\eta_1 + \bar{\eta}_1 + \eta_2 + \bar{\eta}_2}\right) \end{pmatrix}, \quad (14)$$

where $\sigma + \mu = m$ and the Hirota function is

$$H = \left(1 + \sum_{i,j}^2 a_{ij}e^{\eta_i + \bar{\eta}_j} + a_{1122}e^{\eta_1 + \bar{\eta}_1 + \eta_2 + \bar{\eta}_2}\right).$$

Let $v_1 > v_2$ ($\mathrm{Im}\,\zeta_1 > \mathrm{Im}\,\zeta_2$), where v_n is the velocity of the S_j^n soliton in the jth mode ($j = 1, 2, \ldots, \mu, \mu + 1, \ldots, \mu + \sigma$). Solution (14) for $t \longrightarrow \pm\infty$ on the trajectories $\xi_n = x - v_n t$ of individual S_j^n solitons is decomposed into the sum of free soliton solutions given by Eq. (12):

$$\psi_{\{j\}}(x, t)|_{t \to \pm\infty} = \sum_n C_j^{n\pm} S_{\{j\}}^n (x - v_n t, x_{0n}^\pm) e^{i\Theta_{nj}}. \quad (15)$$

Here, the envelope $S_{\{j\}}^n$ of the nth soliton in the jth mode for $n = 1, 2$ and $j = \sigma, \mu$ has the form

$$S_{\{\sigma\}}^n = \mathrm{sech}\,Y_n^\pm, \quad S_{\{\mu\}}^n = \tanh Y_n^\pm + i\tan\phi_{n\mu},$$

where

$$Y_n^\pm = u_n(x - v_n t - x_{0n}^\pm)/2,$$
$$\phi_{n\mu} = \arctan((v_n - 2k_\mu)/u_n), \quad u_n = 2\mathrm{Re}\,\zeta_n,$$
$$v_n = 2\mathrm{Im}\,\zeta_n;$$

and soliton amplitudes C_j^{n+} and C_j^{n-} before and after the interaction are related to one another as $C_j^{n+} = \hat{S}_j^n C_j^{n-}$, where the matrix $\hat{S}$ transforms the asymptotic function for $t \longrightarrow -\infty$ to the asymptotic function for $t \longrightarrow +\infty$. These amplitudes and matrix have the form

$$\hat{S}_\sigma^1 = \tilde{\zeta}_{12}(1 - s_1\gamma_{21}^\sigma)(1 - s_1 s_2)^{-1/2},$$
$$2C_\sigma^{1-} = \gamma_1^\sigma (a_{11})^{-1/2}, \quad \hat{S}_\mu^1 = e^{i(2\phi_{2\mu} - \pi)},$$
$$C_\mu^{1-} = \rho_\mu \cos\phi_{1\mu} e^{i(\phi_{1\mu} + \pi)},$$
$$\hat{S}_\sigma^2 = \tilde{\zeta}_{21}(1 - s_2\gamma_{12}^\sigma)^{-1}(1 - s_1 s_2)^{1/2}, \quad (16)$$
$$2C_\sigma^{2-} = a_{121}^\sigma (a_{1122}a_{11})^{-1/2}, \quad \hat{S}_\mu^2 = e^{-i(2\phi_{1\mu} - \pi)},$$
$$C_\mu^{2-} = \rho_\mu \cos\phi_{2\mu} e^{i(2\phi_{1\mu} + \phi_{2\mu})},$$

where

$$\gamma_{ij}^\sigma = \frac{\gamma_i^\sigma}{\gamma_j^\sigma}, \quad s_1 = \frac{\tilde{a}_{12}}{\tilde{a}_{22}}, \quad s_2 = \frac{\tilde{a}_{21}}{\tilde{a}_{11}}, \quad |\tilde{\zeta}_{12}| = |\tilde{\zeta}_{21}| = 1.$$

It is seen that the soliton velocities v_n are invariants of motion, whereas the phases $X_{0n}^\pm$ and amplitudes $C_j^{n\pm}$ are not. Since $|\hat{S}_\sigma^n| \ne 1$ and $|\hat{S}_\mu^n| = 1$ in the general case, the interaction of mixed-color $U(\sigma + \mu)$ vector solitons (14) is nontrivial and gives rise to the exchange of intensity between modes, which is proportional to $\sim|\hat{S}_j^n|^2$. This exchange is responsible for the energy redistribution in the components (nonlinear modes) of color vector solitons. However, the exchange effects different character in the σ and μ modes: σ modes exchange nonzero energy $\sim|\hat{S}_\sigma^n|^2$ and conserve sign, whereas μ modes conserve energy ($|\hat{S}_\mu^n|^2 = 1$) but

change their signs and acquire additional phase shift $\sim(2\phi_{n\mu} + \pi)$ as a result of interaction. It is seen that the μ modes interact only if their phases are different.

As a whole, the asymptotic analysis indicates that the exchange between the components of an individual color soliton is not arbitrary (chaotic) but correlates with the corresponding changes in the components of all other solitons. The nontrivial interaction of color multisolitons (14) and the possible intermode exchanges in the system described by Eqs. (3) and (4) must satisfy the conservation laws for (i) the total intensity of an individual S_j^n soliton, $\sum_j^m |C_j^{n-}|^2 = \sum_j^m |C_j^{n+}|^2$, and (ii) the total intensity of all solitons before and after interaction, $\sum_n (\sum_j |C_j^{n-}|^2) = \sum_n (\sum_j |C_j^{n+}|^2)$. The validity of these laws can easily be seen from asymptotic Eqs. (16). In addition, the interaction-induced shifts of the soliton centers of mass $\Delta X_n = X_{0n}^+ - X_{0n}^- = (-1)^{n+1} 2\zeta_{nn}^{-1} \ln\chi$, where

$$\chi = \left|\frac{\zeta_1 - \zeta_2}{\zeta_{12}}\right|^2 \sqrt{1 + \frac{\zeta_{11}\zeta_{22}}{|\zeta_1 - \zeta_2|^2}(1 - \epsilon)}$$

with

$$\epsilon = \frac{\left(\delta + \sum_\mu^{m-\sigma} \rho_\mu^2/|z_{1\mu}|^2\right)\left(\delta + \sum_\nu^{m-\sigma} \rho_\nu^2/|z_{2\nu}|^2\right)\sum_{\sigma,r}^{m-\mu} \gamma_1^\sigma \gamma_2^\tau \tilde{\gamma}_1^\tau \tilde{\gamma}_2^\sigma}{\left|\delta + \sum_\mu^{m-\sigma} \rho_\mu^2/z_{1\mu}\bar{z}_{2\mu}\right|^2 \sum_{\sigma,r}^{m-\mu} |\gamma_1^\sigma|^2 |\gamma_2^\tau|^2} \quad (17)$$

obey the Sudzuki–Zakharov–Shabat condition $\zeta_{11}\Delta X_1 + \zeta_{22}\Delta X_2 = 0$ (conservation law for the soliton centers of mass), which follows from the conservation of the quantity $I_{\text{tot}} = \int \sum_n |\psi_n|^2 dx$ in time t. The above conservation laws and the exact formulas describe quantitatively the exchange kinetics and possible scenarios of intermode exchange in the system of color multisolitons (14). Let us discuss the factor ϵ in Eq. (17).

Owing to the explicit multiparticle effects in ϵ, the shifts ΔX_n of the centers of mass for color solitons do not have the factorization property that is conventional for ordinary solitons. Therefore, ϵ indicates a complex character of the interaction of composite $U(\sigma + \mu)$ vector solitons (14). In the general case [for arbitrary soliton parameters γ_n^j, ζ_n, $(z_{j\mu})$, vacuum densities ρ_μ^2, and the number of components $\sigma + \mu = m$), the soliton shifts ΔX_n cannot be represented in the two-particle form because of the presence of ϵ; the N-soliton scattering does not reduce to pair scattering, and the interaction of composite $U(\sigma + \mu)$ vector solitons at $\sigma \geq 2$ is nontrivial (changes the shape with energy conservation). In a particular case of the linear dependence of parameters $\gamma_i^\sigma \gamma_j^\nu - \gamma_i^\nu \gamma_j^\sigma = 0$, they do not affect ϵ, the contribution of vacuums is symmetrized, and the shifts ΔX_n of centers can be represented in the two-particle form. Therefore, N-soliton scattering is factorized, and the interaction between solitons becomes elastic ($|\hat{S}_j^n| = 1$, $j = \sigma$ and μ). Moreover, it directly follows from Eq. (17) that the interaction between composite U(1 + 1) vector solitons is completely elastic in the Manakov mixed U(2) model with $\sigma = \mu = 1$ [12]. In all other cases, color $U(\sigma + \mu)$ vector solitons with $m = \sigma + \mu \geq 3$ interact nontrivially, and their nonlinear modes undergo energy exchange satisfying the above conservation laws.

We are grateful to V.E. Zakharov for his attention to the work and S.V. Manakov and V.G. Marikhin for useful remarks. This work was performed in part at the Landau Institute for Theoretical Physics.

REFERENCES

1. V. E. Zakharov and E. A. Kuznetsov, Zh. Éksp. Teor. Fiz. **113**, 1892 (1998) [JETP **86**, 1035 (1998)].
2. Y. S. Kivshar and B. Luther-Davies, Phys. Rep. **298**, 81 (1998).
3. F. T. Hioe, Phys. Rev. Lett. **82**, 1152 (1999).
4. B. A. Kalinikos, M. M. Scott, and C. E. Patton, Phys. Rev. Lett. **84**, 4697 (2000).
5. L. D. Faddeev and L. A. Takhtajan, *Hamiltonian Methods in the Theory of Solitons* (Nauka, Moscow, 1986; Springer-Verlag, Berlin, 1987).
6. K. E. Strecker, G. Partridge, A. G. Truscott, and R. G. Hulet, Nature **417**, 150 (2002).
7. A. L. Berkhoer and V. E. Zakharov, Zh. Éksp. Teor. Fiz. **58**, 903 (1970) [Sov. Phys. JETP **31**, 486 (1970)].
8. S. V. Manakov, Zh. Éksp. Teor. Fiz. **65**, 505 (1973) [Sov. Phys. JETP **38**, 248 (1974)].
9. V. G. Makhan'kov and O. K. Pashaev, Teor. Mat. Fiz. **53**, 55 (1982).
10. A. V. Mikhaĭlov and A. B. Shabat, Teor. Mat. Fiz. **66**, 47 (1986).
11. R. Radhakrishnan and M. Lakshmanan, J. Phys. A **28**, 2683 (1995).
12. A. P. Sheppard and Yu. S. Kivshar, Phys. Rev. E **55**, 4773 (1997).
13. S. Novikov, S. V. Manakov, L. P. Pitaevskii, and V. E. Zakharov, *Theory of Solitons: The Inverse Scattering Method* (Nauka, Moscow, 1980; Consultants Bureau, New York, 1984).
14. R. Hirota, *Solitons*, Ed. by R. K. Bullough and P. J. Coudrey (Springer-Verlag, Berlin, 1980), p. 157.

Translated by R. Tyapaev

JETP Letters, Vol. 76, No. 7, 2002, pp. 419–422. Translated from Pis'ma v Zhurnal Éksperimental'noĭ i Teoreticheskoĭ Fiziki, Vol. 76, No. 7, 2002, pp. 493–496.

Nonlinear Resonant Polarization Rotation under Conditions of Coherent Population Trapping

R. A. Akhmedzhanov and I. V. Zelensky*

Institute of Applied Physics, Russian Academy of Sciences, ul. Ul'yanova 46, Nizhni Novgorod, 603950 Russia

** e-mail: zelensky@appl.sci-nnov.ru*

Received August 16, 2002

Nonlinear resonant optical rotation was studied over a wide range of experimental parameters at the Rb D_1 $F = 2 \longrightarrow F' = 1$ transition in the ^{87}Rb vapor under conditions of coherent population trapping. The angle of rotation was found to depend nonmonotonically on the laser intensity and applied magnetic field. The effect of optical pumping out to the level $F = 1$ is discussed. It is demonstrated experimentally that the Faraday rotation angle increases twofold upon the compensation for pumping. © *2002 MAIK "Nauka/Interperiodica".*

PACS numbers: 42.50.Gy; 42.25.Ja

The nonlinear polarization rotation (nonlinear Faraday effect) is among the effects that are closely allied to coherent population trapping and electromagnetically induced transparency in degenerate systems [1–10]. In measuring magnetic field with the help of the resonant Faraday effect, one ordinarily uses low-intensity laser radiation, because it allows the obviation of field-induced line broadening and provides a high sensitivity [1, 2]. This approach is suggested for measuring microgauss fields. It should be noted, however, that the applicability of this method, as a rule, is restricted to superlow magnetic fields (~100 μG). Moreover, due to the strong absorption under resonance conditions, measurements can be carried out only at low atomic concentrations.

The use of relatively high intensities and optically dense media is a promising approach in experiments with nonlinear resonant polarization rotation. In this case, the coherent population trapping occurs in medium, resulting in a decrease of absorption because of the effect of electromagnetically induced transparency. A wide range of measured fields (up to several gauss) is one of the advantages of this method, rendering it promising for practical applications such as, e.g., measurement of the variations in the earth magnetic field. In addition, the use of optically dense media increases the Faraday rotation angle up to several radian (compared to milliradians in the experiments with low intensities and optically thin media), thereby improving the measurement accuracy. In particular, the maximal rotation angle at the ^{87}Rb D_1 $F = 2 \longrightarrow F' = 1$ transition equals 10 rad in a magnetic field of 0.6 G [4]. The sensitivity of the method is limited by the dynamic Stark effect (intensity dependence), collisional effects, and by the radiation reabsorption (concentration dependence) [4, 5, 11, 12] and, as theoretical estimates show, is comparable with the sensitivity of the low-intensity measurements [13].

In this work, the nonlinear resonant polarization rotation in ^{87}Rb vapor was experimentally studied at the $F = 2 \longrightarrow F' = 1$ transition of the D_1 line. The $F = 2 \longrightarrow F' = 1$ transition was chosen among other transitions between the hfs components of the $5s_{1/2}$ and $5p_{1/2}$ levels because it is most sensitive to the magnetic field and, hence, is of the greatest practical interest. Measurements were performed over a wide range of laser intensities and magnetic fields. The laser parameters and the magnetic field were varied from 10 μW/cm^2 to 100 mW/cm^2 and from 0.25 to 25 G, respectively. Measurements were made in an optically dense medium with a rubidium concentration of ~10^{11} cm^{-3}, for which the role of collisional effects and radiation reabsorption was negligible, as was confirmed by the linear concentration dependence of rotation angle.

The scheme of experimental setup is shown in Fig. 1. An external cavity diode laser *1* was used as a source of monochromatic radiation. The radiation was linearly polarized at the laser output. Polarization was con-

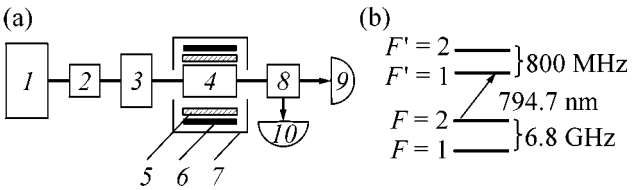

Fig. 1. (a) Scheme of the setup: (*1*) laser, (*2*) polarizer, (*3*) light filters, (*4*) cell with ^{87}Rb vapor, (*5*) heater, (*6*) solenoid, (*7*) magnetic screen, (*8*) polarizing beam splitter, and (*9*) and (*10*) photodiodes; (b) scheme of the hyperfine structure of the ^{87}Rb D_1 line.

0021-3640/02/7607-0419$22.00

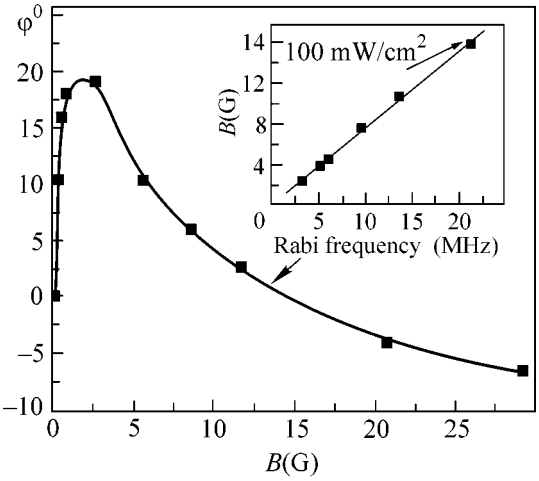

Fig. 2. Magnetic-field dependence of the Faraday rotation angle (for an intensity of 100 mW/cm^2 and a concentration of 1.5×10^{11} cm^{-3}). The dependence of a point at which the effect changes sign on the Rabi frequency (square root of intensity) is shown in the inset. The arrow indicates the point corresponding to an intensity of 100 mW/cm^2.

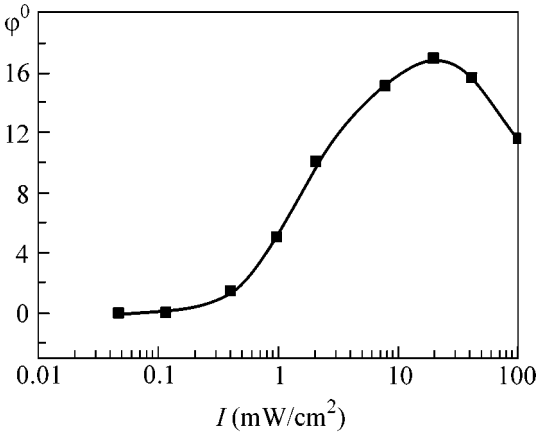

Fig. 3. Faraday rotation angle as a function of laser intensity (for a magnetic field of 0.85 G and a concentration of 1.1×10^{11} cm^{-3}).

trolled additionally by polarizer *2*. The intensity was varied using set of calibrated light filters *3*. The laser beam with a cross section of 2×5 mm passed through cylindrical cell *4* 56 mm in diameter and 55 mm in length filled with ^{87}Rb vapor without buffer gas. The cell was placed inside solenoid *6*, which was used to produce a longitudinal magnetic field. To prevent influence of the laboratory magnetic field, magnetic screen *7* was used. The screening quality was checked against the absence of Faraday rotation in the switched-off solenoid. The rubidium concentration in the cell was varied using heater *5*. When passing through the cell, laser beam fell on polarizing beam splitter *8*, which was set at an angle of 45° to the laser output polarization. The Faraday rotation angle and the absorption in the cell were calculated using the radiation intensity measured in the different splitter arms by photodiodes *9* and *10*.

The magnetic-field dependence of the Faraday rotation angle is presented in Fig. 2. The measurements were performed with a laser intensity of 100 mW/cm^2 and a concentration of ^{87}Rb atoms of 1.5×10^{11} cm^{-3}. In low fields, the rotation angle increases linearly with magnetic field, following the linear increase of Zeeman splitting. On further increase in a magnetic field and, correspondingly, in Zeeman splitting, the left-hand and right-hand circular light polarizations get off the two-photon Raman resonance, which is responsible for the coherent population trapping. This disturbs the coherence between the magnetic sublevels and, hence, reduces the Faraday effect. The decay of atomic coherence and of the attendant electromagnetically induced transparency is confirmed by the experimentally observed increase in absorption. At even higher magnetic fields, the rotation angle changes sign. The change in sign of the effect is caused by a change in the medium dispersion characteristics after the decay of atomic coherence; this is analogous to a change in sign of the derivative of refractive index for a probe wave in the experiments with electromagnetically induced transparency [7].

Measurements showed that the curve for the magnetic-field dependence of Faraday rotation angle changed its shape (position of a maximum, point at which the effect changes sign, etc.) with changing light intensity. It proved that the magnetic field at which the effect changes sign depends linearly on the square root of intensity, i.e., on the Rabi frequency of laser field (inset in Fig. 2). The corresponding Zeeman splitting approximates the Rabi frequency. In particular, for an intensity of 100 mW/cm^2 (Rabi frequency 21.5 MHz), the effect changes sign in the magnetic field B = 15 G corresponding the sublevel splitting $\delta = g\mu_B B/h \approx$ 21 MHz, where μ_B is the Bohr magneton, h is Planck's constant, and g is the Landé factor taken to be unity for estimation.

Measurement of the rotation angle as a function of light intensity showed that, at low intensities, the medium is virtually insensitive to magnetic field. As the intensity increases, the rotation angle starts to grow rapidly, reaches maximum, and then decreases (Fig. 3). Such a behavior can be explained in the following way. At low intensities, the atomic coherence is almost absent in medium. As a certain threshold is exceeded, the onset of coherent population trapping is observed in the medium, resulting in a sharp enhancement of the Faraday effect. The experimentally observed threshold intensity was found to be ~100 μW/cm^2 (Fig. 3). This is slightly higher than the threshold of coherent population trapping caused by the relaxation processes $\Omega \approx$

$\sqrt{2\Gamma\gamma}$ = 0.44 MHz, where $\gamma \approx 6$ MHz is the homogeneous width of the transition and $\Gamma \approx 16$ kHz is the Zeeman coherence relaxation rate, which is equal in the experimental conditions to the time of atomic flight through the laser beam (the corresponding light intensity is 40 μW/cm^2). The threshold shift can be explained by the fact that the Rabi frequency becomes equal to the Zeeman splitting at the intensities on the order of 100 μW/cm^2 in the applied magnetic field, and the effect is close to zero (inset in Fig. 2).

With an increase in laser intensity, the number of atoms involved, within the inhomogeneously broadened contour (the Doppler halfwidth in the experiment was $W_D \approx 250$ MHz), in the coherent population trapping and interacting efficiently with light increases. This results in an increase in the Faraday rotation angle with increasing intensity.

On further rise in intensity, the effect starts to weaken. Theoretical estimates within a simplified three-level Λ-type scheme without inhomogeneous broadening indicate that, at high intensities, the Faraday effect is inversely proportional to light intensity and reaches maximum at $\Omega \approx \sqrt{2\delta\gamma} = 3.8$ MHz (at $\gamma \gg \delta$), which corresponds to $I \approx 3$ mW/cm^2. Measurements showed that the rotation angle reached its maximum at the laser intensity $I = 20$ mW/cm^2 (Fig. 3), which is higher than the theoretical value obtained without regard for the Doppler broadening. Note, however, that the inhomogeneous broadening can be ignored at $\Omega \gg \sqrt{\Gamma/\gamma}\, W_D \approx 13$ MHz, which corresponds to $I \approx 35$ mW/cm^2.

Note that, since the $F = 2 \longrightarrow F' = 1$ transition is an open system, the population is optically pumped out to the $F = 1$ level under the action of electromagnetic wave, resulting in weakening of the Faraday effect. Evidently, the compensation of population pumping from the system should increase the Faraday rotation angle and improve the magnetic-field sensitivity at a fixed concentration of active atoms. This is particularly important for overcoming the sensitivity threshold associated with the influence of collisions and radiation imprisonment at high concentrations [4, 5, 11, 12].

To study the effect of optical pumping out, an auxiliary laser was used. It was tuned to the $F = 1 \longrightarrow F' = 2$ transition and pumped population from the $F = 1$ level to the $F = 2$ level via the upper $F' = 2$ level. The $F = 1 \longrightarrow F' = 2$ transition has no dark states, providing high efficiency of pumping. The beams of both lasers were superposed inside the vapor cell, and the intensity of the auxiliary laser was 70 mW/cm^2. The experiment was conducted with various intensities of the main laser and magnetic fields. The angle of rotation was increased approximately twofold.

These results agree with simple estimates. The rate of optical pumping out of the $F = 2 \longrightarrow F' = 1$ transition can be estimated at $\nu_{out} = \gamma n_1'$, where n_1' is the population of the upper $F' = 1$ level. Under conditions of coherent population trapping, the population of the upper level is $n_1' \approx \Gamma/\gamma$ and, correspondingly, the pumping rate is $\nu_{out} \approx \Gamma$. In the absence of the auxiliary laser, the rate of population recovery to the system is determined by the relaxation rate between the hfs sublevels. This rate is determined by the atomic time of flight through the laser beam and is equal approximately to the Zeeman coherence relaxation rate $\nu_{in} \approx \Gamma$. Thus, the rates of population outflow from the $F = 1$ level to the $F = 2$ level and back are approximately the same, $\nu_{in} \approx \nu_{out}$, and, hence, the level populations are also equal. On switching on the auxiliary laser tuned to the $F = 1 \longrightarrow F' = 2$ transition having no dark states, the population recovery rate increases substantially. As a result, almost the whole population undergoes transition to the $F = 2$ level, resulting in a twofold increase of the Faraday effect, as was observed in the experiment.

The above considerations are in agreement with the numerical calculations carried out for a three-level open system. The calculations show that the compensation of optical pumping in the range of low magnetic fields results in a twofold increase in the Faraday rotation angle. In addition, the linear field dependence of the rotation angle can be extended appreciably and, accordingly, the maximum attainable rotation angle can be increased upon choosing optimal radiation parameters and medium. The extension of the dynamic range is of great importance in fabricating optical magnetometers. The results of studying the influence of optical pumping out and its compensation on the Faraday rotation are rather cumbersome and will be reported in detail elsewhere.

One more specific feature of the nonlinear resonant Faraday effect is that the dichroism in the center of an inhomogeneously broadened line is totally absent, because the absorption coefficients for the right-hand and left-hand circular polarizations of electromagnetic wave are equal. Evidently, the lack of dichroism allows the accuracy of measuring magnetic field to be improved, which is particularly important for the optically dense media, where the absorption plays a significant role.

Our experiments demonstrate that the Faraday rotation angle depends nonmonotonically on the laser intensity and magnetic field. It turns out that the optimal light intensity exists (20 mW/cm^2 in our experiments) for which the angle of rotation is maximal. Measurements of the rotation angle as a function of magnetic field suggest that the sense of rotation of the polarization plane is different at high and low magnetic fields. The Zeeman splitting corresponding to a change in sign of the effect is equal approximately to the Rabi frequency of the light wave. The magnetic field at which the effect changes sign is virtually independent

of the atomic concentration and, hence, on the sample temperature.

It seems that the compensation of the population optical pumping out from the system is promising for the extension of dynamic range and improvement of accuracy of measuring magnetic field using the nonlinear resonant Faraday effect. A twofold increase of the effect has been demonstrated experimentally.

The results obtained open up new possibilities for using the phenomena of coherent population trapping and electromagnetically induced transparency in degenerate systems to solve applied problems. The design of a new generation of magnetometers seems to hold much promise.

We are grateful to P.M. Anisimov, R.L. Kolesov, E.A. Kuznetsova, A.G. Litvak, V.A. Mironov, and V.E. Semenov for helpful discussions. This work was supported by the Russian Foundation for Basic Research, project no. 01-02-17779.

REFERENCES

1. D. Budker, V. V. Yashcuck, and M. Zolotorev, Phys. Rev. Lett. **81**, 5788 (1998).
2. D. Budker, D. F. Kimball, S. M. Rochester, and V. V. Yashcuck, Phys. Rev. Lett. **83**, 1767 (1999).
3. V. A. Sautenkov, M. D. Lukin, C. J. Bendar, *et al.*, Phys. Rev. A **62**, 023810 (2000).
4. I. Novikova, A. B. Matsko, and G. R. Welch, Opt. Lett. **26**, 1016 (2001).
5. I. Novikova and G. R. Welch, J. Mod. Opt. **49**, 349 (2002).
6. E. Arimondo, Prog. Opt. **35**, 257 (1996).
7. A. B. Matsko, O. Kocharovskaya, Y. Rostovtsev, *et al.*, Adv. At., Mol., Opt. Phys. **46**, 191 (2001).
8. V. S. Smirnov, A. M. Tumaĭkin, and V. I. Yudin, Zh. Éksp. Teor. Fiz. **96**, 1613 (1989) [Sov. Phys. JETP **69**, 913 (1989)].
9. A. M. Tumaĭkin and V. I. Yudin, Zh. Éksp. Teor. Fiz. **98**, 81 (1990) [Sov. Phys. JETP **71**, 43 (1990)].
10. I. V. Zelensky and V. A. Mironov, Zh. Éksp. Teor. Fiz. **121**, 1068 (2002) [JETP **94**, 916 (2002)].
11. A. B. Matsko, I. Novikova, M. O. Scully, and G. R. Welch, Phys. Rev. Lett. **87**, 133601 (2001).
12. A. B. Matsko, I. Novikova, and G. R. Welch, J. Mod. Opt. **49**, 367 (2002).
13. M. Fleischauer, A. B. Matsko, and M. O. Scully, Phys. Rev. A **62**, 013808 (2000).

Translated by V. Sakun

JETP Letters, Vol. 76, No. 7, 2002, pp. 423–427. Translated from Pis'ma v Zhurnal Éksperimental'noĭ i Teoreticheskoĭ Fiziki, Vol. 76, No. 7, 2002, pp. 497–502.

Laser Cooling of Recombining Electron–Ion Plasma

A. P. Gavrilyuk, I. V. Krasnov*, and N. Ya. Shaparev

Institute of Computational Modeling, Siberian Division, Russian Academy of Sciences, Krasnoyarsk, 660036 Russia

** e-mail: krasn@icm.krasn.ru*

Received July 24, 2002; in final form, August 19, 2002

A method of producing and confining ultracold electron–ion plasma with a strongly nonideal ion subsystem is considered. The method is based on the laser cooling of plasma ions by the radiation resonant with the ion quantum transition. A model is developed for the laser cooling of recombining plasma. Computer simulation based on this model showed that the ion nonideality parameter can be as large as ~100. The data obtained demonstrate that the production of ultracold nonideal plasma is quite possible. © *2002 MAIK "Nauka/Interperiodica".*

PACS numbers: 52.58.–c; 32.80.Pj

In recent years, considerable interest has been expressed in studying ultracold plasma (UP) [1–13]. Experimental works on producing and studying plasmas at cryogenic temperatures (>4 K) were performed earlier and described in book [14]. Interest in such plasmas was mainly caused by the possibility of investigating various elementary processes with low-energy particles. It should be noted that the degree of ionization of plasma produced in these experiments was low ($<10^{-4}$).

In [2–4] the idea was proposed of producing and confining strongly ionized UP by resonance laser cooling and plasma ion localization. In spite of a low particle concentration ($<10^8$ cm^{-3}), the interparticle interaction in such plasma is relatively strong because of the low particle temperature. It is characterized by the nonideality parameter [15]

$$\Gamma_\alpha = \frac{e^2}{ak_BT_\alpha}, \quad a = \left(\frac{3}{4\pi N}\right)^{1/3},$$

where $\alpha = e$ or i, k_B is the Boltzmann constant, e is elementary charge, a is the mean interparticle distance, N is the particle (electron and ion) concentration, and T_α is the ion ($\alpha = i$) or electron ($\alpha = e$) temperature. For the ion subsystem, Γ_i can be much greater than unity. The respective electronic component may be weakly nonideal ($\Gamma_i \ll 1$), but its temperature is relatively low because of cooling due to the elastic collisions with ions, so that the Debye radius (determined by this temperature) is smaller than the size of cooled area, providing the necessary condition for the existence of electron–ion plasma.

Note that, despite the great progress in utilizing the laser-cooling and atom–ion localization methods [16, 17], recombining electron–ion plasma has not been studied in this context so far. One may anticipate that the extension of these methods to plasmas will assist in preparing new physical objects in laboratory conditions. In particular, a UP with strongly nonideal laser-cooled ionic component is among such objects. This plasma is of considerable interest due to the following reasons.

It is the natural physical implementation of the classical three-dimensional model, so-called one-component plasma (OCP) (ideal electron subsystem acts as a neutralizing background), which is widely used in theoretical studies of phase transitions in Coulomb systems [15]. For this reason, this system is a highly suitable object for the experimental study of the liquid–(Wigner)crystal transition [15] predicted by the OCP theory. The possibility of varying Γ_i in laboratory (by controlling laser parameters) is very important for studying the properties of phase states and transitions between them in quasi-neutral strongly ionized plasmas.

Interest in UP has been grown due to recent experiments [5–7], in which it was produced by near-threshold photoionization [18] of preliminarily cooled Xe atoms. The authors of experiments [5–7] assumed that the electron and ion temperatures were as low as 0.1 and even 10^{-3} K, respectively, for the concentrations of charged particles ~10^8–10^9 cm^{-3}; i.e., plasma should be strongly nonideal for both components. However, the experimental results ran counter to the assumption about very low particle temperature. In a number of subsequent works [8–13], these experiments were analyzed, and it was shown that the relaxation of both subsystems to the minimum-potential-energy state in times $\tau_e \sim \omega_e^{-1}$ and $\tau_i \sim \omega_i^{-1}$ (ω_e and ω_i are the electron and ion plasma frequencies) increases their kinetic energy by ~e^2/a, where a is the mean interparticle spacing. The corresponding nonideality parameters are Γ_e, $\Gamma_i \sim 1$. Further rise in electron temperature is caused by the recombination-induced heating. Therefore, this method allows one to produce UP with the nonideality parame-

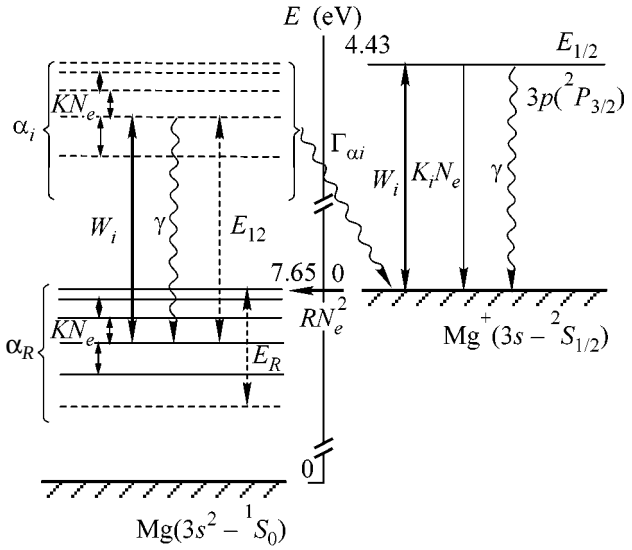

Fig. 1. Scheme of elementary processes: α_i and α_R are the autoionizing and Rydberg atomic states, respectively; E_{12} is the ion excitation energy; E_R is the energy [22] above which the electron-impact-induced de-excitation rate is higher than the spontaneous decay rate. The following processes are also shown: W_i are the laser-induced transitions; KN_e denote the electron–atom inelastic collisions; K_iN_e is the electron-impact-induced ion de-excitation; RN_e^2 is the three-particle recombination; Γ_{ai} is the autoionization decay; and γ is the spontaneous decay of an excited ion.

ter <1 and the lifetime less, at least, than the plasma expansion time.

In our opinion, the combination of two methods—creation of initial UP by near-threshold photoionization followed by laser cooling and ion localization by resonant radiation—is the promising method of producing long-lived UP with strongly nonideal ion subsystem. Such is the case, because the ion heating upon the relaxation to equilibrium distribution is compensated by laser cooling while the plasma expansion is prevented by the ion localization in optical trap and, correspondingly, electron localization by the light-induced ambipolar potential [2, 19].

Note also that the ion-cooling laser radiation affects not only the translational but also the ion internal degrees of freedom. The formation of excited ions initiates a number of elementary processes that complicate the plasma cooling pattern. In particular, the superelastic electron collisions with excited ions and the formation of Rydberg atoms and autoionizing states in the recombining UP are such processes.

In this work, computer simulation was carried out for the plasma laser-cooling dynamics with the aim of determining the range of attainable UP parameters.

Let us consider a "cold" rarefied plasma with a particle temperature of <100 K and a concentration of $<10^9$ cm^{-3}, which can be produced by near-threshold photoionization. Considering the results of works [11–13], we assume that initial temperatures satisfy the condition $\Gamma_e < 1$ and $\Gamma_i \sim 1$. Let the plasma be exposed to the monochromatic radiation [in the form of standing wave with amplitude $E = E_0\cos(k\mathbf{lr})$ along the $\mathbf{l}$ direction] quasi-resonant with the quantum transition of plasma ions and having frequency ω red-shifted from the resonance frequency ω_{21}: $\omega - \omega_{21} = \Delta < 0$. Then the friction force acting on ions in the weak-saturation $|V| \ll \gamma, |\Delta|$ and slow-ion $\gamma \gg k\sqrt{\varepsilon_i/m_i}$ case can be written as [20]

$$\mathbf{F} = m_i\chi(\mathbf{vl})\mathbf{l}, \qquad \chi = \frac{\hbar k^2\gamma\Delta|V|^2}{m_i(\Delta^2 + \gamma^2/4)^2}, \qquad (1)$$

where m_i is the ion mass, χ is the friction coefficient, V is the Rabi frequency, γ is the ion excited-state spontaneous-decay rate, and $\mathbf{v}$ is the ion velocity.

The conditions

$$\gamma \gg \omega_i; \quad \tau \ll \tau_0$$

are considered, where $\tau = \max(\nu_{ii}^{-1}, \omega_i^{-1})$, ν_{ii} is the frequency of elastic interion collisions, and $\tau_0 = \chi^{-1}$ is the ion cooling characteristic time.

Due to the elastic collisions with ions, electrons are also cooled, but the electron cooling rate is lower than that of ions if $\tau_0 < (m_e\nu_{ei}/m_i)^{-1}$ (m_e is electron mass and ν_{ei} is the frequency of elastic ion–electron collisions). As a result, the ion subsystem may be strongly nonideal ($\Gamma_i \gg 1$), with the electron state remaining weakly nonideal. Despite the low concentrations, the three-particle recombination rate is high, because the initial particle temperatures are low. Besides, this recombination is distinctive in that the electron is captured to highly excited (Rydberg) atomic levels followed by their electron-impact de-excitation down along the energy axis.

As a result, the cooling irradiation remains resonant with the ion core of the formed Rydberg atom, and the atom undergoes transition to the autoionizing state upon core excitation. This results in the situation corresponding to the method of producing autoionizing states by the "excitation of isolated core" [21].

The subsequent autoionizing atomic decay again results in the formation of an ion and an electron, thereby preventing the recombination. Figure 1 is the schematic of the main elementary processes involved in our model.

As a result of autoionization and superelastic electron collisions with excited ions, hot electrons appear with energy ε_h equal to the resonance ion-transition the energy E_{12} appreciably higher than the kinetic energy ε_e of thermalized electrons. This results in the formation of two groups of electrons, because the energy exchange between them is hampered due to small elastic-scattering cross sections $\sigma_{ee} \sim \varepsilon_h^{-2}$. The formation of

hot electrons also brings about recoil-induced ion heating. The recoil energy is $\varepsilon_r \approx m_e E_{12}/m_i$.

Apart from the above-mentioned processes, there are some other processes influencing the ion kinetic energy. Among these are ion heating caused by the quantum fluctuations of radiative forces [20] and decrease in the ion kinetic energy as a result of weakening interparticle Coulomb interaction in the recombination.

Plasma dynamics depends on the size of the region and the way of localization. In our opinion, a purely optical trap based on the use of rectified gradient forces in bichromatic laser fields is most promising for the localization [23], because it is free from the disadvantages inherent in the traditional plasma magnetic confinement methods (magnetohydrodynamic instabilities are possible in nonuniform magnetic fields). The depth U_0 of such a trap can be as large as ~10 K [23]. If the characteristic trap size $L \ll \lambda_h$, where λ_h is the mean free path of hot electrons, the latter will freely escape the trap (in the ambipolar regime with the same number of ions). Although this reduces plasma concentration, the contribution of these electrons to the heating of the remaining thermalized electrons can be ignored. In what follows, the conditions

$$\varepsilon_e < U_0, \quad \varepsilon_h \gg U_0, \quad \varepsilon_r > U_0 \tag{2}$$

are assumed to be fulfilled. This signifies that the thermalized electrons with mean kinetic energy ε_e are confined in the trap, while the hot electrons freely escape it.

With allowance for this, the dynamics of mean kinetic energies ε_e and ε_i of the thermalized electrons and ions and their concentrations N_e and N_i can be described by the set of equations

$$dN_e/dt = -j_0 - K_i N_e N_{2i}; \tag{3}$$

$$N_{2i} \approx \frac{|V|^2}{\Delta^2 + (\gamma/2)^2} N_i, \quad N_i = N_e; \tag{4}$$

$$\frac{d\varepsilon_e}{dt} = Q_r - \frac{2m_e}{m_i}\nu_{ei}(\varepsilon_e - \varepsilon_i); \tag{5}$$

$$Q_r = (\varepsilon_e + E_R) j_0 - \sum_{n_R}^{n_c} (E_R - E_n)\Gamma_n; \tag{6}$$

$$\frac{d\varepsilon_i}{dt} = \frac{2m_e}{m_i}\left(K_i N_{2i} + \sum_{n_R}^{n_c}\Gamma_n\right)\frac{E_{12}}{N_i} + \Lambda + \frac{2m_e}{m_i}\nu_{ei}(\varepsilon_e - \varepsilon_i) - \frac{d(U_i N_i)}{N_i dt} - \chi\varepsilon_i, \tag{7}$$

where j_0 is the classical [24] recombination flux. The second term on the right-hand side of Eq. (3) accounts for the escape of thermalized electrons to the group of hot electrons through the superelastic collisions with excited ions, where K_i is the electron-impact ion-deexcitation rate constant, and N_{2i} is the concentration of excited ions. It is described by Eq. (4), which is obtained in the quasi-stationary approximation valid under the condition

$$\gamma \gg \tau_r^{-1}, \tau_h^{-1}, \tag{8}$$

where τ_r is the characteristic recombination time and τ_h is the characteristic time of electron recombinational heating. Our estimates show that condition (8) is fulfilled for the concentrations $N_e = 10^5$–10^9 cm^{-3} and $\Gamma_e \sim 0.1$. In Eq. (5), the first term on the right-hand side accounts for the electron recombinational heating with the transition of some Rydberg atoms to the decaying autoionizing states; Γ_n is the number of atoms excited in unit time from the state with principal quantum number n to the appropriate autoionizing state (ICE mechanism) followed by the decay of the latter; E_R is the energy above which the electron-impact-induced deexcitation rate is higher than the spontaneous decay rate; E_n is the electron binding energy in the nth state; n_c corresponds to the upper limit of bound states; and $n_R = \sqrt{\mathrm{Ry}/E_R}$. The second term is responsible for the energy exchange in elastic collisions of thermalized electrons and ions (as shown in [25], the pair-collision approximation can be used for weakly nonideal electron subsystem for an arbitrary value of Γ_i) with frequency ν_{ei}. The first term for the ion kinetic energy on the right-hand side in Eq. (7) describes the ion heating by virtue of the recoil energy arisen in the formation of hot electrons; $\Lambda = (\hbar k)^2\gamma^2|V|^2/[2m_i(\Delta^2 + \gamma^2/4)]$ describes the ion heating due to quantum fluctuations of radiative forces [20]; $U_i = -\xi e^2/a$ [26] is the potential energy of interacting ions ($\xi \sim 1$); and the corresponding term in Eq. (7) accounts for a change in this energy in recombination. The value of Γ_n was determined in the weak-field limit from the population balance equations for autoionizing states in the quasistationary approximation, whose validity follows from condition (8). In so doing, the model of fast mixing between the states with different orbital quantum numbers l, the condition $\Gamma_n \ll j_0$, and the features in the dependence of the autoionization rate Γ_{nl} [27] on l were used.[1] In the model considered, $\Gamma_n = \Gamma_n(|V|, \Delta, \gamma, N_e, \Gamma_{nl})$ is a function of field parameters, characteristics of ion quantum transition, concentration of thermalized electrons, and a functional of autoionization rate Γ_{nl} and j_0 is expressed by the classical formula.

Since electrons in the course of ion cooling are heated due to three-particle recombination (Γ_e decreases, as is confirmed by the numerical experi-

[1] With an increase in l at a fixed n, the autoionization rate Γ_{nl} rapidly decreases (by several orders of magnitude) and the contribution to Γ_n comes only from the states with $l \le l_{\max}$ ($l_{\max} \lesssim 10$) [27, 28], so that one may put $\Gamma_{nl} = 0$ at $l > l_{\max} \ll n$).

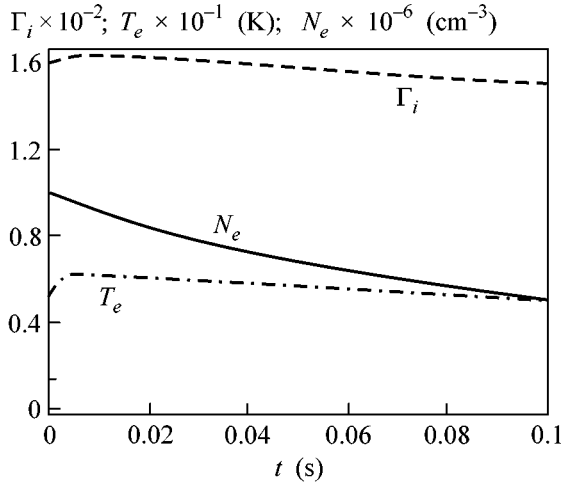

Fig. 2. Dynamics of plasma parameters for $N_0 = 10^6$ cm^{-3}, $\Delta = 2 \times 10^9$ s^{-1}, and electron initial energy $\varepsilon_{e0} = 1$ K.

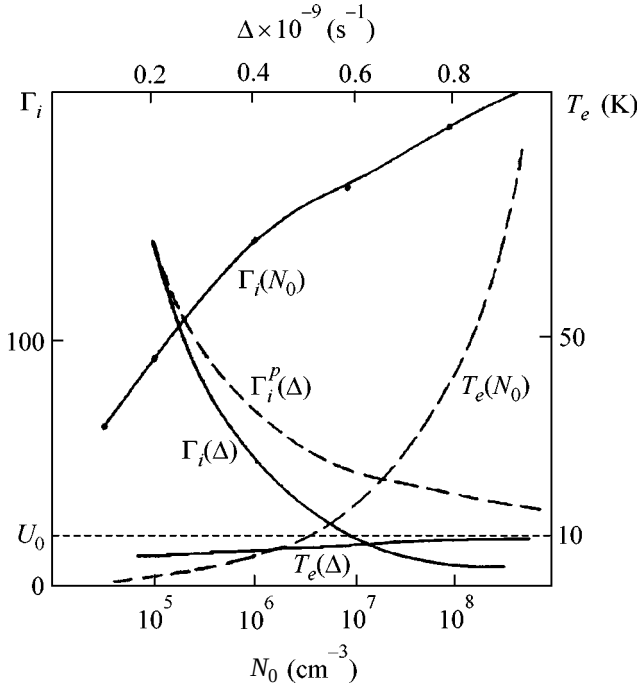

Fig. 3. The nonideality parameter and the electron temperature as functions of N_0 (for $\Delta = 2 \times 10^8$ s^{-1}) and Δ (for $N_0 = 10^6$ cm^{-3}).

ments), they can be considered weakly nonideal and forming ion-neutralizing background.

Computer simulation of model (3)–(7) was carried out for the Mg ions with the initial concentration $N_0 = 10^9$–10^5 cm^{-3}, detuning $\Delta = 2 \times 10^8$–10^9 s^{-1}, and Rabi frequency $|V| = 10^8$ s^{-1}.

Figure 2 demonstrates the dynamics of plasma parameters (Γ_i, ε_e, N_e) in the course of cooling. It turned out that quasistationary values of parameters are established in a relatively short time ($<10^{-4}$ s) and then slowly change because of a decrease in plasma concentration as a result of the escape of hot particles (main reason) and the recombination. Despite the low initial electron temperature, the recombination plays a considerable role only at the initial moment. Because of the fast recombinational electron heating, the rate decreases rapidly and the escape of hot particles from the cooling region plays the main role. Note that a high $\Gamma_i \sim 160$ value is achieved in a rather short time, after which it changes only slightly upon decreasing plasma concentration.

The nonideality parameter is shown in Fig. 3 as a function of concentration $\Gamma_i(N_0)$ and detuning $\Gamma_i(\Delta)$. The Γ_i values correspond to the time $t = 0.1$ s. Similar dependences for the maximal electron temperature are also shown in the figure. One can see that the character of $\Gamma_i(N_0)$ dependence alters at $N_0 \geq 10^6$ cm^{-3}, because the processes change their roles: at small N_0, the "fluctuation" heating mainly limits the ion cooling; as N_0 increases, the electron–ion energy exchange becomes dominant. A change in the roles of processes is also manifested by the deviation of the $\Gamma_i(\Delta)$ dependence from the $\Gamma_i^p(\Delta) \sim 1/|\Delta|$ dependence obtained for $|\Delta| > \gamma$ on the assumption that fluctuation heating dominates.

The dependences shown in Fig. 3 can be used to determine the range of N_0 values that are admissible for the plasma localization in a trap with depth U_0. For example, the concentrations $N_0 \leq 3 \times 10^6$ cm^{-3}, for which the maximal temperature of thermal electrons does not exceed 10 K, are admissible for $U_0 = 10$ K. Nevertheless, $\Gamma_i \sim 150$ can be attained even in such a rarefied plasma.

Our studies have shown that the plasma laser cooling is a rather complicated phenomenon, whose specificity is caused by the low energies of charged particles, action of resonance radiation on both translational and internal degrees of freedom of particles and by the plasma localization in trap. Of special note is the stabilizing role of the trap. In the absence of the trap, the plasma would decay, due to its expansion, in a time on the order of 10^{-3}–10^{-4} s (even at $T \leq 10$ K).

Our computer simulation has demonstrated that plasma laser cooling in an optical trap is an efficient method of producing long-lived ultracold plasma with a strongly nonideal ion subsystem, which can be used in laboratory studies of phase transitions in the coulombic systems. Note also that the specificity of the elementary processes occurring in cooled plasma allows the use of this method for the formation of Rydberg and autoionizing atomic states and the study of the recombination processes in as yet poorly explored low-tem-

perature and low-concentration ranges and the properties of nonideal plasma.

This work was supported by the Russian Foundation for Basic Research, project no. 99-02-16873.

REFERENCES

1. L. I. Men'shikov and P. O. Fedichev, Zh. Éksp. Teor. Fiz. **108**, 144 (1995) [JETP **81**, 78 (1995)].
2. A. P. Gavrilyuk, I. V. Krasnov, and N. Ya. Shaparev, Pis'ma Zh. Éksp. Teor. Fiz. **63**, 316 (1996) [JETP Lett. **63**, 324 (1996)].
3. A. P. Gavrilyuk, I. V. Krasnov, and N. Ya. Shaparev, Pis'ma Zh. Tekh. Fiz. **23** (2), 28 (1997) [Tech. Phys. Lett. **23**, 61 (1997)].
4. A. P. Gavrilyuk, I. V. Krasnov, and N. Ya. Shaparev, Laser Phys. **8**, 653 (1998).
5. T. C. Kilian, S. Kulin, S. D. Bergeson, *et al.*, Phys. Rev. Lett. **83**, 4776 (1999).
6. S. Kulin, T. C. Kilian, S. D. Bergeson, *et al.*, Phys. Rev. Lett. **85**, 318 (2000).
7. T. C. Kilian, M. J. Lim, S. Kulin, *et al.*, Phys. Rev. Lett. **86**, 3759 (2001).
8. A. N. Tkachev and S. I. Yakovlenko, Pis'ma Zh. Éksp. Teor. Fiz. **73**, 71 (2001) [JETP Lett. **73**, 66 (2001)].
9. M. P. Robinson, B. Laburthe Tolra, M. W. Noel, *et al.*, Phys. Rev. Lett. **85**, 4466 (2000).
10. A. N. Tkachev and S. I. Yakovlenko, Kvantovaya Élektron. (Moscow) **31**, 1084 (2001).
11. S. Mazevet, L. A. Collins, and J. D. Kress, Phys. Rev. Lett. **88**, 055001 (2002).
12. F. Robicheaux and J. D. Hanson, Phys. Rev. Lett. **88**, 055002 (2002).
13. S. G. Kuzmin and T. M. O'Neil, Phys. Rev. Lett. **88**, 065003 (2002).
14. E. I. Asinovskiĭ, A. V. Kirillin, and A. A. Rakovets, *Cryogenic Charges* (Nauka, Moscow, 1988).
15. S. Ichimaru, Rev. Mod. Phys. **54**, 1017 (1982).
16. M. H. Anderson, J. R. Ensher, M. R. Matthews, *et al.*, Science **269**, 198 (1995).
17. P. É. Toshek, Usp. Fiz. Nauk **158**, 451 (1982).
18. S. I. Yakovlenko, Kvantovaya Élektron. (Moscow) **19**, 5 (1992).
19. S. A. Gavrilyuk, I. V. Krasnov, S. P. Polyutov, and N. Ya. Shaparev, in *Proceedings of the 5th Russian–Chinese Symposium on Laser Physics and Technologies, Tomsk, Russia, 2000* (Tomsk State Univ., Tomsk, 2001), p. 56.
20. A. P. Kazantsev, G. I. Surdutovich, and V. P. Yakovlev, *The Mechanical Action of Light on Atoms* (Nauka, Moscow, 1991).
21. W. E. Cooke, T. F. Gallagher, S. A. Ebelstein, *et al.*, Phys. Rev. Lett. **40**, 178 (1978).
22. L. M. Biberman, V. S. Vorob'ev, and I. T. Yakubov, *Kinetics of Nonequilibrium Low-Temperature Plasmas* (Nauka, Moscow, 1982; Consultants Bureau, New York, 1987).
23. A. P. Kazantsev and I. V. Krasnov, Pis'ma Zh. Éksp. Teor. Fiz. **46**, 264 (1987) [JETP Lett. **46**, 332 (1987)].
24. A. V. Gurevich and L. P. Pitaevskiĭ, Zh. Éksp. Teor. Fiz. **46**, 1281 (1964) [Sov. Phys. JETP **19**, 870 (1964)].
25. G. Hazak, Z. Zinamon, Y. Rosenfeld, and M. W. C. Dharma-Wardana, Phys. Rev. E **64**, 066411 (2001).
26. V. S. Vorob'ev and A. A. Likal'ter, *Chemistry of Plasma* (Énergoatomizdat, Moscow, 1989).
27. L. A. Vaĭnshteĭn and V. P. Shevel'ko, *Structure and Characteristics of Ions in Hot Plasma* (Nauka, Moscow, 1986).
28. J. Li and Y. Hahn, Z. Phys. D **41**, 19 (1997).

Translated by V. Sakun

JETP Letters, Vol. 76, No. 7, 2002, pp. 428–432. Translated from Pis'ma v Zhurnal Éksperimental'noĭ i Teoreticheskoĭ Fiziki, Vol. 76, No. 7, 2002, pp. 503–507.

Cavitation Model of Micropoint Explosion

V. S. Vorob'ev[1, *], S. P. Malyshenko[2], and S. I. Tkachenko[1]

[1] *Institute of Thermal Physics of Extremal States, Russian Academy of Sciences, Moscow, 127412 Russia*

[2] *Institute of High Temperatures, Russian Academy of Sciences, Izhorskaya ul. 13/19, Moscow, 127412 Russia*

**e-mail: vrbv@mail.ru*

Received July 15, 2002; in final form, August 21, 2002

In a strong electric field, liquid metal of a micropoint is in the extended metastable state. At a certain degree of superheating, rapidly growing vapor bubbles arise spontaneously in it (vapor cavitation or explosive boiling), leading to the explosion of the micropoint. The resulting mixture of droplets in vapor expands with a high velocity to transform into plasma bunches. The field dependences obtained with this model for the explosion delay time and for the droplet size agree qualitatively with the experimental data for tungsten micropoints. © *2002 MAIK "Nauka/Interperiodica".*

PACS numbers: 64.70.Fx; 64.60.My

It was established by Mesyats *et al.* [1, 2] that, if the electric field strengthens locally in the vicinity of a micropoint, explosive electron emission is preceded by microexplosions of the point tip. At the current density $j > 10^8$ A/cm^2, the micropoint at the cathode surface acquires an energy of ~10^4 J/g, after which it explodes. This is accompanied by the transformation of field-emission current into the explosive electron-emission current with the formation of a crater at the cathode. In [3–6], the electrohydrodynamic processes occurring in the plasma state after the destruction of cathode micropoint were considered. The possible role of metal superheating in the microexplosion was discussed in [7]. However, the physical nature of the processes leading to microexplosions (ectons) at the cathode surface was still not fully understood. The authors of [1, 2] showed that the processes occurring in the wire electric explosion are closely related to the explosive electron emission. Experiments [1, 2] suggest that an external electric field plays the decisive role in the micropoint explosion: a less than twofold change in the field strength changes the microexplosion delay time by seven orders of magnitude.

A two-phase liquid–vapor system in an external field becomes thermodynamically unstable at a certain critical field strength [8] and undergoes transition, through phase explosion, to a new state with a different configuration, namely, to a finely dispersed phase mixture. In the case of wire explosion, a vapor in equilibrium with the conductor compressed by the Ampere forces is supersaturated with respect to the liquid without current. For this reason, liquid-phase nuclei with critical radius can spontaneously arise in this vapor at a certain degree of supersaturation (magnetic field), thereby destabilizing the "conducting liquid-metal core–vapor" system and inducing its explosive transformation into a rapidly expanding finely dispersed mixture of liquid droplets in vapor [8–11]. In contrast to the explosion of thin wires, the explosion of micropoints occurs in a strong electric field, which induces, at the liquid–gas interface, surface electric force directed toward the vapor and, hence, extending metal. Because of this, liquid conductor appears in the extended (superheated) metastable state. At a certain field strength and degree of superheating, rapidly grown vapor bubbles arise spontaneously, and the cavitation (explosive boiling or cavitation; see [12, 13] for detail) with pressure impulse occurs in the micropoint liquid. The micropoint breaks and transforms into the expanding finely dispersed mixture of droplets in vapor, from which plasma bunches are subsequently formed and flow toward the anode. Experimental data [14] confirm the presence of such droplets in the micropoint explosion products. The cavitation micropoint explosion model explains the experimentally observed [1, 2] sharp decrease in the delay time between the impulse and explosion upon a small increase in the field strength and allows one to estimate the size of liquid droplets and the value of post-explosion current.

Figure 1 presents the experimental data from [1, 2]. The explosion delay time was measured as a function of field strength at micropoints with radii of curvature $R \sim (0.05–0.3)$ μm. Measurements were made in the range $E \sim (70–130)$ MV/cm with current densities $(4.5–220) \times 10^7$ A/cm^2. After the micropoint explosion, the discharge current increased from ~10^{-2} to ~1 A.

Let the micropoint be a liquid-metal cylinder of length l and radius R and have spherical tip. At the interface of two magnetically inactive media (liquid and gas), in which the electric field and current are perpen-

dicular to the interface, the equilibrium is described by the equations

$$\mu_l - \frac{E_l^2}{8\pi}\left(\frac{\partial\varepsilon_l}{\partial\rho}\right)_T + \frac{\Delta p_M}{\rho_l} = \mu_g - \frac{E_g^2}{8\pi}\left(\frac{\partial\varepsilon_g}{\partial\rho}\right)_T, \quad (1)$$

$$p_l - \frac{E_l^2\rho_l}{8\pi}\left(\frac{\partial\varepsilon_l}{\partial\rho}\right)_T - p_g + \frac{E_g^2\rho_g}{8\pi}\left(\frac{\partial\varepsilon_g}{\partial\rho}\right)_T = F_\gamma + F_E. \quad (2)$$

The index l refers to liquid and g refers to gas. Equation (1) is the condition for the constancy of chemical potential along both media. In Eqs. (1) and (2), E is the electric field strength; μ, ε, and ρ are the chemical potential, the dielectric constant, and the substance density, respectively; and Δp_M is the addition to the liquid pressure from the Ampére forces. For a cylindrical rod, $\Delta p_M = \mu_0 j^2 R^2/4$, where μ_0 is the magnetic constant and j is the current density. The corresponding term for the gas phase is negligible because of the low current density in it.

Equation (2) relates the liquid and gas pressures p at the interface to each other. Here, $F_\gamma = 2\gamma/R$ is the capillary pressure for a micropoint with spherical curvature and F_E is the surface electric force at the interface of two media with different dielectric constants; it is directed toward the medium with the smaller value of this constant. The surface tension $\gamma(T) = \gamma_0(1 - T/T_c)^\theta$ was determined from the data in [15] (T_c is the critical temperature and $\theta = 1.25$ is the critical index). For the perpendicular force, one has

$$F_E = \frac{\varepsilon_g - \varepsilon_l}{8\pi\varepsilon_l} E_g^2 \varepsilon_g. \quad (3)$$

Linearizing the chemical potentials in Eq. (1) with respect to pressure in the vicinity of p_s (p_s is the equilibrium pressure in the absence of fields and surface curvature), one obtains

$$p_l = p_s + \frac{E_l^2\rho_l}{8\pi}\left(\frac{\partial\varepsilon_l}{\partial\rho}\right)_T + \frac{\rho_l(F_\gamma + F_E) + \rho_g\Delta p_M}{\rho_l - \rho_g}, \quad (4)$$

$$p_g = p_s + \frac{E_g^2\rho_g}{8\pi}\left(\frac{\partial\varepsilon_g}{\partial\rho}\right)_T + \frac{\rho_g(F_\gamma + F_E + \Delta p_M)}{\rho_l - \rho_g}. \quad (5)$$

Below, we restrict ourselves to the case where one of the media is a liquid metal and the other is a nonpolarizable weakly conducting vapor with $\varepsilon_g \cong 1$. In this case, the contribution of the electrostriction forces to the pressure and chemical potential can be ignored, and expression (3) for the surface electric force (3) takes the form

$$F_E \cong -E_g^2/8\pi. \quad (6)$$

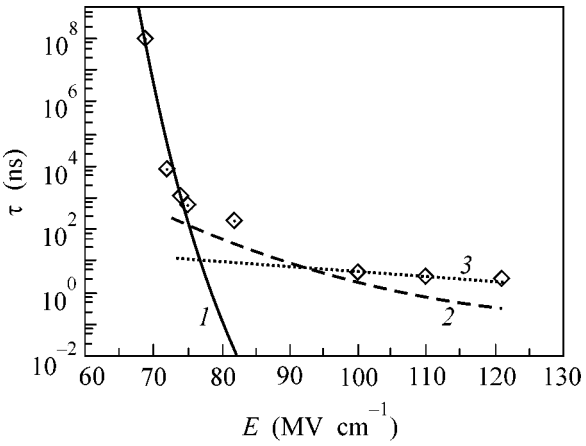

Fig. 1. Emitter explosion time as a function of electric field strength at the micropoint. Curve (*1*) is the expectation time for the nucleus appearance in liquid phase; curve (*2*) is the time of heating emitter to a temperature of ~1.3×10^4 K; curve (*3*) is the time of reaching steady-state nucleation, as calculated by Eq. (13). Rhombi denote the experimental data from [1, 2].

The field strength in liquid metal can be estimated using Ohm's law $E_l = j/\sigma_l$. Taking $\sigma_l \sim 0.7 \times 10^5$ S/m, one obtains $E_l \leq 3$ MV/cm; this value is appreciably lower than the field strength near the tip. The estimates of the contributions from different media to the phase pressures in experiments [1, 2] suggest that the main contribution comes from the surface electric force F_E, which produces high negative pressures exceeding the contribution of the capillary Ampére forces by more than an order of magnitude. Because of this, the pressure in liquid metal is much lower than its equilibrium value p_s; i.e., the metal is in a extended metastable state. At the initial moment, the surface electric force applied to the micropoint tip produces an unloading wave in the micropoint. The characteristic size of the extended region is ~$u_s\tau$, where u_s is the sound velocity and τ is the delay time. Since, for the micropoint length $l <$ (10–15)R, the micropoint has time to unload along its entire length during the experiment, the volume of metastable liquid is comparable with the micropoint volume.

The pressure–chemical potential phase diagram for the states of micropoint metal and surrounding vapor in Fig. 2 is constructed using the semiempirical equation of state for tungsten [16] at $T \sim 1.2 \times 10^4$ K. The line b is a binodal; *ig* and *il* are the chemical potential isotherms for the gas and liquid, respectively. The point of intersection of the lines *ig* and *il* corresponds to the liquid–gas equilibrium at pressure p_s and chemical potential μ_s in the absence of current and electric field.

The horizontal line in Fig. 2 corresponds to the total chemical potential uniform across the whole system in equilibrium. The black points *1*, *2*, and *3* are the states of the liquid metal micropoint in electric fields E = 120, 100, and 70 MV/cm, respectively. The metal pressure at

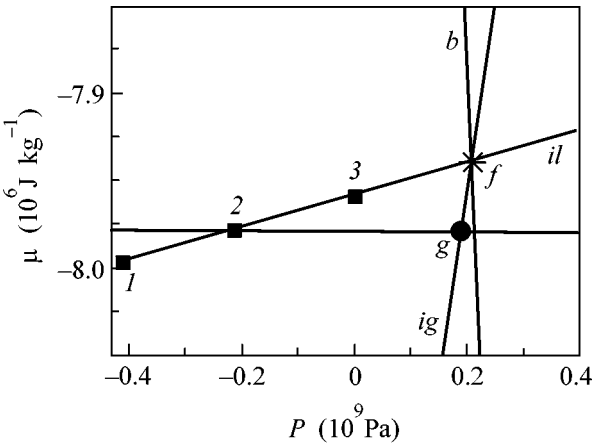

Fig. 2. The tungsten phase diagram in the μ–*P* plane.

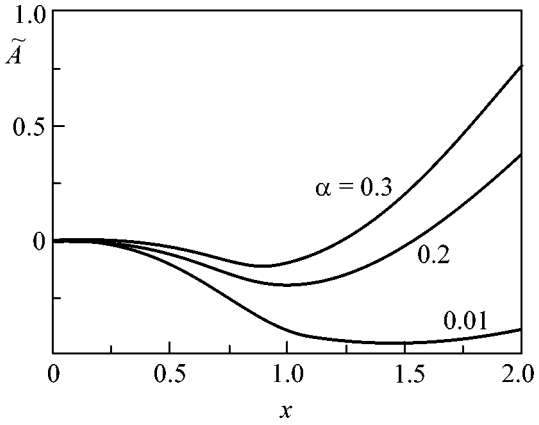

Fig. 3. Typical plots of the work of formation for the phase nucleus vs. the dimensionless radius for the parameters α = 0.01, 0.2, and 0.3.

these points is appreciably lower than the equilibrium pressure p_s. The point *g* denotes the gas state in equilibrium with metal. The chemical potentials of liquid metal and gas are equal, but the phases of the substance are at different pressures (the difference is mainly caused by the surface electric force).

The electric field strength inside the metal is low compared to the external strength. In such a situation, both the vapor surrounding the micropoint and occurring in a strong electric field and the gas bubble of critical radius arising inside the liquid-metal micropoint, where the field is nearly zero, may be in equilibrium with the superheated metal. The vapor pressure and chemical potential in such a bubble should coincide with those outside the micropoint.

Let a bubble of radius *a* arise near the micropoint tip with the initial radius *R*. Due to the low compressibility of liquid, the micropoint slightly thickens, its radius of curvature increases, and the field strength decreases at the tip. Because of this, the field strength changes when the bubble forms, according to the expression

$$E \cong E_0/(1 + a^3/R^3)^{4/3}, \tag{7}$$

where $E_0 = E_g$ is the field strength at the micropoint in the absence of a bubble.

The pressure difference $\Delta p = p_g - p_l$ between the vapor in the bubble and the liquid is given by Eqs. (4) and (5). If the electric field dominates, one can write $\Delta p \approx E^2/8\pi$. The work necessary for the formation of a bubble with radius *a* in the extended superheated micropoint liquid is found from the relation

$$A = 4\pi\gamma a^2 - \frac{a^3 E_0^2}{6}\frac{R^4}{(a^3 + R^3)^{4/3}}. \tag{8}$$

It is convenient to introduce the dimensionless radius $x = a/R$ and the dimensionless work $\tilde{A} = 6A/R^3E_0^2$. Then one has from Eq. (8)

$$\tilde{A} = \frac{\alpha x^2}{2} - \frac{x^3}{(1 + x^3)^{4/3}}, \tag{9}$$

where $\alpha = 48\pi\gamma/RE_0^2$ is the dimensionless parameter. In the experimental conditions of works [1, 2], this parameter does not exceed few hundredths.

It follows from Eqs. (8) and (9) that the equation determining the extreme points for x_c takes the form

$$\alpha = x_c\frac{3 - x_c^3}{(1 + x_c^3)^{7/3}}. \tag{10}$$

The dependence of the dimensionless work on the dimensionless radius *x* is shown in Fig. 3 for different values of parameter α. At $x \ll 1$, the curve has a weak maximum, which almost disappears in high fields. The maximum point corresponds to the critical radius and work

$$a_c \cong \frac{16\pi\gamma}{E_g^2}, \quad A_c \cong \frac{2^{10}\pi^3\gamma^3}{3E_g^4}. \tag{11}$$

One can see that the work of formation of the critical bubble decreases drastically with increasing field strength near the micropoint.

Every bubble with radius larger than a_c grows with a high rate. This growth is restricted by the radius corresponding to the minimum of function $\tilde{A}$ in Fig. 3. In the range of parameter α considered, the maximum occurs at $x \geq 1$. In this range, the vapor bubbles grow to

a size that exceeds the initial micropoint radius. By this instant of time, the micropoint should be destroyed.

Let us estimate the instant of time at which a viable vapor nucleus appears in the superheated metastable liquid of volume V. The mean expectation time τ for the appearance of such a nucleus is ordinarily written as [17]

$$\tau = (BnV)^{-1}\exp G, \quad (12)$$

where $G = A_c/kT$ is the Gibbs number, n is the number of nucleation centers in a unit volume (the parameters for the liquid–vapor phase equilibrium curve for tungsten were taken in accordance with the semiempirical equation of state given in [16]), and $B \approx 10^{10}$ s^{-1} is the kinetic factor.

The dependence of τ on the field strength (solid curve) is drawn in Fig. 1 for the volume $V \approx 10\pi R^3$ and the number of cavitation centers determined by the metal density. The micropoint temperature in [1, 2] was not measured, so that we chose the value $T \sim 13 \times 10^3$ K from the condition of best fit to the experimental data. At this temperature, growing vapor bubbles appear near the micropoint tip. Our calculation adequately describes the steepest left portion of the delay-time vs. field-strength curve. The right portion of this curve changes much slower with changing field strength. However, at high field strengths, the total delay time can be controlled by the time it takes to establish steady-state nucleus flow [17, 18]. According to the theory in [19], it can be determined from the relation

$$\tau_d = \frac{2\pi\rho_g a_c^2}{mB}\sqrt{\frac{kT}{\gamma}}, \quad (13)$$

where m is the tungsten atomic mass. The delay time may also be determined by the time it takes for the micropoint to be heated to the temperature corresponding to the onset of fast bubble grow. The latter time can be estimated from the formula

$$\tau_h \approx c_p\rho_l T\sigma_l/j^2, \quad (14)$$

where c_p is the heat capacity of liquid metal. Lines *2* and *3* in Fig. 1 correspond to these times.

At low field strengths, the expectation time τ for the appearance of vapor bubbles in metal is much longer than all other times, so that it controls the total delay time. As the field strength increases, the time τ rapidly decreases and becomes much shorter than the time τ_h and, next, than τ_d. Accordingly, the delay time for the moderate electric-field strengths (from the field range considered) is close to τ_h and, for higher fields, it is close to τ_d.

The cavitation destruction transforms the micropoint into a finely dispersed sol, whose droplets fly apart from the micropoint. After the dispersion of the micropoint, the field near its surface decreases substantially and becomes $E_f \sim RE_g/l$. The droplet size a_f after the micropoint destruction can be estimated from the relation $a_f = 16\pi\gamma/E_f^2$. In this case, the surface electric force is balanced out by the capillary pressure ($F_\gamma = F_E$). For the field strengths E_g = 120, 100, and 70 MV/cm, the droplet radii are, respectively, $a_f \sim$ (0.9, 1.3, 2.6) $\times 10^{-5}$ cm. These values correlate with the experimental data in [2], where the range of most frequently observed droplet radii was found to be (0.1–1.5) $\times 10^{-5}$ cm. The number of droplets formed after the micropoint explosion can be estimated at $N \sim 3R^2l/4a_f^3$. For the above-mentioned R and a_f values, seven or eight droplets appear from a single micropoint.

The commonness of the phenomena experimentally observed in [1, 2] in the explosions of a current-carrying conductor and a micropoint is explained by the thermodynamic instability of a two-phase "liquid conductor–vapor" system in an external field. At the same time, there are certain distinctions: in the first case, the stability limit is reached for a superheated vapor [8–11], whereas in the second case it is reached for a extended liquid, but in both cases this results in the explosive dispersion of the system and ensuing decrease in the strength of external field.

The model developed in this paper, although it does not lay claim to the complete description of such a complex phenomenon as the transformation of field emission into the explosive electron emission, allows one to obtain the experimentally observed steep dependence of the explosion expectation time as a function of the field strength at the micropoint and the droplet size after the explosion.

We are grateful to V.E. Fortov for valuable remarks. This work was supported by the Russian Foundation for Basic Research, project nos. 02-02-17255, 02-02-17376, and 00-15-96529.

REFERENCES

1. G. K. Kartsev, G. A. Mesyats, D. I. Proskurovskiĭ, *et al.*, Dokl. Akad. Nauk SSSR **192**, 309 (1970) [Sov. Phys. Dokl. **15**, 475 (1970)].
2. G. A. Mesyats, *Ectons* (Nauka, Yekaterinburg, 1993).
3. A. V. Bushman, S. L. Leshkevich, G. A. Mesyats, *et al.*, Dokl. Akad. Nauk SSSR **312**, 1368 (1990) [Sov. Phys. Dokl. **35**, 561 (1990)].
4. K. Niayesh, J. Phys. D **33**, 2189 (2000).
5. S. A. Barengol'ts, G. A. Mesyats, and D. L. Shmelev, Zh. Éksp. Teor. Fiz. **120**, 1227 (2001) [JETP **93**, 1065 (2001)].
6. G. A. Mesyats and S. A. Barengol'ts, Pis'ma Zh. Éksp. Teor. Fiz. **75**, 306 (2002) [JETP Lett. **75**, 257 (2002)].
7. A. A. Valuev and G. É. Norman, Zh. Éksp. Teor. Fiz. **116**, 2176 (1999) [JETP **89**, 1180 (1999)].
8. V. S. Vorob'ev and S. P. Malyshenko, Phys. Rev. E **56**, 3959 (1997).
9. V. S. Vorob'ev and S. P. Malyshenko, Zh. Éksp. Teor. Fiz. **111**, 2016 (1997) [JETP **84**, 1098 (1997)].

10. V. S. Vorob'ev, A. A. Eronin, and S. P. Malyshenko, Teplofiz. Vys. Temp. **39**, 101 (2001).
11. V. S. Vorob'ev, S. P. Malyshenko, S. I. Tkachenko, and V. E. Fortov, Pis'ma Zh. Éksp. Teor. Fiz. **75**, 445 (2002) [JETP Lett. **75**, 373 (2002)].
12. P. A. Pavlov, *Dynamics of Boiling up of Strongly Superheated Liquids* (Ural. Otd. Akad. Nauk SSSR, Sverdlovsk, 1988).
13. R. T. Knapp, J. W. Daily, and F. G. Hammitt, *Cavitation* (McGraw-Hill, New York, 1970; Mir, Moscow, 1974).
14. A. V. Batrakov, B. J. Jüttner, S. A. Popov, *et al.*, Pis'ma Zh. Éksp. Teor. Fiz. **75**, 84 (2002) [JETP Lett. **75**, 76 (2002)].
15. V. K. Semenchenko, *Surface Phenomena in Metals and Alloys* (GITTL, Moscow, 1957).
16. S. I. Tkachenko, K. V. Khishchenko, V. S. Vorob'ev, *et al.*, Teplofiz. Vys. Temp. **39**, 728 (2001).
17. V. P. Skripov, *Metastable Liquid* (Nauka, Moscow, 1972).
18. *Thermophysical Properties of Liquids in Metastable State: a Handbook*, Ed. by V. P. Skripov, E. N. Sinitsin, P. A. Pavlov, *et al.* (Atomizdat, Moscow, 1980).
19. Yu. M. Kagan, Zh. Fiz. Khim. **34**, 92 (1960).

Translated by V. Sakun

JETP Letters, Vol. 76, No. 7, 2002, pp. 433–435. Translated from Pis'ma v Zhurnal Éksperimental'noĭ i Teoreticheskoĭ Fiziki, Vol. 76, No. 7, 2002, pp. 508–510.

Shock Compression of Solid Deuterium

S. I. Belov, G. V. Boriskov, A. I. Bykov, R. I. Il'kaev, N. B. Luk'yanov, A. Ya. Matveev, O. L. Mikhaĭlova, V. D. Selemir, G. V. Simakov, R. F. Trunin, I. P. Trusov, V. D. Urlin, V. E. Fortov, and A. N. Shuĭkin

Russian Federal Nuclear Center, All-Russia Research Institute of Experimental Physics, Sarov, Nizhni Novgorod region, 607190 Russia

Received June 17, 2002; in final form, September 10, 2002

Experimental data on the compression of solid deuterium at a pressure of ~60 GPa are presented. The data were obtained on a generator of powerful converging spherical shock waves. The results are compared with the data of shock experiments obtained on a Nova laser facility and an electrodynamic EPBF-Z plant. © *2002 MAIK "Nauka/Interperiodica".*

PACS numbers: 62.50.+p; 07.35.+k

The behavior of hydrogen at extremely high pressures and temperatures has always been of interest, both from the fundamental and applied points of view. The fact is that strongly compressed hydrogen plasma is the most abundant state of the matter in nature. It determines the structure of stars and giant planets of the solar system and their evolution, and there is a hope for the implementation of controlled thermonuclear fusion with inertial confinement and preparation of high-temperature metallic hydrogen superconductor by compressing its isotopes to ultrahigh pressures. Despite the very simple one-electron structure, the theoretical predictions about the behavior of hydrogen in the megabar pressure range have a large measure of uncertainty because of the fundamental difficulties associated with correct inclusion of the strong interparticle interaction and taking into account of the degeneracy effects in a strongly nonideal plasma of condensed planes. Interestingly, some theoretical models lose thermodynamic stability in the range of experimentally high temperatures and megabar pressures. This is believed to be due to the "plasma" phase transition and, in turn, stimulates experimental studies in this range of parameters.

Experimental studies of hydrogen at high pressures and temperatures also involve difficulties that are caused by the high mobility and compressibility of hydrogen and its low molecular weight and, hence, hamper the generation of high temperatures by the methods of powerful shock wave physics. For this reason, to move up along the scale of dynamic pressures, one must use the most elaborated methods of exciting powerful shock waves, while the reliability of the presently available results is not too high. For instance, the results obtained for a liquid shock adiabat in the experiments with laser shock waves [1] suggest that the plasma compressibility is exceedingly high and hard to explain by theoretical models, but this was not confirmed experimentally at a later time in the experiments with electrodynamic shock compression [2].

The work on measuring the deuterium shock compressibility using powerful spherically converging shock waves excited by the detonation of condensed explosives began in 1998. Of the possible systems suitable for the solution of this problem, an explosion system was chosen in which a thin-walled steel shell was accelerated to velocities of 9–23 km/s by the spherical converging detonation wave produced by explosion products [3]. The impact of this shell on the deuterium sample produces states in it that are close to the ones obtained on a Nova laser facility [1]. The scheme of the measuring unit is shown in Fig. 1. The standard reflection method was used [4], for which the knowledge of the shock-wave velocity in the substance of interest and

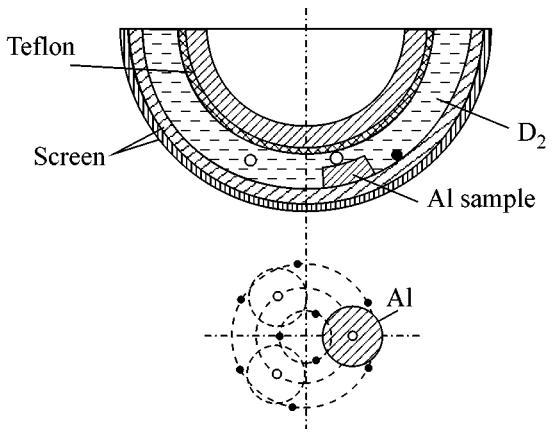

Fig. 1. Scheme of the measuring core and the arrangement of the samples. Positioning of electrocontact gauges is shown at the bottom of the figure: ● and ○ are the lower-level and upper-level gauges, respectively.

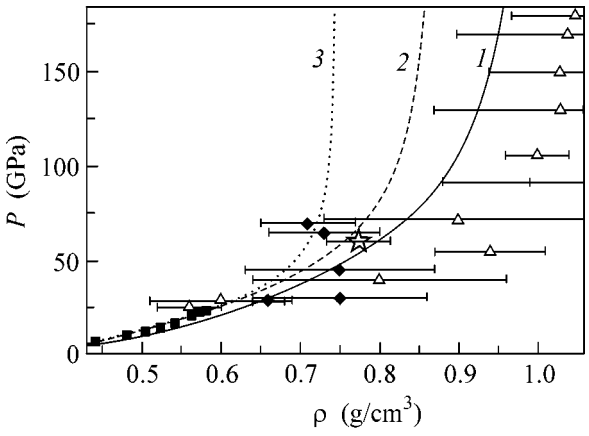

Fig. 2. The *P*–ρ diagram of the deuterium shock compression. Experiment: ☆ this work (solid phase); △, ■, and ◆ are, respectively, the data from [1], [9], and [2] (liquid phase). Calculated Hugoniot curves: for (*1*) solid (ρ_0 = 0.119 g/cm^3) and (*2*) liquid (ρ_0 = 0.171 g/cm^3) D_2, as calculated using the equation of states from [7], and (*3*) liquid D_2 from the Sesam equation of states [2].

the parameters of the wave transmitted in the screen material protecting the sample is necessary to determine the compression parameters of the substance. The range of attainable pressures in a spherical system was determined by the radius of sample positioning; the smaller the radius, the higher the pressure in the sample.

At the first stage of the work, a modest radius (measurement radius) of 17.6 mm was chosen, which corresponded to a velocity of 12.9 km/s for the steel shell. The samples were arranged in a standard way; to detect the time of shock wave transmission through the samples, electrocontact gauges were used. In each measuring device, three samples—a control aluminum (screen material) sample and two deuterium samples—were placed. The gauge length of the samples was 4 mm, which exceeded the target thicknesses in laser experiments by more than an order of magnitude [1]. This eliminates the problem of detecting the nonequlibrium state (in [1], the sample thicknesses were equal to about a hundred microns) and increases the accuracy and reliability of measurements. Nevertheless, considering that the shock wave in the samples is asymmetric in reality (deviates from spherical motion), from four to six experiments with eight to ten independent detections in each of them were carried out to obtain the results with the desired accuracy (~1% for wave velocities).

It should be emphasized that the spherical generators of powerful shock waves used in this work and the method of recording velocities of shock waves and gauging surfaces were put to a detailed test and widely used in Russia in determining the shock compressibility for a broad class of materials in the megabar range of dynamic pressures (see [3] and references given therein).

Although the spherical explosion systems provide a direct and most reliable method of checking the presently existing experimental data, the use of such systems presents considerable difficulties, which cannot be obviated *a priori* with ease. The main difficulties are associated with (1) the necessity of developing the technology of deuterium confinement in the capsule of a measuring device in the "undisturbed" liquid (or solid) state until the shock wave arrives at the sample (>10 min) and (2) the reliable operation of measuring elements at low temperatures (~10–18 K).

In addition, the interpretation of the data for spherical systems is hampered by the necessity of introducing corrections to the experimental results because of the nonstandard convergence of shock wave in the materials under study and the departure of the temperature conditions in the experiments from the standard conditions.

All methodological problems were solved in special studies. However, it was found, in the course of developing the technology of obtaining condensed deuterium from the gas phase, that the transformation of gas into the solid state and holding it in the frozen form for the desired time is a more simple method. Because of this, the first measurements were made with the solid phase in parallel with developing the technology of deuterium confinement in the liquid state. It was assumed that the results of measurements were close for both phases. The aggregate state of deuterium was monitored by calibrated temperature sensors placed at different points of the active volume ($V \sim 10$ cm^2).

The preliminary results were reported at the VI Zababakhin Scientific Readings in Snezhinsk [5]. Note that these results are virtually no different from the data of this work, which includes additional measurements.

After the report in Snezhinsk, new data on measuring the shock compression of liquid deuterium by a group of researchers at the Sandia laboratory (USA) [2] have appeared. In [2], a strong magnetic field accelerating aluminum foil (from 200 to 300 μm in thickness) to a velocity higher than 20 km/s. The impact of the foil on the sample produced shock waves in it with an amplitude up to 70 GPa. These results are presented in Fig. 2. One can see that the data of work [2] are in conflict with the data in [1], although the error of determining the parameters was rather large, as was pointed out by the authors of that work.

In the reflection method, the value of shock adiabat and isentrope or the equation of state for the screen material are the fundamental factors which affect the accuracy of determining pressure and density in the compressed substance. In our experiments, the screen was made from aluminum. The calculations were carried out using the equation of state for the liquid phase [6] of aluminum. This equation adequately describes its thermodynamic parameters and the experimental

Hugoniot curve for Al up to 1000 GPa. In the range below 500 GPa, the calculated Hugoniot curve virtually coincides with the isentrope reported in [2].

According to our equation of state for Al, its density at normal conditions (300 K) is $\rho_0 = 2.71$ g/cm^3, and $\rho_0 = 2.74$ g/cm^3 at $T = 10$ K. The equation of state for solid deuterium [7] gives $\rho_0 = 199$ g/cm^3 at $T = 10$ K.

In five experimental runs conducted in this work, the average local (instantaneous) shock wave velocities (direct measurement), after introducing due corrections, were found to be $D = 16.39 \pm 0.10$ km/s, $U = 8.53$ km/s, and $P = 383$ GPa ($\rho_0 = 2.74$ g/cm^3); for the deuterium, $D = 20.3 \pm 0.2$ km/s, which corresponds to $U = 15.08$ km/s and $P = 60.9$ GPa on the P–U diagram. The shock compression density was $\rho = 0.774 \pm 0.040$ g/cm^3 ($\rho_0 = 0.199$ g/cm^3).

The obtained experimental point is shown in Fig. 2. As an illustration, the Hugoniot curves calculated using the equation of state [7] for solid and the Sesam equation of states [8] for liquid deuterium are presented in the figure. The point lies on the continuation of the experimental adiabat branch obtained in [9] for liquid deuterium and contradicts the data from [1]. However, it should be borne in mind that the measured parameters relate to the solid deuterium and, in principle, may change upon the transition to liquid states. This assumption is based, in particular, on the fact that the experimentally obtained point is situated near the "interface" of two deuterium adiabat branches, so that one cannot rule out the possibility that the deuterium compression parameters change qualitatively at high (megabar) pressures used in this work.

We are planning to accomplish such measurements. It is believed that these experiments, which will be conducted using the forced variants of spherical plants and the sample thicknesses of few millimeters, will play the decisive role in the question of the representativeness of the Livermore laboratory data.

This work was supported in part by the Russian Foundation for Basic Research, project no. 00-02-17505a.

REFERENCES

1. L. B. Da Silva, P. Celliers, G. W. Collins, *et al.*, Phys. Rev. Lett. **78**, 483 (1997).
2. M. D. Knudson, D. L. Hanson, J. E. Bailey, *et al.*, Phys. Rev. Lett. **87**, 225501 (2001).
3. L. V. Al'tshuler, R. F. Trunin, K. K. Krupnikov, and N. V. Panov, Usp. Fiz. Nauk **166**, 575 (1996) [Phys. Usp. **39**, 539 (1996)].
4. L. V. Al'tshuler, K. K. Krupnikov, and M. I. Brazhnik, Zh. Éksp. Teor. Fiz. **34**, 874 (1958) [Sov. Phys. JETP **7**, 606 (1958)].
5. S. I. Belov, G. V. Boriskov, A. I. Bykov, *et al.*, in *Proceedings of VI Zababakhin Scientific Readings, Snezhinsk, Russia, 2001*.
6. V. D. Urlin, in *Shock Waves and Extremal States of Matter*, Ed. by V. E. Fortov *et al.* (2000), p. 255.
7. V. P. Kopyshev and V. D. Urlin, in *Shock Waves and Extremal States of Matter*, Ed. by V. E. Fortov *et al.* (Moscow, 2000), p. 297.
8. G. I. Kerley, *Molecular Based Study of Fluids*, Ed. by J. M. Haile and G. A. Mansoori (American Chemical Society, Washington, 1983), p. 107.
9. N. C. Holms, M. Ross, and W. J. Nellis, Phys. Rev. B **52**, 15835 (1995).

Translated by V. Sakun

JETP Letters, Vol. 76, No. 7, 2002, pp. 436–439. Translated from Pis'ma v Zhurnal Éksperimental'noĭ i Teoreticheskoĭ Fiziki, Vol. 76, No. 7, 2002, pp. 511–514.

Isotherms of Isoelectronic Materials, Melting, and Shear Moduli in the Megabar Pressure Range

V. V. Kechin

Institute for High Pressure Physics, Russian Academy of Sciences, Troitsk, Moscow region, 142190 Russia
e-mail: kechin@hppi.troitsk.ru

Received August 8, 2002; in final form, September 10, 2002

It is shown that the isotherms of isoelectronic materials in the statistical model converge in the megabar pressure range. The convergence of isotherms is universal and depends neither on the crystallographic structure nor on the specific type of the intermolecular potential. It is pointed out that the majority of compounds and minerals which constitute the Earth's mantle are isoelectronic with neon. The melting curves of isoelectronic materials are parallel to each other. The mutual arrangement of the melting curves depends on the number of atoms in the molecule. Computations of the shear moduli of materials at 1 Mbar show that the materials with small number of electrons per atom have the lowest shear modulus. These materials are preferable for using as pressure-transmitting media in the megabar pressure range. *© 2002 MAIK "Nauka/Interperiodica".*

PACS numbers: 64.30.+t; 64.70.Dv; 62.20.Dc

1. The materials are isoelectronic if they have the same number Z of electrons (protons) per atom. There is confusion about the definition what materials are isoelectronic. For example, the CH_4, NH_3, and H_2O compounds are considered as isoelectronic [1]. Nevertheless, although all of them have 10 electrons per molecule, they have 2.0, 2.5, and 3.3 electrons per atom, respectively; i.e., they are not isoelectronic. In accordance with the classical rigid-ion model, the isotherms of isoelectronic rare gas solids and alkali halides are separated by the interval $\Delta P \sim V^{-4/3}$, where P is pressure, and V is volume. Hence, the interval P must increase at compression. However, the results of X-ray experiments showed the opposite behavior.

X-ray diffraction experiments [2, 3] at 300 K for isoelectronic CsI and Xe (Z = 54), as well as for RbBr and Kr (Z = 36) [3] up to 0.55 Mbar (1 Mbar = 100 GPa) are illustrated in Fig. 1. Figure 1 shows that the isotherms of these isoelectronic pars at the pressure $P > 0.2$ Mbar are indistinguishable within the experimental resolution. The convergence of isotherms for CsI and Xe was studied up to 3 Mbar, where both materials undergo structural changes and insulator–metal transitions [4]. Recently, Loubeyre *et al.* measured the equation of state for isoelectronic solids (Z = 2) LiH up to 0.36 Mbar, LiD up to 0.94 Mbar, and He up to 1.3 Mbar by X-ray diffraction methods [5, 6]. They found that the isotherms of LiH and He approached each other under pressure [5]. The authors of [5, 6] noted that the similarity in the equations of state of isoelectronic solids under pressure may be quite general and this can hardly be predicted *a priori* [6].

The convergence of isoelectronic isotherms of inert gas solids and alkali halides (group IA–VII compounds) at high pressure can be explained from simple considerations. Both materials have closed shells, and, hence, the short-range repulsive interactions between inert gases and alkali halides are virtually identical. The main difference between them consists in the attractive forces: Coulomb forces in halides and van der Waals forces in inert gases. With increasing pressure, the

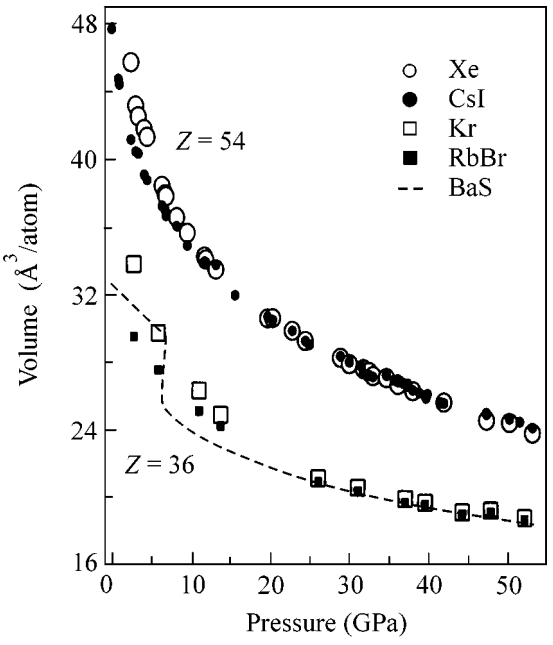

Fig. 1. 300-K Isotherms of isoelectronic materials Xe, CsI (Z = 54) and Kr, RbBr, BaS (Z = 36) from X-ray experiments [2, 3, 8].

interatomic forces start to be dominated by short-range repulsive rather than attractive terms, and the isotherms of these materials must approach each other under pressure.

In connection with the experimental study of the equations of state of solid inert gases and IA-VII compounds, two question arise:

(1) is the convergence of isotherms at high pressure complete or are the isotherms still separated by the interval ΔV?

(2) does the convergence of isotherms at high pressure hold only for inert gases and alkali halides or is it also valid for all isoelectronic materials?

The equations of state of elements at megabar pressures include the kinetic pressure of a uniform degenerate Fermi gas, the Coulomb (Madelung) correction, and the exchange correction. It has the form [7]

$$p = n^{5/3}(1 - bZ^{2/3}n^{-1/3} - cn^{-1/3}), \qquad (1)$$

where $p = P/a$ is the reduced pressure, P is the pressure in Mbar,

$$a = \frac{(3\pi^2)^{2/3}e^2}{5a_B^4} = 563.173 \text{ Mbar};$$

$$b = \frac{4^{1/3}}{2\pi}0.252643; \quad c = \frac{5}{4\pi(3\pi^2)^{1/3}} = 0.128613,$$

$n = Za_B^3/V$ is the electron density, V is the atomic volume, a_B is the Bohr radius, and e is the electron charge.

The equation of state of compounds can by obtained from the condition that the volumes of different components of compounds are additive and their partial pressures are equal. It is convenient to write the generalized equation of state in the form suitable for both elements and compounds,

$$V = a_B^3 Z\left\{p^{3/5} + \frac{3}{5}[b(Z^*)^{2/3} + c]p^{2/5}\right\}^{-1}, \qquad (2)$$

where

$$(Z^*)^{2/3} = \frac{\sum N_k Z_k^{5/3}}{\sum N_k Z_k}, \quad k > 1. \qquad (3)$$

Here, N_k is the number of times the element with the atomic number Z_k appears in the chemical formula. The parameter Z^* corrects the Coulomb (Modelung) correction for compounds (for an element, $Z^* = Z$). It follows from Eq. (2) that the isotherms of two materials A and B having the same Z (isoelectronic materials) but different Z_A^* and Z_B^* ($Z_B^* > Z_A^*$) are separated by the interval

$$-\Delta V/V_A \approx 0.54[(Z_B^*)^{2/3} - (Z_A^*)^{2/3}]P^{-1/5}. \qquad (4)$$

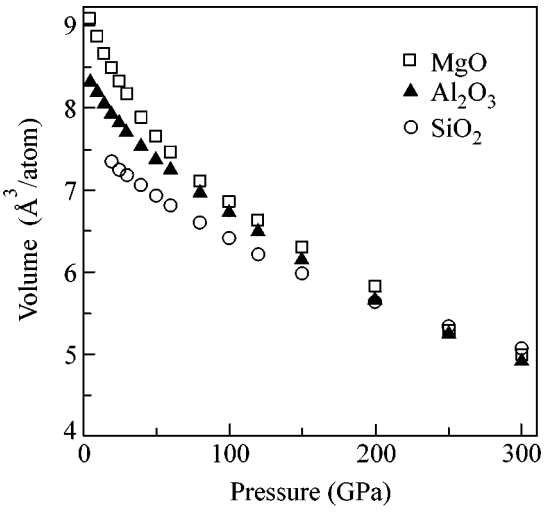

Fig. 2. 300-K Isotherms of isoelectronic materials MgO, Al_2O_3, and SiO_2 ($Z = 10$) from shock-wave experiments [9].

It can be concluded that

(1) at moderate pressures the isotherms of isoelectronic materials are separated by the interval $\Delta V(P)$. The mutual arrangement of the isotherms of isoelectronic materials depends on Z^*. For compounds, Z^* is larger then for elements, $Z^* > Z$, and, hence, the isotherm of, e.g., CsI is located below the isotherm of Xe (Fig. 1);

(2) at megabar pressures, the isotherms of isoelectronic materials converge completely ($\Delta V \longrightarrow 0$ at $P \longrightarrow \infty$). The convergence of the isotherms of isoelectronic material at high pressure is universal. It is true for the different classes of materials (molecular, ionic, covalent, or metallic) and depends neither on the crystallographic structure nor on the specific type of the intermolecular potential at low pressure.

The isotherm of BaS (Z = 36; II–VI compound) from X-ray diffraction experiments [8] is shown in Fig. 1. It is seen that, after the B1–B2 phase transition at 6.5 GPa, the isotherm of BaS above $P > 20$ GPa coincides with the isotherms of RbBr and Kr. The isotherms of isoelectronic oxides MgO, Al_2O_3, and SiO_2 (Z = 10; II–VI, III–VI, and IV–VI binary compounds, respectively) from shock-wave experiments [9] are presented in Fig. 2. (The Hugoniot curve of SiO_2 above 2 Mbar corresponds to melting [10]). Figure 1 shows that, after the transition to the high-density phase (stishovite) at $P > 0.2$ Mbar, the isotherm of SiO_2 coincides with the isotherms of MgO and Al_2O_3.

It is remarkable that the majority of compounds and minerals constituting the Earth's mantle [11] are isoelectronic with neon (Z = 10). Some of these materials are MgO, Al_2O_3, SiO_2, LiCl, NaF, Na_2O, P_2O_5, MgF_2, $MgSiO_3$, Mg_2SiO_4, $CaMg(SiO_3)_2$, $NaAl(SiO_3)_2$, $Al_2Si_2O_8$, $Ca_2Mg_5(Si_2O_5)_4(OH)_2$, $NaAlSi_3O_8$, $MgAl_2O_4$, $Mg_3Al_2(Si_2O_6)_3$, and $Mg_3Al_2Si_3O_{12}$. There-

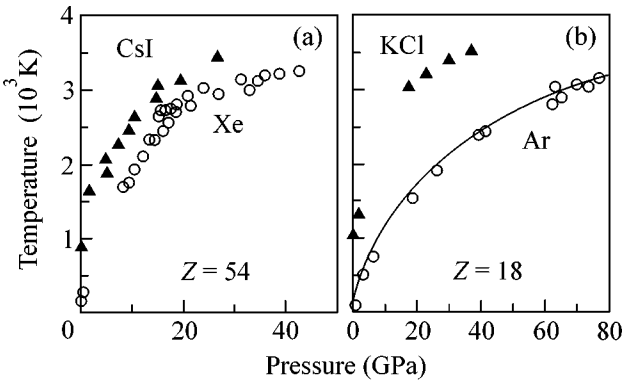

Fig. 3. Melting curves of (a) Xe and CsI and (b) Ar and KCl from DAC experiments [14, 15]. The line for Ar corresponds to the equation $T_m = 83.78(1 + \Delta P/0.2232)^{0.6854}\exp(-0.005\Delta P)$, $P = P - 0.7$ GPa (see [16]).

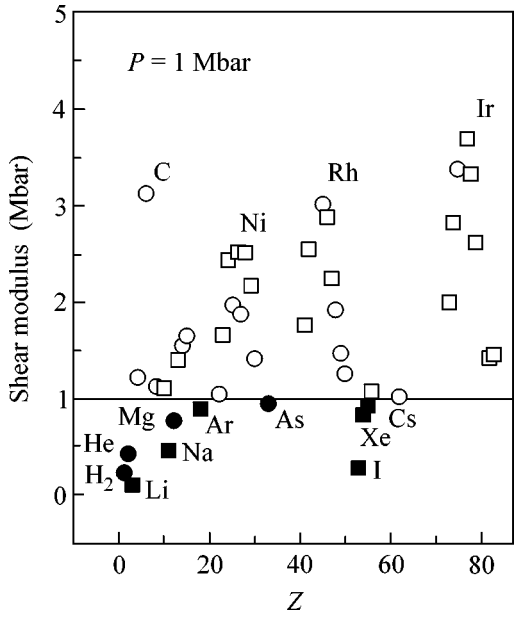

Fig. 4. The shear moduli of various materials at a pressure of 1 Mbar, as calculated from the Voigt formula $G_V = (3B - 6P)/5$. The squares correspond to the bcc and fcc lattices.

fore, the Earth's mantle, provided that its composition is described by the parameter Z, mainly consists of neon. If one bears in mind that the Earth's core mainly consists of iron (Z = 26), then one can say that the Earth is mainly a "neon–iron" body.

To conclude this section, it should be emphasized that Eq. (1) holds at high compressions ($V < 4a_B^3 Z^{1/3}$). Nevertheless, experiments show that the convergence of isoelectronic materials may occur at much lesser compressions.

2. Let as turn now to the melting temperature of isoelectronic materials. It was predicted earlier that the melting curves of the isoelectronic materials Xe and CsI intersect at high pressure [12]. The pressure dependence of melting temperature can be estimated qualitatively from the Lindemann melting theory. It follows from this theory that the melting temperature $T_m \sim nVB$, where n is the number of atoms in compound, V is the atomic volume, and B is the bulk modulus [13]. Therefore, the curves of isoelectronic materials should be parallel to each other. The mutual arrangement of melting curves mainly depends on the number of atoms in compounds. Thus, the melting temperature of a compound is higher than the melting curve of the corresponding isoelectronic element. The melting curves of the isoelectronic pairs Xe–CsI (Z = 54) and Ar–KCl (Z = 18) at high pressures, taken from the unique DAC experiments, are presented in Fig. 3 [14–16]. Figure 3 shows that the melting curves of isoelectronic materials do not intersect.

3. A new effect—the inversion of shear moduli upon compression for various classes of materials—was predicted in [17]. In accordance with this hypothesis, the materials traditionally considered as the softest (such as rare gas solids and molecular materials) can become the hardest in the megabar range. In this regard, it should be noted that the convergence of the isotherms of pairs of isoelectronic materials such as CsI–Xe, RbBr–Kr and LiH–He [2, 3, 5] (Fig. 1) implies that the inversion of shear moduli for rare gas solids Xe, Kr, and He does not occur (the isotherms of isoelectronic pairs do not intersect upon compression). As an example of the shear moduli inversion, it is pointed out in [17] that Xe becomes stiffer than CsCl at pressures of hundreds of kilobars. This is not surprising, because Xe is stiffer than Kr, which is isoelectronic with respect to CsCl. It is pointed out in [17] that the intersection of melting curves (for example, Fe and Ar) is a strong evidence of the shear modulus inversion. However, the melting temperature is not connected directly to the shear moduli. Thus, the shear modulus of Pd is half of that of Fe, but the melting temperature of Pd is higher than for Fe [18]; the isotherms and shear moduli of the isoelectronic pairs Xe–CsI and Ar–KCl converge at high pressure, but their melting temperatures are different (Fig. 3).

The authors of [17] recommended to use metals, including In, Pb, Sn, Na, Be, Bi, Ga, etc., as quasi-hydrostatic pressure-transmitting media in the megabar pressure range, instead of the traditional materials (rare gas solids etc.). We calculated the shear modulus at a pressure of 1 Mbar for various Z using the Voight formula $G_V = (3B–6P)/5$ (Fig. 4). This formula is exact for the lattices with the central interaction [17], e.g., for the bcc and fcc structures, i.e., the most probable structures at high pressure. In the calculations of shear moduli, we used the equation of state of materials from the X-ray and shock-wave data. Figure 4 shows that the inert gases and molecular gases, as well as alkali metals (and, consequently, corresponding isoelectronic compounds) have the lowest shear moduli and that the

inversion of shear moduli at 1 Mbar is absent. It should be noted that, when studying the melting curves at pressures up to 1 Mbar and temperatures up to 4000 K, isoelectronic Ar and KCl ($Z = 18$), as well as MgO and Al_2O_3, which are isoelectronic with Ne ($Z = 10$) [19], were used. Figure 4 shows that the materials with low Z value ($Z < 4$), for example, H_2 ($Z = 1$), He, LiH ($Z = 2$), NH_3 ($Z = 2.5$), and H_2O ($Z = 3.3$) are most suitable for using as pressure-transmitting media in the megabar pressure range. A methanol–ethanol–water mixture is often used in high-pressure experiments as a pressure-transmitting medium. It is remarkable that $Z \cong 3$, for this mixture, for which reason this mixture is used successfully as a pressure-transmitting medium.

The author is grateful to S.M. Stishov, E.E. Tareeva, and V.N. Ryzhov for fruitful discussion. This work was supported in part by the Russian Foundation for Basic Research, project no. 02-02- 17112.

REFERENCES

1. J. W. Otto, R. F. Porter, and A. L. Ruoff, J. Phys. Chem. Solids **30**, 171 (1989).
2. A. N. Zisman, I. V. Aleksandrov, and S. M. Stishov, Phys. Rev. B **32**, 484 (1985).
3. I. V. Aleksandrov, A. N. Zisman, and S. M. Stishov, Zh. Éksp. Teor. Fiz. **92**, 657 (1987) [Sov. Phys. JETP **65**, 371 (1987)].
4. H. K. Mao, Y. Wu, R. J. Hemley, *et al.*, Science **246**, 649 (1989).
5. P. Loubeyre, R. Le Toullec, M. Hanfland, *et al.*, Phys. Rev. B **57**, 10403 (1998).
6. P. Loubeyre, R. Le Toullec, J. P. Pinceaux, *et al.*, Phys. Rev. Lett. **71**, 2272 (1993).
7. D. A. Kirzhnits, Zh. Éksp. Teor. Fiz. **32**, 115 (1957) [Sov. Phys. JETP **5**, 64 (1957)]; Zh. Éksp. Teor. Fiz. **35**, 1545 (1958) [Sov. Phys. JETP **8**, 1081 (1959)]; D. A. Kirzhnits, Yu. U. Lozovik, and G. V. Shpatkovskaya, Usp. Fiz. Nauk **117**, 3 (1975) [Sov. Phys. Usp. **18**, 649 (1975)]; N. N. Kalitkin and I. A. Govorukhina, Fiz. Tverd. Tela (Leningrad) **7**, 355 (1965) [Sov. Phys. Solid State **7**, 287 (1965)]; R. M. More, Phys. Rev. A **19**, 1234 (1979).
8. S. T. Weir, Y. K. Vohra, and A. L. Ruoff, Phys. Rev. B **33**, 4221 (1986).
9. R. T. Reynolds and A. L. Summers, J. Geophys. Res. **74**, 2494 (1969).
10. E. K. Graham, Geophys. J. R. Astron. Soc. **32**, 15 (1973).
11. A. E. Ringwood, *Composition and Petrology of the Earth's Mantle* (McGraw-Hill, New York, 1975).
12. R. Boehler, M. Ross, and D. B. Boercker, Phys. Rev. B **53**, 556 (1996).
13. V. N. Zharkov and V. A. Kalinin, *Equations of State for Solids at High Pressures and Temperatures* (Nauka, Moscow, 1968; Consultants Bureau, New York, 1971).
14. R. Boehler, M. Ross, P. Söderlind, *et al.*, Phys. Rev. Lett. **86**, 5731 (2001).
15. R. Boehler, M. Ross, and D. B. Boercker, Phys. Rev. Lett. **78**, 4589 (1997).
16. V. V. Kechin, Phys. Rev. B **65**, 052102 (2002).
17. V. V. Brazhkin and A. G. Lyapin, Pis'ma Zh. Éksp. Teor. Fiz. **73**, 220 (2001) [JETP Lett. **73**, 197 (2001)].
18. M. W. Guinan and D. J. Steinberg, J. Phys. Chem. Solids **35**, 1501 (1974).
19. D. Errandonea, R. Boehler, and M. Ross, Phys. Rev. Lett. **85**, 3444 (2000); D. Errandonea, B. Schwager, R. Ditz, *et al.*, Phys. Rev. B **63**, 132104 (2001); D. Errandonea, R. Boehler, and M. Ross, Phys. Rev. B **65**, 012108 (2002).

Translated by V. Kechin

JETP Letters, Vol. 76, No. 7, 2002, pp. 440–443. Translated from Pis'ma v Zhurnal Éksperimental'noĭ i Teoreticheskoĭ Fiziki, Vol. 76, No. 7, 2002, pp. 515–519.

Interactions of $_{\mu}$Al Acceptor Impurity in Weakly and Heavily Doped Silicon

T. N. Mamedov[1], D. G. Andrianov[2], D. Herlach[3], V. N. Gorelkin[4], A. V. Stoĭkov[1], and U. Zimmermann[3]

[1] *Joint Institute for Nuclear Research, Dubna, Moscow region, 141980 Russia*
e-mail: tmamedov@nu.jinr.ru
[2] *State Research and Design Institute of Rare Metals "Giredmet", Moscow, 109017 Russia*
[3] *Paul Scherrer Institut, CH-5232 Villigen PSI, Switzerland*
[4] *Moscow Institute of Physics and Technology, Dolgoprudnyĭ, Moscow region, 141700 Russia*
Received July 25, 2002; in final form, August 26, 2002

The interactions of the aluminum acceptor impurity in silicon are investigated using polarized negative muons. The polarization of negative muons is studied as a function of temperature on crystalline silicon samples with phosphorus (1.6×10^{13} cm^{-3}) and boron (4.1×10^{18} cm^{-3}) impurities. The measurements are performed in a magnetic field of 4.1 kG perpendicular to the muon spin, in the temperature range from 4 to 300 K. The experimental results show that, in phosphorus-doped *n*-type silicon, an $_{\mu}$Al acceptor center is ionized in the temperature range $T > 50$ K. For boron-doped silicon, the temperature dependence of the shift of the muon spin precession frequency is found to deviate from the $1/T$ Curie law in the temperature range $T \lesssim 50$ K. The interactions of a $_{\mu}$Al acceptor that may be responsible for the effects observed in the experiment are analyzed. © *2002 MAIK "Nauka/Interperiodica".*

PACS numbers: 71.55.Cn; 76.75.+i

In the last few years, interest in studying paramagnetic centers in semiconductors has quickened in connection with the possibility of using them as a basis for designing a quantum computer [1], this issue being the subject of a considerable literature. In the light of this problem, detailed data on the electronic structure of different paramagnetic centers and on their interactions in semiconductors are of prime importance. One of the types of paramagnetic centers existing in semiconductors is a shallow acceptor center (AC). Unlike donors, shallow acceptor centers formed in diamond-like semiconductors (such as diamond, silicon, and germanium) have not been adequately investigated [2].

Our previous studies [3–6] showed that, by using polarized negative muon beams, it is possible to obtain extensive data on the interactions of ACs in diamond-like semiconductors, while the potentialities of conventional methods (ESR, ENDOR, and NMR) in this respect are limited.

The possibility to use negative muons for studying ACs in semiconductors is based on the fact that a muon being captured by an atom of the medium causes the formation of a muon atom, which models an acceptor impurity. For example, in silicon, a muon atom is an analogue of an aluminum atom: $_{\mu}$Al. The time dependence of the muon polarization $P(t)$ on the 1*s* level of a $_{\mu}$Al atom is determined by the state of the electron shell of the given muon atom (AC) and by its interaction with the medium. An AC in a semiconductor can be in the ionized (diamagnetic) state or in the neutral (paramagnetic) state. Let us assume that $_{\mu}$Al is formed in the neutral state $_{\mu}$Al^0 and that the transition to the diamagnetic state $_{\mu}$Al$^-$ is allowed. Then, the muon polarization $P(t)$ in an external magnetic field transverse with respect to the muon spin can be represented in the form [4]

$$P(t) = P_0[C_1 e^{-(\lambda + \nu_i)t}\cos(\omega t + \phi) + C_2\cos(\omega_d t + \phi_d)], \quad (1)$$

where P_0 is the muon polarization on the 1*s* level at $t = 0$; λ is the relaxation rate of the muon spin in the paramagnetic state of the AC; ν_i is the ionization rate of the AC; ω and ϕ are the precession frequency and initial phase for the relaxing polarization component; ω_d and ϕ_d are the respective parameters for the nonrelaxing (diamagnetic) polarization component; and C_1 and C_2 are the relative amplitudes of the relaxing and nonrelaxing components, which depend on λ, ν_i, and $\delta = \omega - \omega_d$.

The experimentally measured quantities λ and ω depend on such parameters of the AC as the relaxation rate of its magnetic moment (ν) and the hyperfine interaction constant (A). The value of the latter is determined by the density distribution of the wave function of a hole bound to the acceptor. In [7], the isotropic hyperfine interaction approximation was used to derive analytical relationships between the parameters of the

muon spin polarization and the parameters characterizing the interactions of the ACs in a semiconductor:

$$\frac{\omega - \omega_d}{\omega_d} = -\frac{g\mu_B}{2\mu_B^{\mu}}\frac{J(J+1)A}{3k_BT}, \quad (2)$$

$$\lambda = \frac{J(J+1)}{3}\left(\frac{(A/\hbar)^2}{\nu} + \frac{(A/\hbar)^2\nu}{\nu^2 + \omega_e^2}\right). \quad (3)$$

Here, $\hbar = h/2\pi$, where h is Planck's constant; k_B is Boltzmann's constant; μ_B and μ_B^{μ} are the Bohr magnetons for an electron and a muon, respectively; g is the g factor for an AC; $\omega_e = g\mu_B B/\hbar$ is the angular frequency of precession for the magnetic moment of the electron shell of an AC in a magnetic field **B**; and T is the temperature. For a shallow AC in silicon, $J = 3/2$ [8] and $g = -1.07$ [9].

Our previous studies [3, 6] gave some evidence that the temperature dependence of the shift of the muon spin precession frequency deviates from the $1/T$ Curie law for $_{\mu}$Al acceptors in phosphorus-doped silicon (Si:P, [P] = 1.6×10^{13} cm^{-3}) and in boron-doped silicon (Si:B, [B] = 4.1×10^{18} cm^{-3}). In the latter case, the impurity concentration is close to its critical value n_c corresponding to the semiconductor-to-metal transition (the Mott transition).

This paper presents a more detailed study of the interactions of ACs in silicon samples of the aforementioned types.

The polarization of muons stopped in the target was measured in a magnetic field perpendicular to the muon spin by detecting the decay electrons resulting from the reaction $\mu^- \longrightarrow e^- + \bar{\nu}_e + \nu_{\mu}$. In this case, the time dependence of the number of detected electrons has the form of a cosine-modulated exponent. The cosine period is equal to the period of revolution (precession) of the muon spin in magnetic field, and the cosine amplitude and its time dependence are determined by the muon polarization at the instant of decay.

The measurements were performed using a GPD spectrometer [10] positioned in the μE1 muon channel of the proton accelerator of the Paul Scherrer Institute (Switzerland). The samples cut out of silicon single crystals had the form of disks ~20 mm in diameter and ~8 mm in height. The samples were mounted so that the disk axis coincided with the axis of the muon beam. The temperature of the samples was stabilized with an accuracy of 0.1 K in the temperature range from 4 to 300 K. The procedure used for processing the experimental spectra is described in [4, 5].

The results obtained by approximating the experimental data by function (1) testify to the absence of the nonrelaxing polarization component for the boron-doped sample in the whole temperature range (i.e., $C_2 = 0$ and $\nu_i = 0$). In the phosphorus-doped silicon, only the relaxing component is observed in the temperature interval 12.5 K ≤ T ≤ 50 K, while at T > 52 K, only the nonrelaxing component of the muon polarization is present in the spectrum (i.e., $C_1 = 0$). Hence, in Si:B, an AC is in the paramagnetic (neutral) state in the whole temperature range. In Si:P, an AC is paramagnetic at temperatures $T \lesssim 50$ K and diamagnetic when $T >$ 52 K.

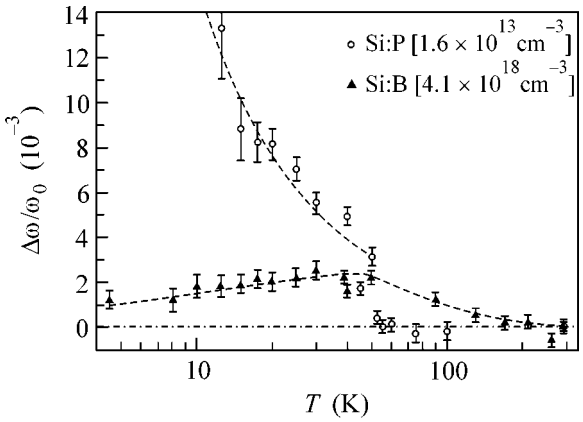

Fig. 1. Temperature dependences of the shift of the muon spin precession frequency for silicon samples with boron and phosphorus impurities. The dashed lines are plotted for illustration.

For the samples under investigation, Fig. 1 shows the temperature dependences of the shift of the muon spin precession frequency $\Delta\omega = (\omega - \omega_0)$, where ω_0 is the precession frequency measured for each given sample at $T_0 = 290$ K. For the Si:P sample at $T < 50$ K and for the Si:B sample at $T > 50$ K, the dashed lines in Fig. 1 represent the dependences of the types of $1/T$ and $(1/T - 1/T_0)$, respectively. As seen from this figure, the dependence $\Delta\omega/\omega_0 = f(T)$ is determined by the $1/T$ Curie law in the temperature range $T < 50$ K for Si:P and in the temperature range $T > 50$ K for Si:B. In the latter case, the experimental data are closer approximated by the dependence $\Delta\omega/\omega_0 \sim (1/T - 1/T_0)$. This suggests that, in Si:B, at room temperature, an AC is not ionized ($\omega_0 \neq \omega_d$). Approximating the experimental data in the aforementioned temperature ranges by dependence (2), we determined the value of the hyperfine interaction constant (A/h) for a $_{\mu}$Al acceptor. This value was found to be (23 ± 2) MHz for Si:P and (20.0 ± 2.3) MHz for Si:B, which agrees with our previous results [6] to within the experimental errors.

However, in the case of boron-doped silicon, in the temperature range 4.5 K ≤ $T \lesssim 40$ K, the dependence $\Delta\omega/\omega_0 = f(T)$ noticeably deviates from the $1/T$ law: at $T \approx 50$ K, the growth of the frequency shift with decreasing temperature terminates and, at $T < 50$ K, even a certain decrease in $\Delta\omega/\omega_0$ is observed as T decreases further. The temperature dependence of the muon spin relaxation rate obtained for this sample also considerably differs from the corresponding depen-

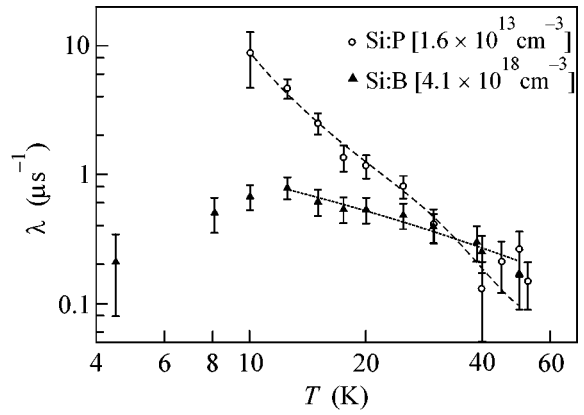

Fig. 2. Temperature dependences of the muon spin relaxation rate for silicon samples with phosphorus and boron impurities. The dashed and dotted lines show the results of approximation by dependence (3).

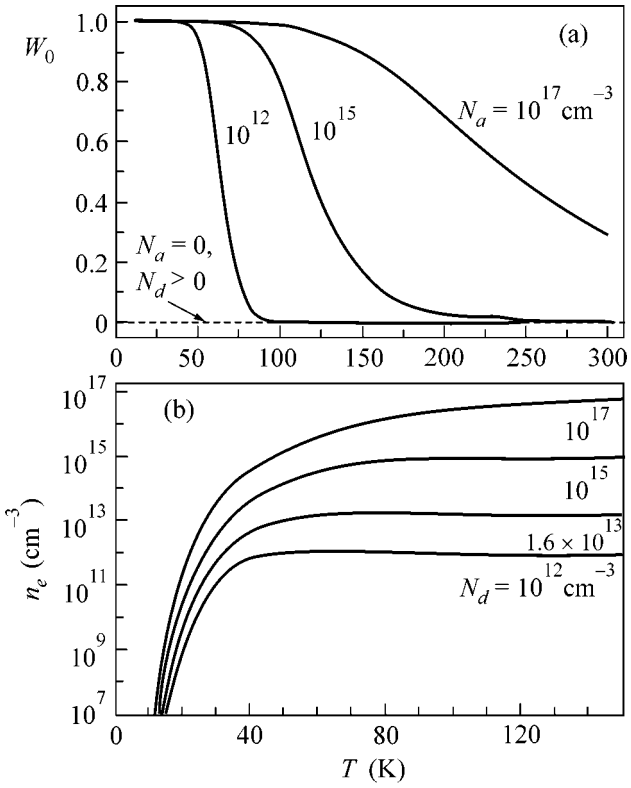

Fig. 3. (a) Probability W_0 for a $_\mu$Al acceptor center to be in the nonionized (paramagnetic) state at the thermodynamic equilibrium in silicon with different concentrations of donor N_d and acceptor N_a impurities. (b) Temperature dependence of the free electron concentration n_e in silicon with different donor (phosphorus) concentrations N_d. The values of W_0 and n_e are calculated by the relations known from the literature (see, e.g., [12]).

dence for phosphorus-doped silicon (Fig. 2). In the latter case, the experimental dependence $\lambda(T)$ agrees well with that reported previously [6] for silicon samples with impurity concentrations lower than $\sim 2 \times 10^{17}$ cm^{-3}.

The data presented in Fig. 2 were approximated by dependence (3) under the assumption that the relaxation rate of the magnetic moment of an acceptor depends on temperature according to the power law $\nu = CT^q$: (a) for Si:P, at A/h = 23 MHz; (b) for Si:B, at A/h = 20 MHz and $T > 12$ K. The values of the parameters C and q obtained as a result of this approximation were $C = (1.9 \pm 1.2) \times 10^6$ s^{-1} and $q = 3.2 \pm 0.3$ for Si:P and $C = (2.4 \pm 0.7) \times 10^9$ s^{-1} and $q = 1.1 \pm 0.1$ for Si:B. It should be noted that, in the case of Si:B, the absolute value of the parameter C can be inaccurate, because the approximation of experimental data was performed using the value of A/h derived from the data on $\Delta\omega/\omega_0$ at $T \geq 50$ K.

The fact that the exponent in the temperature dependence of ν is close to three testifies to the phonon mechanism of relaxation for the magnetic moment of an AC in phosphorus-doped silicon, whereas, in heavily boron-doped silicon, the dominant relaxation mechanism is the spin-exchange scattering of holes by the acceptor (see also [6]).

From the data obtained for $\Delta\omega/\omega_0$, it follows that, in phosphorus-doped silicon, at $T > 50$ K, ionization of ACs takes place. In *n*-type silicon, the paramagnetic state of an AC, i.e., $_\mu$Al^0, in which a given center is formed within the time $t < 10^{-8}$ s [11], is not a thermodynamic equilibrium state (see Fig. 3a, which presents the calculated probability W_0 for the $_\mu$Al acceptor center to be in the nonionized state at thermodynamic equilibrium in *n*-type and *p*-type silicon). In principle, the ionization of an acceptor in *n*-type silicon can be caused by the following processes: (i) the capture of an electron from the conduction band and (ii) the thermal ionization, which occurs when a hole (h^+) acquires energy due to its interaction with phonons and thus leaves the impurity center. According to theoretical calculations [13], the rate of the thermal ionization of impurity centers grows with increasing temperature as $\nu_i \sim \exp(-E_i/k_BT)$, where E_i is the impurity ionization energy. Since the rate of capture of the conduction electrons by the ACs is proportional to the electron concentration n_e [14], we have $\nu_i \sim n_e \sim \exp(-E_i/2k_BT)$ (the calculated dependence $n_e = f(T)$ for phosphorus-doped silicon is shown in Fig. 3b). However, the absence of reliable data on the capture cross section for conduction electrons captured by a neutral AC (see [14]) and the absence of data on the AC–phonon interaction constant makes it impossible to estimate the contribution of the aforementioned processes to the dependences $\Delta\omega/\omega_0 = f(T)$ observed in the experiment. Presumably, one should not rule out the possibility that, in *n*-type silicon, a $_\mu$Al atom can be formed in the ionized state in the case when the free electron concentration in the sample exceeds the concentration of holes that appear near the muon atom in the course of its formation.

The study of the temperature T_i at which a break is observed in the curves $\Delta\omega/\omega_0 = f(T)$ as a function of

donor concentration in silicon reveals the role of the thermal ionization process. At a fixed temperature, the rate of thermal ionization of ACs should remain practically invariable in a wide range of impurity concentrations, whereas the contributions of the two other mechanisms of the AC ionization are concentration dependent.

In Si with a boron impurity concentration of 4.1×10^{18} cm^{-3}, the breaks observed in the dependences $\Delta\omega/\omega_0 = f(T)$ and $\lambda = f(T)$ can be caused by the interaction of the $_{\mu}$Al acceptor with boron impurity centers. This interaction is likely to become effective only in the temperature range $T \lesssim 50$ K.

The problem of interimpurity interactions in disordered systems has been intensively studied in the last few years (see [15]). Silicon, in which the semiconductor-to-metal transition (the Mott transition) occurs as a result of the interaction between impurity centers randomly distributed in space, is one of the most suitable objects for studying this phenomenon.

As is known [16, 17], in heavily doped *p*-type or *n*-type silicon, the exchange interaction between impurities leads to a decrease in the macroscopic magnetic susceptibility χ of the sample: $\chi \sim T^{-\alpha}$, where the exponent α is less than unity and decreases with increasing impurity concentration; i.e., the temperature dependence of χ noticeably deviates from the Curie law. According to [16], in boron-doped silicon, $\alpha = (0.3–0.4)$ at the boron concentration [B] $\approx 4 \times 10^{18}$ cm^{-3}. Basically, from Eq. (2), one should infer that $\Delta\omega/\omega_0 \sim \chi$. It is evident that the temperature dependence of the shift of the muon spin precession frequency that was obtained in our experiments for Si:B at $T \lesssim 50$ K (see Fig. 1) cannot be fully explained in terms of the macroscopic magnetic susceptibility of the given sample, because, even at $\alpha = 0.3$, a twofold increase in $\Delta\omega/\omega_0$ should be observed as the temperature decreases from 50 to 5 K. However, unlike the macroscopic quantity χ, the frequency shift $\Delta\omega/\omega_0$ is determined by the local susceptibility of the AC. Hence, the difference in the behavior of $\Delta\omega/\omega_0$ and χ should be a manifestation of the difference between the local and macroscopic magnetic susceptibilities in disordered systems near the Mott transition.

Thus, it was found that the behavior of a $_{\mu}$Al acceptor center in Si strongly depends on the type and concentration of impurity in the sample: in weakly doped *n*-type silicon, the AC is ionized at $T > 50$ K, while in the sample with a high concentration of *p*-type impurity ([B] $= 4.1 \times 10^{18}$ cm^{-3}), the AC is in the paramagnetic (neutral) state practically up to room temperature. In the temperature range $T \lesssim 50$ K, in *p*-type silicon, a decrease in the atomic susceptibility of the AC is observed, which testifies to the appearance of a magnetic interaction between impurities. In addition, the results of this study presumably testify to the difference between the local susceptibility of an AC and the macroscopic magnetic susceptibility of the sample. Further studies should reveal the mechanism of ionization of an AC in *n*-type silicon and provide a more detailed information about the interimpurity interactions in *p*-type silicon.

We are grateful to the Management of the Paul Scherrer Institute (Switzerland) for making these measurements possible.

The work was supported by the Russian Foundation for Basic Research, project no. 02-02-16881.

REFERENCES

1. S. Ya. Kilin, Usp. Fiz. Nauk **169**, 507 (1999).
2. G. D. Watkins, Fiz. Tverd. Tela (St. Petersburg) **41**, 826 (1999) [Phys. Solid State **41**, 746 (1999)].
3. V. N. Gorelkin, V. G. Grebinnik, K. I. Gritsaĭ, *et al.*, Pis'ma Zh. Éksp. Teor. Fiz. **63**, 539 (1996) [JETP Lett. **63**, 566 (1996)].
4. T. N. Mamedov, I. L. Chaplygin, V. N. Duginov, *et al.*, J. Phys.: Condens. Matter **11**, 2849 (1999).
5. T. N. Mamedov, D. G. Andrianov, D. Herlach, *et al.*, Zh. Éksp. Teor. Fiz. **119**, 1159 (2001) [JETP **92**, 1004 (2001)].
6. T. N. Mamedov, D. G. Andrianov, D. Herlach, *et al.*, Pis'ma Zh. Éksp. Teor. Fiz. **73**, 759 (2001) [JETP Lett. **73**, 674 (2001)].
7. V. N. Gorelkin, T. N. Mamedov, and A. S. Baturin, Physica B (Amsterdam) **289–290**, 585 (2000).
8. G. L. Bir and G. E. Pikus, *Symmetry and Stain-Induced Effects in Semiconductors* (Nauka, Moscow, 1972; Wiley, New York, 1975).
9. H. Neubrand, Phys. Status Solidi B **86**, 269 (1978).
10. R. Abela, C. Baines, X. Donath, *et al.*, Hyperfine Interact. **87**, 1105 (1994).
11. V. N. Gorelkin, T. N. Mamedov, and D. V. Rubtsov, Hyperfine Interact. C **1**, 191 (1996).
12. V. L. Bonch-Bruevich and S. G. Kalashnikov, *Physics of Semiconductors* (Nauka, Moscow, 1990).
13. R. Kubo, Phys. Rev. **86**, 929 (1952).
14. A. G. Milnes, *Deep Impurities in Semiconductors* (Wiley, New York, 1973; Mir, Moscow, 1977).
15. D. Belitz and T. L. Kirpatrik, Rev. Mod. Phys. **66** (2), 261 (1994).
16. M. P. Sarachik, D. R. He, W. Li, *et al.*, Phys. Rev. B **31**, 1469 (1985).
17. A. Roy, M. Turner, and M. P. Sarachik, Phys. Rev. B **37**, 5522 (1988); A. Roy and M. P. Sarachik, Phys. Rev. B **37**, 5531 (1988).

Translated by E. Golyamina

JETP Letters, Vol. 76, No. 7, 2002, pp. 444–449. Translated from Pis'ma v Zhurnal Éksperimental'noĭ i Teoreticheskoĭ Fiziki, Vol. 76, No. 7, 2002, pp. 520–525.

The Coster–Kronig Process Used to Study the Transition of Metal Nanoclusters into a Nonmetallic State

V. D. Borman[1], X. Ch. Lai[2], M. A. Pushkin[1], V. N. Tronin[1], and V. I. Troyan[1, *]

[1] *Moscow Engineering Physics Institute, Moscow, 115409 Russia*

**e-mail: mal@park.mephi.ru*

[2] *China Academy of Engineering Physics, Mianyang, 621900 China*

Received July 25, 2002; in final form, August 28, 2002

The results of an experimental study of the Coster–Kronig process in copper nanoclusters obtained by a pulsed laser deposition technique are presented. It is established that the Köster–Krönig process probability depends on the cluster size and is determined by the possibility of a transition of the metal cluster into a state in which copper exhibits no metallic properties. © *2002 MAIK "Nauka/Interperiodica".*

PACS numbers: 73.22.-f; 71.30.+h

Presently, considerable effort is devoted to studying objects with dimensions in a nanometer range [1–5]. Containing from several dozen to a few hundred atoms, such objects occupy an intermediate position between single atoms and crystalline solids and usually exhibit the physical and chemical properties differing from those of bulk materials of the same composition. This circumstance makes the investigation of nanodimensional objects interesting from the standpoint of both basic science and applications.

As the number of atoms in a cluster increases, the electron structure of the cluster is modified, whereby a set of discrete atomic levels transforms into a continuous band characteristic of the bulk metal. It would be most interesting to reveal the moment of transition by determining a minimum number of atoms in the cluster, at which "metallization" takes place, that is, the system exhibits the transition from a nonconducting state of the molecular dielectric type to a state featuring metallic conductivity. The special properties of nanoobjects can be successfully used in nonlinear optics [6], heterogeneous catalysis [7], and nanoelectronics [8]. For these applications, it is important to establish the limiting properties of nanoobjects and, hence, the limits of miniaturization of the related devices.

The possibility of tracing the transition of a metal cluster into a nonmetallic state in the course of decrease in the cluster size was originally pointed out by Citrin and Wertheim [9]. Subsequently, there were several experimental attempts to detect this transition in metal clusters deposited on various substrates by measuring the blue shift of the plasma frequency [10], polarizability [11], valence [12], and electron tunneling from Fe nanoclusters into GaAs substrate [13]. However, it was difficult to treat the results of these experiments as being due to the transition of metal clusters into a nonmetallic state.

In [7, 14], the transition from metal into a nonmetallic state in Au and Pd clusters deposited on TiO_2 was studied by scanning tunneling spectroscopy (STS). Some features observed in the current–voltage characteristics of metal nanoclusters showed evidence of a certain "effective bandgap" present in the electron structure of clusters, the width of which tends to zero ($E_G \longrightarrow 0$) when the cluster size increases to ~40 Å (to contain ~500 atoms). A important condition for such measurements is the need in using a specially selected narrow-bandgap semiconductor substrate, the bandgap of which would allow the STS measurements while being sufficiently large as compared to the effective bandgap of a cluster studied.

Here we propose an alternative approach to experimental observation of the transition of metal clusters into a nonmetallic state. The method is based on the fact that the intensity of lines in a multiplet structure of the Auger electron spectra, determined by the Köster–Krönig process, depends on the cluster size. As will be demonstrated below, this dependence must be observed for the transition metal clusters with $Z \leq 30$, provided that the spin–orbit splitting energy is greater than the valence band width.

The Coster–Kronig process is essentially the Auger transition in which the initial vacancy (hole) and the electron filling this vacancy (hole) occur in the same electron shell (Fig. 1) [15]. The appearance of a vacancy (hole) on the L_2 level upon the action of radiation on the L level split as a result of the spin–orbit interaction initiates the $L_2L_3M_{45}$ Auger transition. However, the electron transition from L_3 to L_2 with excitation of an M_{45} electron in the valence band (Fig. 1, processes *1* and *2*) is only possible provided that the spin–orbit splitting energy is sufficient to excite an electron in the valence band, due to a large overlap of the wave-

functions of electrons on the L_2 and L_3 levels, the Coster–Kronig process probabilities are higher by one order of magnitude [15] than probabilities of the usual Auger transitions $L_2M_{45}M_{45}$ and $L_3M_{45}M_{45}$ (for brevity, jointly referred to below as the $L_{23}M_{45}M_{45}$ Auger transitions). Therefore, a characteristic time of the Coster–Kronig process is significantly shorter than that of the $L_{23}M_{45}M_{45}$ Auger transition. As a result, the fraction of holes preliminarily created by the exciting radiation on the L_2 sublevel decreases. Therefore, the Coster–Kronig process leads to a decrease in the intensity I_2 of the $L_2M_{45}M_{45}$ line as compared to that (I_3) of the $L_3M_{45}M_{45}$ line. For this reason, the ratio of intensities of these lines exhibits an anomalous growth reaching (e.g., for bulk copper) $I_3/I_2 \approx 8$, which is much greater as compared to the value $I_3/I_2 \approx 2$ characteristic of Cu atoms [16, 17]. This is indicative of the absence of the Coster–Kronig transitions in atoms. In a bulk metal or cluster, the Coster–Kronig process probably takes place due to effective interatomic relaxation (Fig. 1).

In this study, we have experimentally established for copper clusters of decreasing size that the I_3/I_2 ratio varies from 7.8 for $R \approx 100$ Å to 2.3 from $R \approx 20$ Å, which can be evidence of the transition from the metallic state into a state in which copper exhibits no metallic properties.

The electron states of Cu nanoclusters, obtained by pulsed laser deposition (PLD) of copper onto a cleaned surface of highly oriented pyrolytic graphite (HOPG), were studied at room temperature under ultrahigh vacuum conditions ($p \approx 5 \times 10^{-10}$ torr) in a chamber of an XSAM-800 electron spectrometer using X-ray photoelectron spectroscopy (XPS) and Auger electron spectroscopy (AES).[1] The XPS and AES spectra were excited by the MgK_α radiation with $h\nu$ = 1253.6 eV. The composition of the metal deposit was studied *in situ* by XPS.

During the PLD process, radiation of the YAG:Nd^{3+} laser (λ = 1.06 μm) with an energy of E = 80–100 mJ in the Q-switched mode (τ = 15 ns) and a pulse repetition frequency of 25 Hz was focused onto a chemically pure copper target. A system of beam deflecting lenses ensured scanning of the target surface according to a preset program, which allowed the PLD process to be performed in an automated regime, with number of pulses varied from 1 to 10^5. By changing the laser operation parameters and the deposition geometry, it was possible to vary the deposited particle flux density from 10^{12} to 10^{15} cm^{-2} at a pulse duration of $\tau_p \approx 10^{-7}$–10^{-6} s. According to [18], the laser power density of 10^8–10^9 W/cm^2 corresponds to the energy of Cu atoms within 10–100 eV. The ionized beam fraction was about 5%.

[1] The PLD method was developed and used to prepare the Cu clusters on HOPG with active the participation of A.V. Zenkevich.

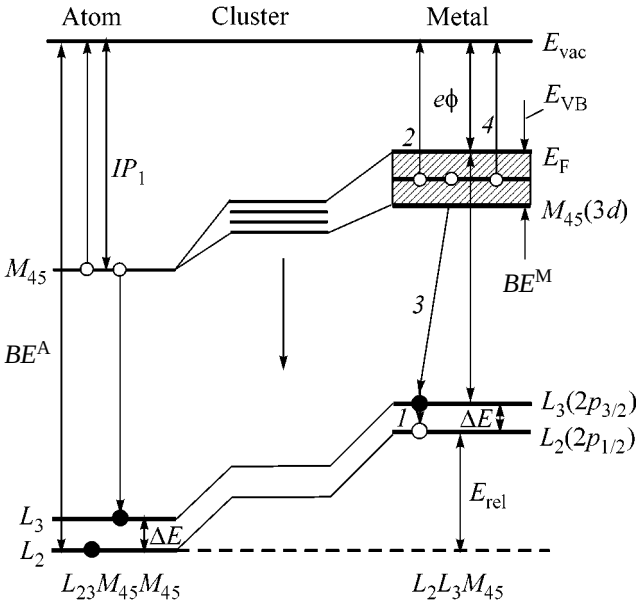

Fig. 1. A schematic diagram showing evolution of the $L_{23}M_{45}M_{45}$ Auger transitions and $L_2L_3M_{45}$ Coster–Kronig processes on the passage from atom to cluster and macroscopic metal: BE^A and BE^M are the binding energies of the core-level electrons in an atoms and metal, respectively; IP is the ionization potential; ϕ is the electron work function of the metal; E_{rel} is the relaxation energy; E_F is the Fermi level; and E_{VB} is the valence band. The primary vacancy formed at the L_2 level is filled by the electron from the L_3 level (process *1*). The liberated energy ΔE is spent to excite an electron in the valence band with the formation of a vacancy (hole) in the valence band (process *2*). The vacancy on the L_3 level, formed as a result of process *1*, is filled by an electron from the valence band (process *3*). The liberated energy is spent to excite a electron in the valence band with the formation of a vacancy (hole) in the valence band (process *4*). Processes *1* and *2* are the Coster–Kronig transitions; processes *3* and *4* are the accompanying usual Auger transitions. As a result of the Coster–Kronig processes and the usual accompanying Auger transitions, the final state is triply ionized.

According to [19], copper is deposited on HOPG so as to form islands of a finite size. Additional investigations, in which Cu was deposited onto NaCl and the deposit was studied by transmission electron microscopy (TEM), showed that, by changing the number of laser pulses from 2×10^3 to 6×10^4, it is possible to obtain clusters with an average size varying from 20–100 Å and the width of the size distribution function much smaller as compared to the case of thermal deposition [4].

In our experiments, the intensity of the $L_{23}M_{45}M_{45}$ Auger transitions in Cu was studied as a function of the number of laser pulses N varied from 500 to 8×10^4. In order to recalculate this into a dependence on the cluster size (or the number of atoms in a cluster), we used the following approach. First, the intensities J_1 and J_2 of the Cu2$p_{3/2}$ and Cu3d XPS lines, respectively, with the

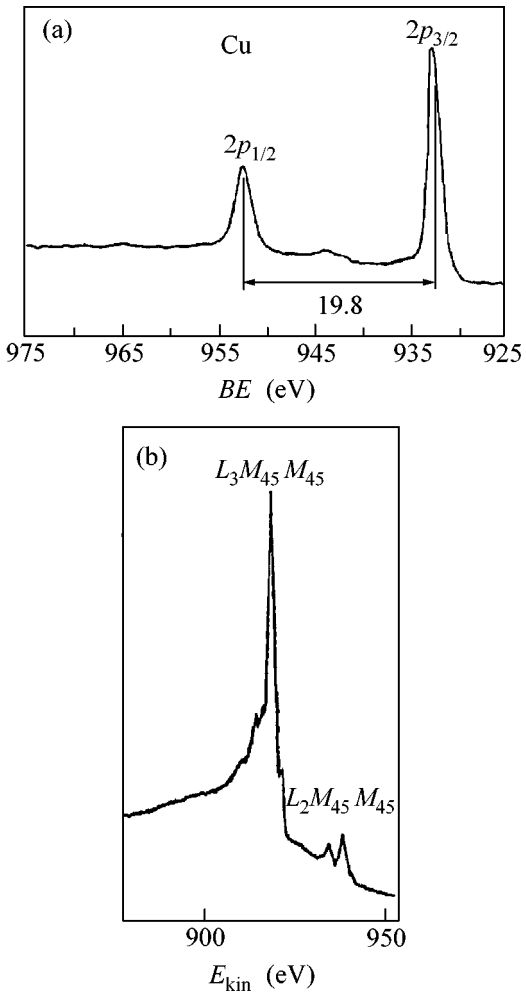

Fig. 2. X-ray photoelectron spectra of $2p_{1/2}$ and $2p_{3/2}$ levels (a) and the $L_3M_{45}M_{45}$ and $L_2M_{45}M_{45}$ Auger electron spectra of single crystal copper (b).

photoelectron free path lengths λ_1 and λ_2 were measured for various numbers N of laser pulses. The ratio of these intensities can be expressed as

$$\frac{J_1}{J_2} = \frac{J_1^0(1-e^{-d/\lambda_1})}{J_2^0(1-e^{-d/\lambda_2})}, \quad (1)$$

where d is the nominal thickness of a deposited film composed of Cu clusters, and J_1^0 and J_2^0 are the XPS peak intensities for $d \gg \lambda$ (bulk metal).

Using relation (1) and taking into account that λ_1 = 13 Å (Cu2$p_{3/2}$, binding energy BE_{2p} = 932.5 eV) and λ_2 = 50 Å (Cu3d, binding energy $BE_{3d} \approx 5$ eV) [19], we readily obtain the dependence $d = f(N)$. This function proved to be linear: $d = KN$, where $K \approx 0.002$ Å/pulse for N = 20–2000 and $K \approx 0.001$ Å/pulse for N = 4000–16000. Taking into that the copper film studied consists of clusters with an average size of $\langle R \rangle$ and a number density n_0, we can relate the nominal film thickness d to these quantities as

$$\langle R \rangle = \left(\frac{3}{2\pi n_0} d\right)^{1/3}. \quad (2)$$

With allowance for the established linear relation between d and N, we arrive at the following relation between the average cluster size and the number of laser pulses N:

$$R = \left(\frac{3K}{2\pi n_0} N\right)^{1/3}. \quad (3)$$

The number density of copper clusters on HOPG is $n_0 \approx 2 \times 10^{-4}$ Å^{-2}, which is close to the value reported for copper on carbon ($n = 1.92 \times 10^{-4}$ Å^{-2}) [19]. This method of determining the average cluster size was also verified for the Au/NaCl system, by comparing the values calculated using relation (3) to the results of direct determination of the cluster size distribution by TEM [3]. Note that the proposed method allows the average cluster size to be determined for the system studied *in situ* in the spectrometer chamber.

Figure 2 presents the Cu2$p_{1/2}$ and Cu2$p_{3/2}$ XPS spectra (a) and the AES spectra of $L_{23}M_{45}M_{45}$ transitions (b) for the standard samples of single crystal copper. As can be seen, the spin–orbit splitting between $2p_{1/2}$ and $2p_{3/2}$ levels amount to ΔE = 19.8 eV, which coincides with the published value [15]. The ratio of intensities of the L_3 and L_2 lines is $I_3/I_2 \approx 8$. The $L_3M_{45}M_{45}$ spectrum exhibits additional satellites with E_{kin} below the transition energy. These satellite peaks are due to the interaction of Auger electrons with the triply ionized M_{45} valence electron states (Fig. 1) arising due to the Coster–Kronig process.

Figure 3 shows the AES spectra of $L_3M_{45}M_{45}$ and $L_2M_{45}M_{45}$ transitions in copper clusters deposited onto the HOPG surface by different numbers of laser pulses. It is seen that, as the N value increases, the intensity of line L_3 grows faster than the intensity of line L_2.

Using the AES spectra of $L_{23}M_{45}M_{45}$ transitions experimentally measured for various numbers N of laser pulses, we constructed a plot of the intensity ratio I_3/I_2 versus average cluster size R (Fig. 4). The transition from the number of laser pulses to the average size of Cu clusters was performed according to formula (3). As can be seen from Fig. 4, an increase in the cluster size is accompanied by a growth in the ratio of intensities of $L_3M_{45}M_{45}$ and $L_2M_{45}M_{45}$ transitions: as $\langle R \rangle$ changes from 18 to 100 Å, the I_3/I_2 ratio grows from 2.2 to 7.8. It should be recalled that the ratio for a bulk solid tends to 8 [16, 17]. This result shows that the Auger spectra of Cu nanoclusters reflect the Coster–Kronig process, the probability of which depends on the cluster size. A deviation from the value $I_3/I_2 \approx 2$ corresponding to the transitions in Cu atoms is observed even for $R_c \approx$

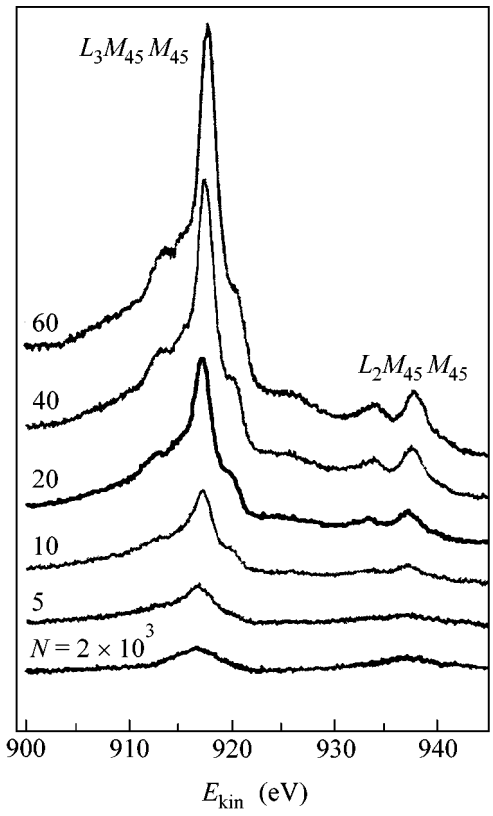

Fig. 3. Variation of the intensities of the $L_3M_{45}M_{45}$ and $L_2M_{45}M_{45}$ Auger electron transitions in Cu clusters deposited on HOPG by increasing number of laser pulses N.

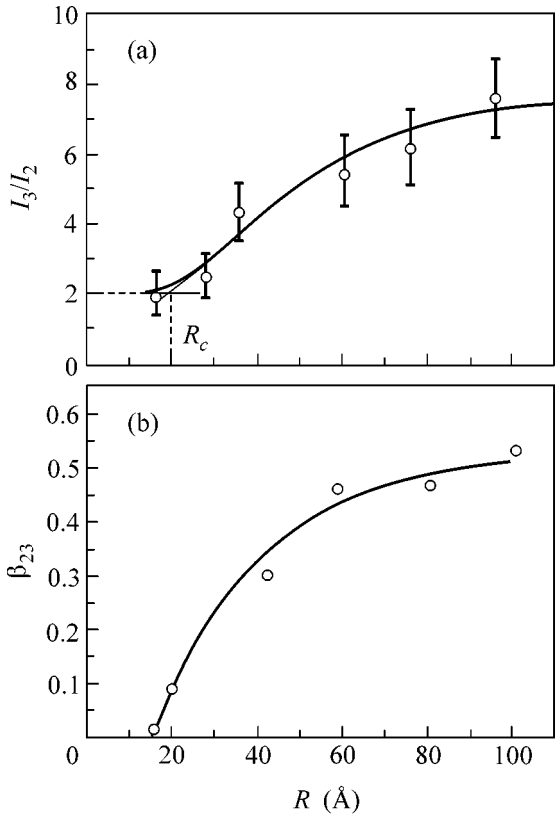

Fig. 4. Plots of (a) the ratio I_3/I_2 of the intensities of $L_3M_{45}M_{45}$ and $L_2M_{45}M_{45}$ Auger electron transitions and (b) the Coster–Kronig process probability β_{23} versus the Cu nanocluster size R.

20 Å. Thus, this R_c value can be treated as the cluster size below which nonmetallic properties of the clusters are manifested.

According to the results of estimates, the number of Cu atoms in the cluster with a radius of $R_c \approx 20$ Å is $n \approx 1/2(R/R_0)^3$, where $R_0 = 3.61$ Å is the Wigner–Seitz radius for Cu. Note that the fractions of atoms occurring in the surface (n_s) and in the bulk (n_v) for the cluster with $R_c \approx 20$ Å are $n_s/n_v \approx 0.4$ and $n_v/n \approx 0.6$, respectively. It is a difference in the electron states of atoms on the surface as compared to those in the bulk, which accounts for a shift in the binding energy of the core-level electrons of the surface atoms in metal clusters [9, 20]. This energy depends on the density of electron states in the valence band, which is determined by the average size of a nanocluster [1,20]. These results [9, 20] indicate that the electron states exhibit evolution on the passage from the metal to atomic state via intermediate nanoclusters. Indeed, the electron configuration of the valence shells of copper is $3d^{10}4s^1$. As a result of the s–d hybridization, the valence band of Cu corresponds to $3d^{9.6}4s^{1.4}$ [21]. Therefore, a decrease in the cluster size (i.e., the transition from solid Cu to atom) is accompanied by rehybridization and, hence, the x value in the electron band structure $3d^{10-x}4s^{1+x}$ must depend on the cluster size, varying from $x = 0$ for $R_c \longrightarrow 0$ to $x = 0.4$ for $\langle R \rangle \longrightarrow \infty$.

The increase in the I_3/I_2 ratio from 2.2 to 7.8 for the $L_2L_3M_{45}$ transitions in copper, accompanying the growth of the cluster size from 20 to 100 Å, can be related to the Coster–Kronig process in the systems with a finite number of copper atoms and explained within the framework of the known mechanisms of evolution of the electron states in metal clusters. As the nanocluster size decreases, the degree of hybridization x drops from 0.4 to 0 and the valence band exhibits narrowing [6, 16]. This can be considered as evidence that the valence band structure disappears and, for the Cu coverage on the HOPG surface studied, transforms into atom-like electron wavefunctions. In this case, the Coster–Kronig process probability must decrease and, in the limit of individual Cu atoms, tend to zero. The ratio of the Auger line intensities I_3/I_2 must tend to the ratio of the statistical weights $2j + 1$ of the split $j = l \pm s$ sublevels, which equals 2 for the Cu$2p_{3/2}$ and Cu$2p_{1/2}$ levels.

Following Yin *et al.* [16], the ratio I_3/I_2 can be related to the corresponding Coster–Kronig process probability β_{23}:

$$\frac{I_3}{I_2} = \left(\frac{\beta_{23} + n_3/n_2}{1-\beta_{23}}\right)\frac{\Gamma_3}{\Gamma_2}, \quad (4)$$

where n_2 and n_3 are the hole occupancies of the atomic levels L_2 and L_3 determined by statistical weights of the corresponding states (for copper, $n_3/n_2 = 2$) and Γ_3 and Γ_2 are the widths of the L_3 and L_2 levels. For the crystalline copper, $\beta_{23} = 0.64$ [16]. Using formula (4) and taking into account experimental dependence of the I_3/I_2 ratio on the cluster size R (Fig. 4a), we can study the probability β_{23} as a function of R. This dependence is presented in Fig. 4b, where it was taken into account that $\Gamma_3/\Gamma_2 \approx 1$ for the atomic copper and $\Gamma_3/\Gamma_2 \approx 1.1$ for the crystalline copper. As can be seen from Fig. 4, the Coster–Kronig process probability decreases to zero for copper clusters with $R = R_c \approx 20$ Å.

The emission of M_{45} electrons from the valence band via the Coster–Kronig process can take place provided that the spin–orbit splitting energy $\Delta E = E_{L_3} - E_{L_2}$ is greater than the valence band width E_{VB} [22]. In copper this condition is satisfied and, hence, the Coster–Kronig process has to be observed. According to estimates, the inequality

$$\Delta E > E_{VB}(M_{45}|L_2^*), \quad (5)$$

is always valid for $E_{VB}(M_{45}|L_2^*)$ representing the binding energy of $M_{45}(3d)$ electrons in the presence of a hole on the $L_2(2p_{1/2})$ level.

Indeed, in the approximation of equivalent orbitals [23], condition (5) can be written as

$$\Delta E > E_{VB}^{z+1}(M_{45}). \quad (6)$$

This inequality is always valid, since we have $\Delta E = 19.8$ eV (for Cu with $Z = 29$) and $E_{VB}^{Z+1}(M_{45}) = 10.2$ eV (for Zn with $Z = 30$).

Taking into account that the separation of lines in the multiplet structure of Cu is retained in the gas and crystal phases [15], we can show that the energy conditions for the Coster–Kronig process are not satisfied for copper in the atomic state. Indeed, comparing the value $\Delta E \approx 19.8$ eV to the ionization potential of the Cu^+ ion, $IP_1 \approx 20$ eV, we see that $\Delta E < IP_1$. This indicates that the Coster–Kronig process is impossible in atoms.

Thus, we established that the Coster–Kronig process is possible only in the metallic copper and cannot take place in Cu atoms. We believe that this difference is due to the effects of interatomic relaxation, which results in a decrease of the IP_1 value by an amount on the order of E_{rel} (Fig. 1). This hypothesis is confirmed by the results reported in [16], according to which the I_3/I_2 ratio is 7.85 for metallic copper and $I_3/I_2 \approx 2.17$ for copper vapor.

Thus, the observed relation between the intensity ratio I_3/I_2 for the $L_2L_3M_{45}$ transitions and the dimensions of Cu nanoclusters deposited on HOPG can be explained by a decrease in probability of the Coster–Kronig process with decreasing cluster size, that is, with the transition of copper from the metallic state to a nonmetallic state described by quasiatomic wavefunctions. The number of atoms or the cluster size (R_c) for which a transition to the metallic state takes place can be estimated, for the simplest case of the *s* band, from a condition of delocalization for the *s* electrons whereby the distance between levels $\delta E \approx E_{VB}/2n$ will become comparable with kT. This yields $R_c \approx R_0(E_{VB}/kT)^{1/3} \approx 22$ Å ($E_{VB} \approx 5$ eV is the valence band width), which corresponds to the number of atoms in the cluster with $N = 100$ atoms. The estimated cluster size $R_c \approx 22$ Å is comparable with that ($R_c \approx 20$ Å) estimated for Cu from the I_3/I_2 curve (Fig. 4b), which is additional evidence that the nanoclusters of Cu on HOPG exhibit the transition to a nonmetallic state at a cluster size of $R \approx R_c \approx 20$ Å.

Using the results presented above, it is possible to study the transition to the metallic state for 3*d* metal clusters on various substrates by measuring only the $L_2L_3M_{45}$ transitions involving the Coster–Kronig process. For the elements with $Z \leq 30$ (Zn), the Coster–Kronig process is possible, because the energy difference between the $2p_{3/2}$ and $2p_{1/2}$ levels (ΔE) is greater than the binding energy of 3*d* electrons (E_{VB}): $\Delta E > E_{VB}$. For the elements with $Z > 30$, the Coster–Kronig process is unlikely, since the E_{VB} value increases with Z faster than does ΔE. It should be noted that the series of the $L_{23}M_{45}M_{45}$ Auger lines accompanied the XPS spectra excited by the same MgK_α source.

It is possible to note an analogy in the character of the $L_{23}M_{45}M_{45}$ Auger spectra of transition metals and nanoclusters (in particular, for Cu). As was demonstrated in [24, 25], the Auger spectra of metals with $Z > 30$ (for which the effective Coulomb interaction U_{eff} of two holes in the final $L_{23}M_{45}M_{45}$ state is greater than the band width Γ: $U_{eff} > 2\Gamma$) exhibit a quasiatomic structure and the Coster–Kronig process is absent [26]. In contrast, in the metals with $Z \leq 30$ (where $U_{eff} < 2\Gamma$), the Auger spectra reflect the band structure and the Coster–Kronig process is observed.

The nanoclusters of Cu on HOPG also exhibit a decrease in the valence band width [20] with decreasing cluster size, which is evidence of a transition from the band to quasiatomic structure of the valence band. As was indicated above, this is accompanied by vanishing of the Coster–Kronig process.

REFERENCES

1. É. L. Nagaev, Usp. Fiz. Nauk **162** (9), 49 (1992) [Sov. Phys. Usp. **35**, 747 (1992)].
2. W. A. de Heer, Rev. Mod. Phys. **65**, 611 (1993).
3. V. D. Borman, A. V. Zenkevich, X. Ch. Lai, *et al.*, Pis'ma Zh. Éksp. Teor. Fiz. **72**, 216 (2000) [JETP Lett. **72**, 148 (2000)].
4. V. D. Borman, A. V. Zenkevich, M. A. Pushkin, *et al.*, Pis'ma Zh. Éksp. Teor. Fiz. **73**, 684 (2001) [JETP Lett. **73**, 604 (2001)].
5. A. V. Zenkevitch, M. A. Pushkin, V. N. Tronin, *et al.*, Phys. Rev. B **65**, 073406 (2002).
6. D. Ricard, P. Ronssgnol, and C. Flytzanie, Opt. Lett. **10**, 511 (1985).
7. M. Valden, X. Lai, and D. W. Goodman, Science **281**, 1647 (1998).
8. S. H. M. Persson and L. Olofson, Appl. Phys. Lett. **74**, 2546 (1999).
9. P. H. Citrin and G. K. Wertheim, Phys. Rev. B **27**, 3176 (1983).
10. N. Nilius, N. Ernst, and H.-J. Freund, Phys. Rev. Lett. **84**, 3994 (2000).
11. W. D. Knight, K. Clemenger, W. A. de Heer, *et al.*, Phys. Rev. B **31**, 2539 (1985).
12. M. Lübcke, B. Sonntag, W. Niemann, *et al.*, Phys. Rev. B **34**, 5184 (1986).
13. P. First, J. Stroscio, and R. Dragoset, Phys. Rev. Lett. **63**, 1416 (1989).
14. C. Xu, X. Lai, G. W. Zaiac, and D. W. Goodman, Phys. Rev. B **56**, 13464 (1997).
15. *Electron and Ion Spectroscopy of Solids*, Ed. by L. Fiermans, J. Vennik, and W. Dekeyser (Plenum, New York, 1978; Mir, Moscow, 1981).
16. Lo I Yin, I. Adler, M. H. Chen, and B. Vrasemann, Phys. Rev. A **73**, 897 (1973).
17. Seppo Aksela and Jyrki Sivonen, Phys. Rev. A **25**, 1243 (1982).
18. A. Zenkevitch, J. Chevallier, and I. Khabelashvili, Thin Solid Films **311**, 119 (1997).
19. D.-Q. Yang, M. Meunier, and E. Sacher, Appl. Surf. Sci. **173**, 134 (2001).
20. V. N. Nevolin, A. V. Zenkevitch, X. Ch. Lai, *et al.*, Laser Phys. **11**, 45 (2001).
21. A. R. Williams and N. D. Lang, Phys. Rev. Lett. **40**, 954 (1978).
22. M. H. Chen, B. Vrasemann, and V. O. Kostroum, Phys. Rev. A **4**, 1 (1971).
23. S. P. Kowalchuk, Phys. Rev. B **8**, 2387 (1973).
24. E. Antonides, E. C. Janse, and G. A. Sawatzky, Phys. Rev. B **15**, 4596 (1977).
25. G. A. Sawatzky, Phys. Rev. Lett. **39**, 504 (1977).
26. N. Martenson and R. Naholm, Phys. Rev. B **24**, 7121 (1981).

Translated by P. Pozdeev

JETP Letters, Vol. 76, No. 7, 2002, pp. 450–455. Translated from Pis'ma v Zhurnal Éksperimental'noĭ i Teoreticheskoĭ Fiziki, Vol. 76, No. 7, 2002, pp. 526–531.

Phase Diagram of the Bose Condensation of Interwell Excitons in GaAs/AlGaAs Double Quantum Wells

A. A. Dremin*, V. B. Timofeev*, A. V. Larionov*, J. Hvam, and K. Soerensen****

** Institute of Solid State Physics, Russian Academy of Sciences, Chernogolovka, Moscow region, 142432 Russia*

*** Microelectronic Center, DK 2800 Lyngby, Denmark*

e-mail: timofeev@issp.ac.ru

Received August 28, 2002

The luminescence of interwell excitons in GaAs/AlGaAs double quantum wells (*n–i–n* heterostructures) with large-scale fluctuations of random potential in the heteroboundary planes was studied at low temperatures down to 0.5 K. The properties of excitons whose photoexcited electron and hole are spatially separated in the neighboring quantum wells by a tunneling barrier were studied as functions of density and temperature. The studies were performed within domains about one micron in size, which played the role of macroscopic traps for interwell excitons. For this purpose, the sample surface was coated with a metal mask containing special openings (windows) of a micron size or smaller. Both photoexcitation and observation of luminescence were performed through these windows by the fiber optic technique. At low pumping powers, the interwell excitons were strongly localized because of the residual charged impurities, and the corresponding photoluminescence line was nonuniformly broadened. As the laser excitation power increased, a narrow line due to delocalized excitons arose in a threshold-like manner, after which its intensity rapidly increased with growing pumping and the line itself narrowed (to a linewidth less than 1 meV) and shifted toward lower energies (by about 0.5 meV) in accordance with the filling of the lowest exciton state in the domain. An increase in temperature was accompanied by the disappearance of the line from the spectrum in a nonactivation manner. The phenomenon observed in the experiment was attributed to Bose–Einstein condensation in a quasi-two-dimensional system of interwell excitons. In the temperature interval studied (0.5–3.6) K, the critical exciton density and temperature were determined and a phase diagram outlining the exciton condensate region was constructed. © *2002 MAIK "Nauka/Interperiodica".*

PACS numbers: 73.21.Fg; 73.20.Mf

In recent years, the interest in Bose–Einstein condensation has been stimulated by major achievements concerned with the observation and investigation of this phenomenon in dilute and deeply cooled gases of atoms confined in magnetic traps [1]. Because of the large atomic masses, the critical temperatures of the Bose–Einstein condensation in dilute gases are on the order of microkelvin or even lower. In a semiconductor, a hydrogen-like exciton, being a composite boson, has a mass that is several orders of magnitude smaller. Therefore, the Bose–Einstein condensation in a dilute gas of hydrogen-like excitons is expected to occur at much higher temperatures of about 1 K [2]. In the last few years, the Bose–Einstein condensation of excitons in 2D systems obtained on the basis of semiconductor heterostructures has been the object of intensive research [3–19].

Earlier, we studied the photoluminescence of interwell excitons in GaAs/AlGaAs double quantum wells containing long-period fluctuations of random potential in the heteroboundary planes [19]. The large-scale fluctuations were obtained by using the growth interruption technique at the heteroboundaries of the quantum wells [20]. The properties of interwell excitons were studied by varying their concentration and temperature within single domains whose size was about 1 μm. To work with a single domain, the surface of the structure was coated with an opaque metal mask that had lithographically made windows of a micron size or smaller, through which the photoexcitation and the subsequent observation of photoluminescence were performed. In a single domain, which essentially played the role of a macroscopic trap, it was easier to accumulate the interwell excitons up to the critical densities at which the excitons began to exhibit collective properties. In the conditions of the resonance laser excitation that generated intrawell 1s HH excitons, it was found that, at low powers and sufficiently low temperatures, the interwell excitons are strongly localized while the corresponding photoluminescence line is nonuniformly broadened (a half-width of about 2.5 meV). As the resonance excitation power increases, the narrow line of delocalized interwell excitons arises in a threshold-like manner (the minimal linewidth is less than 350 μeV). On further increase in the pumping power, the intensity of this line grows, and the line itself is somewhat shifted to lower energies (by about 0.5 meV), in accordance with the filling of the lowest state in the domain. When the tem-

perature grows at constant pumping, this line disappears from the spectrum in a nonactivation manner: the line intensity decreases according to a power law with increasing temperature. This phenomenon testifies to the Bose condensation in the quasi-two-dimensional system of interwell excitons under the conditions of the spatial constraint that is determined by the size of the lateral domains varying within approximately 1 μm. In view of the fact that the width of the narrow line in question remains practically constant with varying temperature, its appearance in the luminescence spectrum can be attributed to the part of excitons condensed at $\mathbf{K} = 0$. For the temperature interval studied in our previous experiments (1.5–3.4) K, it was found that the critical values of the exciton density and temperature are related by a dependence close to linear. This paper studies the Bose condensation of interwell excitons in a heterostructure of the same architecture at lower temperatures, down to 0.5 K. The main purpose of this study is to determine the phase diagram of this collective phenomenon in the temperature interval (0.5–3.4) K.

We studied a GaAs/AlGaAs *n–i–n* heterostructure with GaAs/AlAs/GaAs double quantum wells. The width of the GaAs quantum wells was 12 nm, and the width of the AlAs four-monolayer barrier was 1.1 nm. The structure was grown by molecular beam epitaxy on the (001) surface of an *n*-doped GaAs substrate (Si doping to a concentration of 2×10^{18} cm^{-3}). First, a 0.5-μm-thick GaAs buffer layer doped with Si to a concentration of 2×10^{18} cm^{-3} was grown on the substrate. The next layer was an insulating one ($x = 0.33$), 12 mm in thickness. Then, the GaAs/AlAs/GaAs double quantum well was grown. The well was covered with another 12-nm-thick insulating layer ($x = 0.33$), which contained an AlAs/$Al_xGa_{1-x}As$ ($x = 0.33$) ten-period superlattice with a period of 3 nm. The next layer was conducting, its thickness was 0.1 μm, and it consisted of GaAs doped with Si to a concentration of 2×10^{18} cm^{-3}. The whole structure was covered with a 10-nm-thick GaAs insulating layer (the top layer). At the boundaries of the double quantum wells, AlAs four-monolayer barriers were grown. The epitaxial growth of these barriers was performed using the growth interruption technique. This technique provided the formation of long-period lateral fluctuations of random potential that were related to the fluctuations of the AlAs barrier widths. Metallic contacts made of Cr/Ge/Au alloy were applied to the buffer layer and to the doped layer in the upper part of the mesa.

The surface of the *n–i–n* structure of architecture described above was coated with a metal mask (a 120-nm-thick aluminum film) containing openings (windows) up to 0.5 μm in diameter. The mask was fabricated by the lift-off electron beam lithography. As a result, the surface of the sample had the form of a regular rectangular array of windows that were transparent to light. The spacing between the windows was

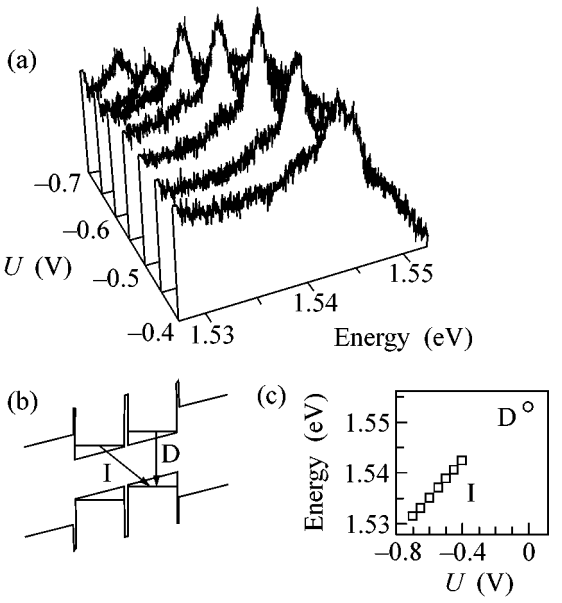

Fig. 1. (a) Behavior of the luminescence spectra of interwell excitons as a function of bias voltage at $T = 0.55$ K. (b) Schematic diagram of optical transitions and (c) the dependence of the spectral positions of the direct (D) and interwell (I) excitons on the bias voltage.

150 μm. In the experiment, the excitation and the detection of the luminescence signal were performed through single windows. We emphasize that the aluminum film was not connected with the n^+ contact area of the heterostructure.

To study the luminescence spectra at temperatures of (0.5–1.4) K, the sample was placed in a low-temperature chamber in which He^3 vapor was condensed. The sample was immersed in liquid helium. The temperature was controlled by pumping He^3 vapor through a cryogetter pump and measured by a resistance thermometer.

For the excitation of luminescence and for the measurement of the luminescence signal, we used the fiber-optic technique. The experiment was performed with a 50-μm light guide. With the help of a specially designed device, the center of the light guide was positioned in front of the micron-size window. The luminescence was excited by a single-mode cw He–Ne laser. To minimize the effect of scattered light, a linear polarizer was placed before the entrance slit of a double monochromator (Ramanor 1000), so that the polarization direction was orthogonal to the polarization of the exciting laser radiation. The luminescence spectra at the exit of the monochromator were measured by a CCD camera.

The results testifying to the exciton condensation were obtained from the experiment with the excitation through a mask window that was less than 1 μm in diameter. Figure 1 presents the experimental lumines-

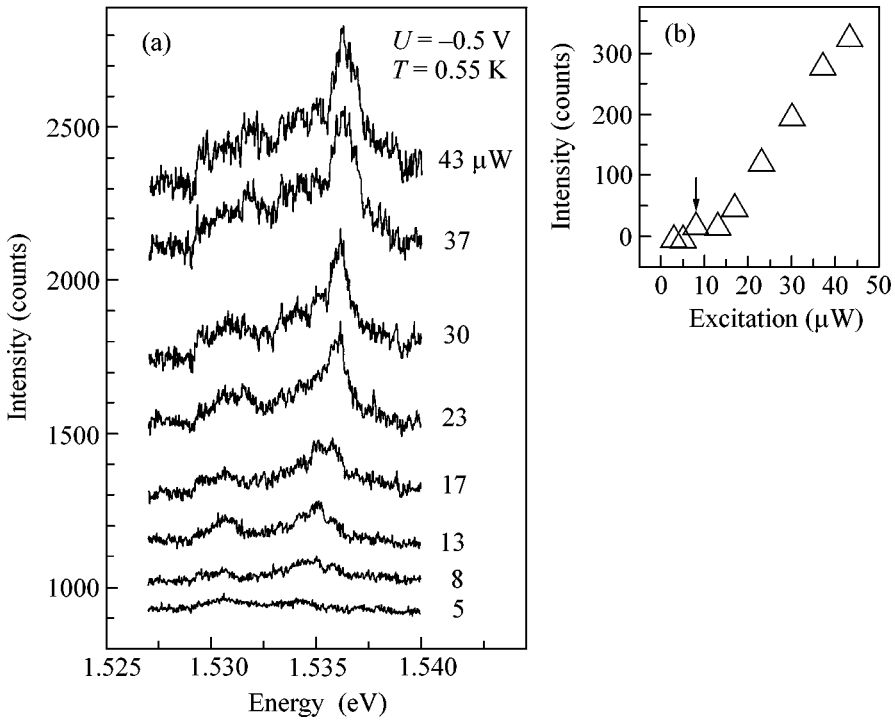

Fig. 2. (a) Luminescence spectra of an interwell exciton (the I line) for different He–Ne laser excitation powers at the bias voltage $U = -0.5$ V and $T = 0.55$ K. (b) Dependence of the intensity of the interwell exciton line on the optical pumping power. The arrow indicates the threshold power at which the I line arises in the spectrum.

cence spectra of interwell excitons (the I line) that were obtained at different bias voltages, at a helium bath temperature of 0.55 K. The optical transitions are schematically illustrated in Fig. 1b. In the intrawell luminescence region, which is not shown in Fig. 1, at zero bias voltage, two lines are observed: a free heavy-hole exciton, i.e., a 1sHH exciton, and a bound exciton [18]. The line corresponding to interwell excitons (the I line) arises in the spectrum when, in the presence of a bias electric field, the value of the Stark shift of the dimensional quantization energy bands, $eF\Delta z$, begins to exceed the difference between the binding energies of the intrawell and interwell excitons: $eF\Delta z > E_D - E_I$. From Fig. 1, it follows that the interwell exciton line is shifted linearly (to a high accuracy) with varying electric field (see also Fig. 1c). This is direct evidence that the I line is associated with an interwell exciton whose electron and hole are in neighboring quantum wells separated by a barrier transparent to tunneling. As the bias voltage increases, the times of the radiative annihilation of interwell excitons change; namely, they increase by more than an order of magnitude because of the decrease in the overlapping of the electron and hole wave functions of the exciton across the barrier. In this case, as seen from Fig. 1, the luminescence intensity under the conditions of steady-state excitation varies only slightly. This fact supports the previously made conclusion [19] that the quantum yield of luminescence of interwell excitons is sufficiently high, and the radiationless transitions can be ignored. In its turn, this result testifies to the high quality of the heterostructure under investigation.

At low excitation powers, below 10 μW, at $T = 0.55$ K, the luminescence spectrum is represented by a relatively broad asymmetric band (the bandwidth is about 3 meV, see Fig. 2). This band is nonuniformly broadened, and, in our opinion [19], its origin is related to the strong localization of interwell excitons by the random potential fluctuations because of the residual charged impurities. As the pumping power grows (>10 μW), a narrow line arises in a threshold-like manner at the violet edge of the broad band, the intensity of this narrow line increasing with the further increase in the pumping power. Qualitatively, the situation develops with increasing pumping in the same way as in the case of the resonance excitation at higher temperatures $T >$ 1.5 K [19]. The intensity of the narrow I line grows with increasing pumping power according to a linear law (see Fig. 2b), but this growth is much faster than that of the structureless luminescence background observed below this line. The I line itself is shifted with growing pumping power by approximately 0.5 meV toward lower energies. The minimal width of the I line is 0.7 meV; i.e., in the case of the excitation by a He–Ne laser, this line is approximately twice as wide as in the case of the resonance excitation by a Ti–sapphire laser with the same spectral resolution. The structureless luminescence band under the I line increases linearly

with increasing excitation power. As the pumping power grows further (above 50 μW), the narrow line of interwell excitons begins to broaden and then, broadening monotonically, shifts toward higher energies because of the screening of the bias electric field. Hence, from the value of the spectral shift, it is possible to estimate the concentration of the interwell excitons by the Gauss formula:

$$\delta E = 4\pi e^2 ND/\varepsilon, \quad (1)$$

where d is the distance between the spatially separated e–h layers, N is the exciton density, and ε is the dielectric constant. For example, if we take the distance between the electron–hole layers equal to 10 nm, the I line will be shifted by 1.4 meV toward higher energies at an interwell exciton concentration of 10^{10} cm^{-2}.

Earlier, it was demonstrated that the narrow line of interwell excitons disappears from the luminescence spectra at $T > 3.4$ K. Below, we present an example illustrating the sensitivity of this phenomenon to temperature (see Fig. 3). Figure 3a shows that, at $T = 1.29$ K, the narrow line vanishes against the background of the structureless luminescence band of localized excitons when the exciting laser power decreases below $P <$ 14 μW. However, if we fix the critical power at a level of 14 μW, which corresponds to the disappearance of the line from the spectrum, and then reduce the temperature of the sample, the narrow line reappears at the violet edge of the structureless continuum and its intensity increases with further cooling (see Fig. 3b). Even at temperatures $T < 1.14$ K and lower, the narrow line is clearly visible in the spectra, its intensity growing with decreasing temperature. For the region $T <$ (0.5–1.5) K, we found that the behavior of the intensity of this line as a function of temperature obeys the relation

$$I_T \sim (1 - T/T_c)^{\alpha}, \quad (2)$$

where I_T is the intensity of the line at a temperature T, T_c is the critical temperature at which the narrow line disappears from the spectrum, and $\alpha \approx 1$ is the exponent.

Judging from the behavior of the narrow line of interwell excitons as a function of temperature, one can see that the phenomenon observed in our experiments demonstrates all characteristic features of the phase transition associated with the Bose condensation of excitons; i.e., as soon as the critical values of density and temperature are reached, a new collective phase of interwell excitons comes into play. Therefore, we tried to determine the form of the phase diagram under the conditions of Bose condensation of interwell excitons. For this purpose, at every given temperature in the interval under study T = (0.5–3.6) K, we investigated the dependence of the luminescence spectra on the pumping power and determined the threshold power P_c at which the narrow line begins to appear in (or disappear from) the spectrum. Thus, the phase diagram was constructed in ($P_c - T$) coordinates, and for its construction, we used the region where the dependence of the intensity of the narrow line on the laser excitation power was linear. The resulting phase diagram is presented in Fig. 4 in both linear and logarithmic coordinates (see the inset in Fig. 4). Experimentally, it was found that, from the point of view of the e–h pair generation in the double quantum wells, the excitation by a He–Ne laser is almost five times more efficient than the resonance excitation by a Ti–sapphire laser. This result is explained by the low coefficient of resonance absorption in the double quantum wells. In Fig. 4, the experimental points obtained with He–Ne and Ti–sapphire lasers are represented by different symbols. The range of the pumping power variation was within approximately an order of magnitude (from ten to two hundred

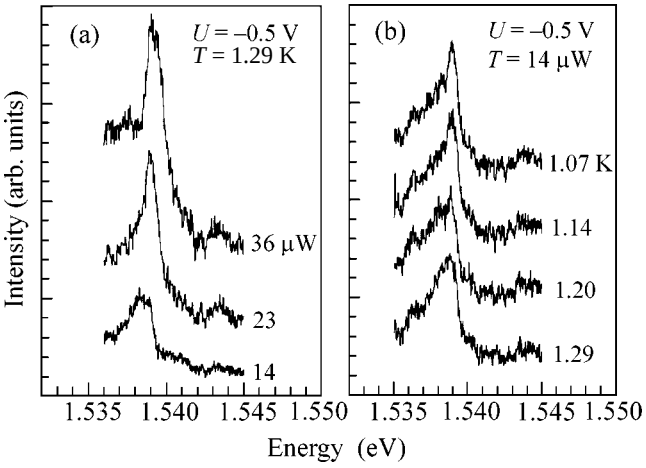

Fig. 3. (a) Dependence of the intensity of the I line on the pumping power at $T = 1.29$ K and at a bias voltage of –0.5 V. (b) Behavior of the spectra at a pumping power of 14 μW in the course of the gradual cooling of the structure. The I line appears in the spectrum at $T < 1.2$ K.

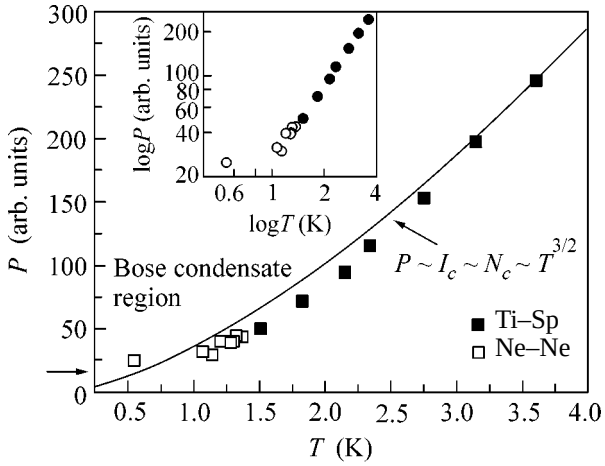

Fig. 4. Phase diagram of the Bose condensation of interwell excitons in the temperature interval T = (0.5–3.6) K.

microwatts). The concentration of the interwell excitons could be estimated judging from the shift of the narrow line toward higher energies at high pumping powers because of the screening of the bias voltage. At the minimal temperature achieved in the experiment, $T = 0.55$ K, and at a pumping power of 10 μW, when the narrow line arises in the spectrum in a threshold-like manner, the exciton density estimated by Eq. (1) is $N_c(T = 0.55\ \text{K}) = 3 \times 10^9\ \text{cm}^{-2}$. In the phase diagram presented in Fig. 4, the scales of the pumping power, narrow line intensity, and interwell exciton density are linearly related ($P \sim I \sim N$).

The phase diagram obtained by us has an unusual form. In the temperature interval (1.2–3.6) K, the critical densities and temperatures, at which the condensation takes place, are related to each other by the power law

$$N_c \sim T_c^{\alpha}, \tag{3}$$

where $\alpha = 3/2$. This power law is an unexpected result. The point is that, in the presence of a lateral spatial constraint, the critical temperature should be related to the density of noninteracting excitons by the law that is close to linear:

$$T_c \approx \pi\hbar^2 N_{\text{ex}}/gk_B m_{\text{ex}} \ln(N_{\text{ex}} S), \tag{4}$$

where $g = 4$ characterizes the spin degeneracy of the exciton state, m_{ex} is the translational mass of the exciton, and S is the area of the lateral constraint. A possible reason for the deviation from this dependence is that the system under study is quasi-two-dimensional, while the gas of interwell excitons is nonideal, because interwell excitons interact with each other.

At the temperatures $T < 1.2$ K and down to 0.5 K, where the strong localization effects are most pronounced, the relation between the critical density and critical temperature cannot be described by a simple power law. It should be also emphasized that the Bose condensation under study manifests itself on the scale of exciton concentrations in certain limits: $N_{\text{loc}} < N_{\text{ex}} < N_{I-M}$. The lower limit corresponding to low concentrations is caused by the effects of the strong localization of interwell excitons by the defects inside the domain (trap). We estimate the density of the localized states in the structures under investigation as $N_{\text{loc}} \approx 3 \times 10^9\ \text{cm}^{-2}$. It is precisely the localized states that are likely to be responsible for the unusual form of the phase diagram at the lowest temperatures. The upper limit (high concentrations) is caused by the collapse of excitons as a result of the insulator-to-metal transition, N_{I-M}. Indeed, as the power of the He–Ne laser excitation increases above 200 μW, the luminescence line of interwell excitons begins broadening and shifts to higher energies. The shift of the I line occurs because of the screening of the bias electric field, while its broadening is caused by the overlapping of the exciton wave functions in the quantum well plane and the Fermi repulsion between electrons in one well and between holes in the other well. We estimate the density at which the interwell excitons collapse and an electron–hole plasma with spatially separated electrons and holes is formed as $N_{I-M} < 10^{11}\ \text{cm}^{-2}$. This density corresponds to the dimensionless parameter $r_S = 1/\sqrt{\pi N_{I-M}}\, a_B < 2$.

In the recent publication [21], Bose condensation was considered in a system of noninteracting two-dimensional excitons in the presence of a discrete spectrum of localized states below the continuum of extended exciton states. In this publication, it was pointed out that, because of the physical limitations, even in the presence of a single discrete level ε_0 lying below the exciton mobility threshold, the chemical potential of excitons μ does not become equal to zero when the critical condensation conditions are reached, namely: $-\mu > -\varepsilon_0 = |\varepsilon_0|$, i.e., $|\mu|_{\min} = |\varepsilon_0|$. This means that, when the critical temperature is reached, the maximal number of extended exciton states $(N_{\text{ex}})_{\max}$ are formed. When the temperature becomes lower than the critical one T_c, the concentration N becomes greater than $(N_{\text{ex}})_{\max}$ and the excess Bose particles, $N - (N_{\text{ex}})_{\max}$, should condense into localized states in macroscopic quantities. If we return to the experiments considered above, at the excitation powers below the threshold values, we can see a wide, nonuniformly broadened luminescence band that corresponds to the continuum of localized states. However, above the threshold, a single narrow line arises with an intensity that grows much faster than the structureless continuum below it. The narrow line appears near the mobility edge of the delocalized exciton states [6]. These observations disagree with the conclusion of the cited paper [21]. Presumably, in the system under investigation, in the presence of localized states and in the presence of the spatial constraint related to the lateral size of domains (traps), the Bose condensation of delocalized interwell excitons follows a more complicated scenario.

We are grateful to S.I. Dorozhkin for supplying us with a He^3 low-temperature chamber, to A.V. Bazhenov for the assistance in the experiment, and to S.V. Dubonos for the electron-beam lithography on the heterostructure. The work was supported in part by the Russian Foundation for Basic Research (project nos. 01-02-16471, 02-01-06349, and 02-02-16791) and the State Science and Technology Program "Physics of Solid-State Nanostructures."

REFERENCES

1. M. H. Anderson, J. R. Ensher, M. R. Matthews, *et al.*, Science **269**, 198 (1995); D. S. Jin, J. R. Ensher, M. R. Matthews, *et al.*, Phys. Rev. Lett. **77**, 420 (1996); M. R. Andrews, M. O. Mewes, N. J. van Druten, *et al.*, Science **273**, 84 (1996).
2. S. A. Moskalenko, Fiz. Tverd. Tela (Leningrad) **4**, 276 (1962) [Sov. Phys. Solid State **4**, 199 (1962)]; I. M. Blatt,

K. W. Boer, and W. Brandt, Phys. Rev. **126**, 1691 (1962); R. S. Casella, J. Appl. Phys. **34**, 1703 (1963).
3. T. Fukuzawa, E. E. Mendez, and J. M. Hong, Phys. Rev. Lett. **64**, 3066 (1990).
4. J. E. Golub, K. Kash, J. P. Harbison, and L. T. Flores, Phys. Rev. B **41**, 8564 (1990).
5. L. V. Butov, A. Zrenner, G. A. Abstreiter, *et al.*, Phys. Rev. Lett. **73**, 304 (1994).
6. V. B. Timofeev, A. V. Larionov, A. S. Ioselevich, *et al.*, Pis'ma Zh. Éksp. Teor. Fiz. **67**, 580 (1998) [JETP Lett. **67**, 613 (1998)].
7. V. V. Krivolapchuk, E. S. Moskalenko, A. L. Zhmodikov, *et al.*, Solid State Commun. **111**, 49 (1999).
8. L. V. Butov, A. Imamoglu, A. V. Mintsev, *et al.*, Phys. Rev. B **59**, 1625 (1999).
9. A. V. Larionov, V. B. Timofeev, J. M. Hvam, and K. Soerenson, Zh. Éksp. Teor. Fiz. **117**, 1255 (2000) [JETP **90**, 1093 (2000)].
10. L. V. Butov, A. V. Mintsev, Yu. E. Lozovik, *et al.*, Phys. Rev. B **62**, 1548 (2000).
11. A. V. Larionov, V. B. Timofeev, J. M. Hvam, and K. Soerenson, Pis'ma Zh. Éksp. Teor. Fiz. **75**, 233 (2002) [JETP Lett. **75**, 200 (2002)].
12. D. Yoshioka and A. H. MacDonald, J. Phys. Soc. Jpn. **59**, 4211 (1990).
13. X. M. Chen and J. J. Quinn, Phys. Rev. Lett. **67**, 895 (1991).
14. Xuejun Zhu, P. L. Littlewood, M. S. Hybersten, and T. Rice, Phys. Rev. Lett. **74**, 1633 (1995).
15. J. Fernandez-Rossier and C. Tejedor, Phys. Rev. Lett. **78**, 4809 (1997).
16. Yu. E. Lozovik and O. L. Berman, Zh. Éksp. Teor. Fiz. **111**, 1879 (1997) [JETP **84**, 1027 (1997)].
17. Yu. E. Lozovik and I. V. Ovchinnikov, Pis'ma Zh. Éksp. Teor. Fiz. **74**, 318 (2001) [JETP Lett. **74**, 288 (2001)].
18. V. B. Timofeev, A. V. Larionov, M. Grassi Alessi, *et al.*, Phys. Rev. B **60**, 8897 (1999).
19. A. V. Larionov, V. B. Timofeev, P. A. Ni, *et al.*, Pis'ma Zh. Éksp. Teor. Fiz. **75**, 689 (2002) [JETP Lett. **75**, 570 (2002)].
20. S. W. Brown, T. A. Kennedy, D. Gammon, *et al.*, Phys. Rev. B **54**, R17339 (1996).
21. J. F. Jan and Y. C. Lee, Phys. Rev. B **58**, R1714 (1998).

Translated by E. Golyamina

JETP Letters, Vol. 76, No. 7, 2002, pp. 456–460. Translated from Pis'ma v Zhurnal Éksperimental'noĭ i Teoreticheskoĭ Fiziki, Vol. 76, No. 7, 2002, pp. 532–537.

Mechanism of Carbon Onion Transformation into Diamond-Like Structure

I. V. Ponomareva and L. A. Chernozatonskii*

Emanuel Institute of Biochemical Physics, Russian Academy of Sciences, ul. Kosygina 4, Moscow, 119991 Russia

** e-mail: cherno@sky.chph.ras.ru*

Received August 22, 2002; in final form, August 29, 2002

The formation of diamond-like structure in the carbon onion core was modeled by the molecular-dynamics method. The stages of this transformation (formation of holes in the fullerene shells and their healing accompanied by a decrease in the interlayer spacing in onion; accumulation of "free" atoms in the core and formation of new shells by these atoms; and core transformation under the action of these modified shells and temperature) adequately describe the main features of the Banhart and Ajayan observations. © *2002 MAIK "Nauka/Interperiodica".*

PACS numbers: 61.48.+c

The discovery of carbon onions—spherical carbon particles consisting of graphite-like shells (fullerenes)—is associated with the name of D. Ugarte. In experiments with the irradiation of nanoparticles filled with gold and lanthanide oxides, Ugarte discovered remarkable particles consisting of concentric perfectly shaped graphite shells. In his work [1], he was first to use the term "carbon onion" in the description of new particles. It was shown in the subsequent works [2–5] that the carbon onions can be prepared from a diversity of carbon materials, including nanodiamond [6]. The spacing between the onion shells corresponds to the interlayer spacing in graphite and comprises ~0.34 nm. One of the models treats the onion structure as a system of concentric fullerenes put into one another and having symmetry I_h with strictly fixed number N of atoms, where $N = 60b^2$ and b is the shell number [7]. The carbon onions are unstable and destroyed after irradiation [8]. In 1996, F. Banhart and P. Ajayan found that the intense irradiation of carbon onions by electron beam at a temperature of 700°C for one hour results in a diamond structure in the onion core [9–11]. These authors assumed that the pressures produced by the radiation and temperature inside the carbon onion exceed the graphite–diamond phase-transition pressure at these temperatures, giving rise to the diamond structure. However, they did not suggest any consistent mechanism that would be responsible for this transition. In [12], molecular dynamic modeling of the formation of sp^3 atoms in a carbon onion consisting of only two fullerene shells C_{60} and C_{240} was performed by the density functional method. The interspace between the shells of this onion and the space inside the C_{60} shell were saturated with carbon atoms. It was established that, to form a structure containing, on the average, 70% sp^3 atoms, nonequilibrium conditions must be created; namely, a considerable atomic inflow must occur from the outer shells to the core region of the onion (130 additional atoms) and the local temperature should be increased to 2100 K. However, this value exceeds by 2.5 times the experimental temperature.

In this work, the mechanism of carbon onion core transformation into a diamond-like structure (DLS) is suggested which adequately accounts for the main experimentally observed regularities of this transition.

According to the experiment, the following stages can be distinguished in the transformation of the core of carbon onion structure into diamond [9].

1. Under the action of radiation and temperature (650–750°C), the spacing between onion shells decreases with decreasing distance to the core. For example, in an onion comprising 15 shells, the interlayer separation changes from 0.33 to 0.22 nm for the shells with radii 12–1.3 nm, respectively.

2. The onion shells take on a more perfect spherical shape and, simultaneously, single-crystal or polycrystalline diamond structure arises in the core.

3. After the irradiated samples are cooled to room temperature, the core DLS remains stable, whereas the surrounding graphite-like structure contains many defects.

Below, the results of molecular dynamic modeling are presented for the transformation of carbon onion core into DLS. Classical molecular dynamic modeling amounts to solving the Newton equations, which were integrated in this work using the Verlet–Beeman scheme with an integration step of 0.35 fs. The total computational time was 140 to 530 fs, depending on the model chosen. The forces acting on atoms were calculated in various ways, depending on the distance between the interacting atoms.

0021-3640/02/7607-0456$22.00

The short-range chemical interactions ($r_{ij} < 0.2$ nm) were calculated using the empirical potential introduced by Brenner [13] for hydrocarbons in studying the growth dynamics of thin diamond films. According to this many-particle potential, the binding energy of two neighboring atoms is given by the expression

$$E_{ij}^b = V_{ij}^R - \bar{B}_{ij} V_{ij}^A, \quad (1)$$

where V_{ij}^R and V_{ij}^A are the repulsive and attractive exponential terms, respectively, and $\bar{B}_{ij}$ are the coefficients allowing for the many-particle interaction [13].

The long-range interaction was taken into account using the Lennard-Jones potential for the general hydrocarbon systems [14, 15]

$$V_{vdw} = \begin{cases} 0.0, \\ r_{ij} \le 0.2 \text{ nm}; \\ c_{3,k}(r_{ij} - r_k)^3 + c_{2,k}(r_{ij} - r_k)^2, \\ 0.2 \text{ nm} \le r_{ij} \le 32 \text{ nm}; \\ 4\varepsilon[(\sigma/r_{ij})^{12} - (\sigma/r_{ij})^6], \\ 0.2 \text{ nm} \le r_{ij} \le 0.32 \text{ nm}, \end{cases} \quad (2)$$

where $c_{n,k}$ are the spline coefficients and ε and σ are the parameters of van der Waals forces.

The combined expression for the total energy has the form

$$E_b = \sum_i \sum_{j<i} [V_{ij}^R - \bar{B}_{ij} V_{ij}^A + V_{vdw}]. \quad (3)$$

The forces were calculated analytically as the derivatives of the potential with respect to the radius-vector, and the temperature of the structure was specified by the mean particle velocity.

The $C_{60}@C_{240}@C_{540}@C_{960}$ onion was chosen as an initial model. We assume that the interlayer separation decreases because of the formation of hole vacancies in the fullerene structure as a result of atomic escape under the action of irradiation and temperature. This assumption is confirmed by the experimental fact that the amount of formed diamond increases substantially after replacing electron by the ion beam [10]. Inasmuch as the pentagon regions are most strained in the fullerene structure composed only of hexagons and pentagons [16], these regions are energetically least stable under the external actions. Based on this assumption, we removed in our model five atoms from each of the 12 pentagons of the C_{540} fullerene and five neighboring atoms for each pentagon, resulting in the C_{420} structure with holes. This structure is more spherical and contains unsaturated bonds. However, the unsaturated bonds are energetically unfavorable, so that these holes heal rather rapidly [16]. To determine the most probable way of filling the holes, the fact was taken into account that the onion shells become spherical and the separation between them decreases during the course of experiment. It is known that, to make fullerene more spherical, pairs of heptagons and pentagons should be present in its structure [17, 18]. Making use of the Stone–Waals transformations [16], we obtained the transformed pseudospherical smaller-diameter C_{420} fullerene containing 60 heptagons and 72 pentagons (Fig. 1a) from the C_{420} structure with holes. The atomization energies for the C_{540} fullerene, C_{420} fullerene with holes, and transformed C_{420} fullerene are, respectively, 3.93, 2.82, and 2.99 keV. The difference in the atomization energies for the fullerene with holes and C_{540} fullerene is –1.11 keV, whence it follows that the hole formation process is endothermic, while the required energy is delivered by the radiation source. The difference in the atomization energies of the fullerene with holes and the transformed C_{420} fullerene is evidence that, energetically, the structure with unsaturated bonds is less favorable.

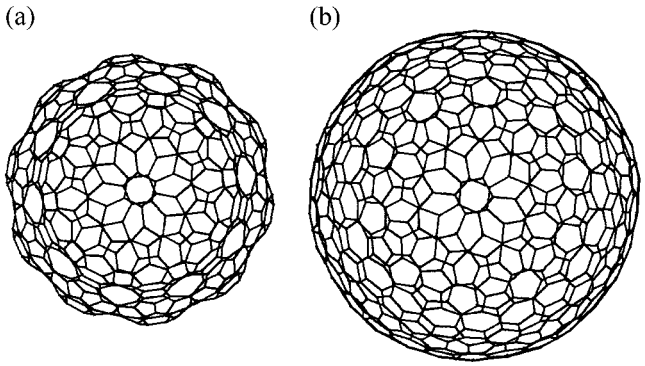

Fig. 1. Transformed fullerenes: (a) C_{420} fullerene (I_h symmetry) and (b) C_{600} fullerene (I_h symmetry).

Assuming that the irradiation effect is the strongest for the middle layers of a large onion [9], we obtained, in a similar manner, the transformed pseudospherical C_{600} fullerene containing 60 heptagons and 72 pentagons (Fig. 1b) from the C_{960} fullerene. The atomization energies for the C_{960} fullerene, C_{600} fullerene with holes, and transformed C_{600} fullerene are, respectively, 7.02, 3.87, and 4.32 keV. As in the case of the transformation of C_{540} into quasi-spherical C_{420} fullerene, the formation of holes in the C_{960} structure requires an energy source (e.g., ion or electron beam), while the quasi-spherical C_{600} fullerene is energetically more favorable than the fullerene with holes. Therefore, we obtained the transformed $C_{60}@C_{240}@C_{420}@C_{600}$ onion (model I) by removing 480 atoms (27% of the total number of atoms in the original structure) from the $C_{60}@C_{240}@C_{540}@C_{960}$ structure. Table 1 presents the interlayer distances for this model and the distances corresponding to the extrapolated experimental curve [9]. Both are in good agreement with each other.

Table 1. Interlayer spacing for the models and for the extrapolated experimental curve

Model	Shell	Intershell separation (in Å)	Intershell separation (in Å) corresponding to the extrapolated curve [9]
I	C_{60}–C_{240}	2.86	1.97
	C_{240}–C_{420}	2.49	2.09
	C_{420}–C_{600}	2.67	2.19
II	C'_{60}–C_{140}	1.95	1.85
	C_{140}–C_{240}	2.14	2.0
	C_{240}–C_{420}	2.31	2.10
	C_{420}–C_{600}	2.50	2.20
III	C_{60}–C_{140}	–	1.82
	C_{140}–C_{180}	–	1.95
	C_{180}–C_{240}	–	2.04
	C_{240}–C_{420}	1.98	2.13
	C_{420}–C_{600}	2.49	2.22

To cut the CPU time, the onion-like $C_{60}@C_{240}@C_{420}$ structure was used as a precursor (precursor **I'**) of the DLS, and the action on it from the outer shells was modeled by hydrostatic pressure with a magnitude calculated by the formula [19]

$$P_t = \left[\frac{2}{3}\frac{h}{R}\frac{1}{(S_{11}+S_{12})}\right]\frac{\Delta V}{V}, \quad (4)$$

where h = 3.4 Å is the interlayer spacing in graphite, $R = R(C_{420}) + 3.4$ (in Å) is the radius of outer shell for C_{420} in the unstrained structure, $\Delta V/V$ is the relative change in the fullerene volume as a result of changing radius from R to $R(C_{600})$ (Table 2), and S_{11} = 0.00098 GPa^{-1} and S_{12} = –0.00016 GPa^{-1} are the elements of the matrix of compliance coefficients for graphite [19].

Three computational runs were carried out in our study.

In the first run, precursor **I'** was heated under an external pressure (4) of 39 GPa (Table 2) to the temperature at which more than one-half (58%) of the total number of atoms became tetrahedrally coordinated. The corresponding temperature was 1450°C.

We assume that the structure with more than 50% (58%) of sp^3 atoms provides a good model for the DLS. We found that, if this structure is thermalized at the same temperature (1450°C) for a more prolonged time, the number of sp^3 atoms increases very slow. For instance, after the thermalization of precursor **I'** at a temperature of 1450°C for 353 ps, the number of sp^3 atoms increased only by 0.022%. At the same time, the thermalization, for the same time interval, of the same precursor at a temperature of 1100°C, at which 40% of atoms become tetrahedrally coordinated, reduces the number of sp^3 atoms by only 0.012%. Experiments show that, to form a diamond crystal in the carbon onion core, the carbon onions should be irradiated for 1 h [9]. Thus, the time it takes for the formation of diamond crystal structure exceeds the time accessible in our computations by ten orders of magnitude, which casts doubt on the possibility of its computer modeling with the presently available computational resources.

With our assumptions about the DLS, by the transition temperature T_t below will be meant the temperature at which more than one-half of the sp^3 atoms in the precursor become tetrahedrally coordinated. In this way, the T_t value in the first computational run was found to be 1450°C (Table 3), which is approximately twice its experimental temperature [9]. Besides, the separation between the C_{60} and C_{240} fullerenes in model **I** did not conform to a monotonic decrease in the interlayer spacing with decreasing distance from the core center [9].

To improve the model, the fact was taken into account that a certain fraction of the atoms removed from the initial $C_{60}@C_{240}@C_{540}@C_{960}$ onion (the total number of these atoms in model **I** was equal to 480) remains inside the onion structure. In principle, these atoms can both occupy arbitrary positions without organizing ordered structure [12] and form new fullerene shells. It turned out that the formation of a new fullerene molecule was energetically more favorable. For example, the specific strain energy for the $C'_{60}@C_{140}@C_{240}@C_{420}@C_{600}$ onion (model **II**; Fig. 2) is 0.63 eV/atom, whereas the specific strain energy of the structure consisting of the $C_{60}@C_{240}@C_{420}@C_{600}$ onion and 140 atoms occupying arbitrary positions between the shells and in the onion core was found to be 0.94 eV/atom.

Table 2. Radii of fullerene shells and hydrostatic pressures for different models

Model	I				II					III					
Shell	C_{60}	C_{240}	C_{420}	C_{600}	C'_{60}	C_{140}	C_{240}	C_{420}	C_{600}	C_{60}	C_{140}	C_{180}	C_{240}	C_{420}	C_{600}
Radius, Å	3.64	6.50	8.99	11.66	3.00	4.95	7.09	9.40	11.90	–			7.99	9.97	12.46
Pressure, GPa	39.4				45.6					42.2					

Table 3. Characteristics of the transformation of model structures into DLS

Model	Number of atoms removed from the $C_{60}C_{240}C_{540}C_{960}$ structure (%)	T_t (°C)	Number of sp^3 atoms at T_t (%)	Number of sp^3 atoms at T = 300 K (%)
$C_{60}C_{240}C_{420}$	27	1450	58	46
$C'_{60}C_{140}C_{240}C_{420}$	19	700	62	54
$C_{60}C_{140}C_{180}C_{240}C_{420}$	9	350	74	64

On this basis, we used model **II** in the second computational run. This model corresponds to the situation where 30% of atoms removed initially from the original $C_{60}@C_{240}@C_{540}@C_{960}$ structure remain inside the $C_{60}@C_{240}@C_{420}@C_{600}$ onion. They form new fullerene shell C_{140} and exert pressure on C_{60}, so that the optimized C_{60} fullerene transforms into the C'_{60} cluster containing 50 sp^3 atoms (Fig. 2). One can see from Table 1 that this model fits the extrapolated experimental curve [9] well: the interlayer spacing tends to monotonically decrease with decreasing distance from the onion center. Because of this, the $C'_{60}@C_{140}@C_{240}@C_{420}$ structure (precursor **II'**) was chosen as a precursor of DLS in this computational run. The pressure exerting on it by the C_{600} shell is given in Table 2. We heated precursor **II'**. The transition temperature at which 465 of 600 atoms became sp^3-coordinated was found to be 700°C (Table 3). This value agrees well with the experimentally observed temperatures of the carbon onion core transformation into diamond [9].

To determine whether model **II** is optimal, performed the third computational run. In this run, an even larger number (67%) of atoms removed from the original $C_{60}@C_{240}@C_{540}@C_{960}$ onion were retained in the inner shells, and it was assumed that these atoms can form two new fullerene shells C_{140} and C_{180}. Hence, a highly strained $C_{60}@C_{140}@C_{180}@C_{240}@C_{420}@C_{600}$ structure (model **III**) was taken as a model in this computational run. Its inner shells C_{60}, C_{140}, and C_{180} form structure with a quantity of diamond-like bonds even at normal conditions. The $C_{60}@C_{140}@C_{180}@C_{240}@C_{420}$ structure (precursor **III'**) was a precursor in this run. The temperature for the modeled transition was found to be 350°C. This value is half as high as the experimentally observed value [9].

Analyzing the obtained results, we can conclude that model **II** is optimal for the comparison with the experiment (Table 3). In this model, about 30% of the atoms removed from the original $C_{60}@C_{240}@C_{540}@C_{960}$ onion remain in the region between the layers of the transformed onion structure $C_{60}@C_{240}@C_{420}@C_{600}$ and form new fullerene shell C_{140}. On the whole, 320 atoms are removed to the outer shells (about 20% of the total number of atoms in the original $C_{60}@C_{240}@C_{540}@C_{960}$ onion). Model **II** also agrees with the extrapolated experimental curve for interlayer distances.

All DLSs obtained in the three computational runs were cooled to room temperature (T = 300 K) after heating to T_t. Since the number of sp^3 atoms changed only slightly in this case (Table 3), the DLS obtained in model **II** can be considered stable.

Therefore, we suggest the following mechanism for the transformation of carbon onion core into DLS.

I. The most strained regions in the onion fullerene shells are destroyed under the action of radiation and temperature. As a result, holes appear in the shells. Hole healing leads to a decrease in the fullerene surface and, as a result, in the interlayer spacing in the onion.

II. Nearly 70% of "free" atoms arisen in the core structure after the hole formation leave their "parent" shells and move into the other outer and inner shells. The total number of atoms migrating beyond this parent region is equal to about 20% of the number of core atoms. It is most likely that they are accumulated near

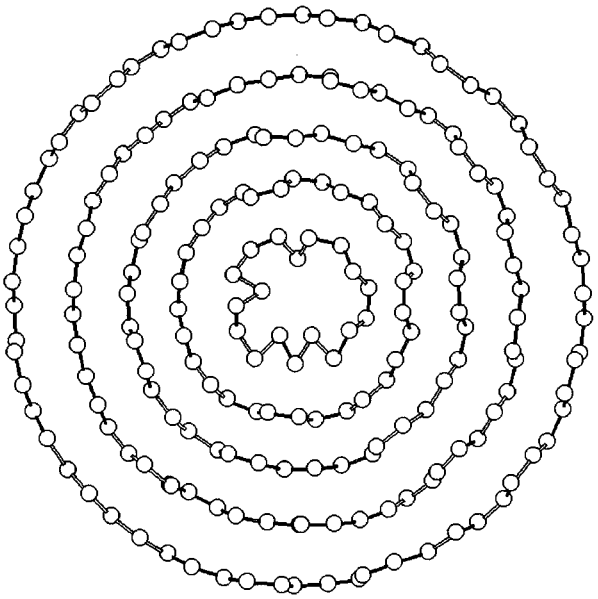

Fig. 2. Cross cut of a strained onion structure $C'_{60}@C_{140}@C_{240}@C_{420}@C_{600}$ (model **II**).

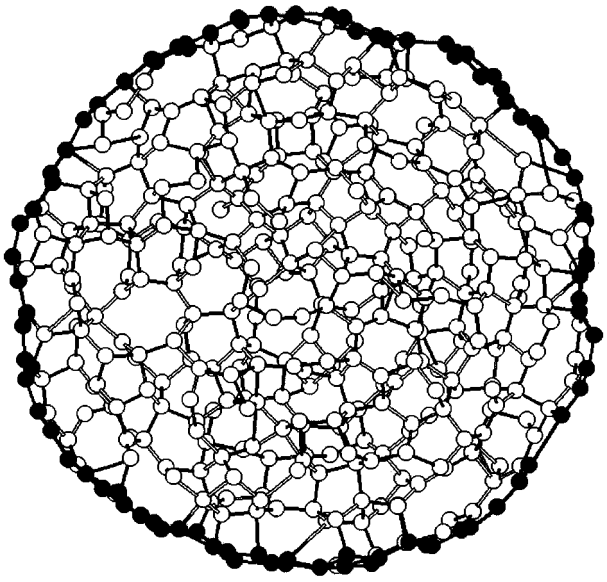

Fig. 3. Cross cut of a diamond-like structure cooled to T = 300 K (initial structure C'_{60} @C_{140}@C_{240}@C_{420}@C_{600}).

the surface of the transformed onion to form new shells. This effect can be used to explain the fact that, despite the increase in the core density as a result of formation of the sp^3 structure, no appreciable decrease in the onion size is observed [9–11]. The atoms remaining in the parent region form new fullerene shells, also leading to a decrease in the interlayer spacing.

III. Because of a decrease in the interlayer spacing, the onion shells act as "microscopic pressure chambers," in which the DLS appears upon rising temperature to 700°C (Fig. 3). In Fig. 3, the contour of the DLS surface replicates the typical contour of a heavily defective structure of graphite shells in the photographs of room-temperature-cooled onions with a diamond core [9].

Let us compare the mechanism suggested in this work with the experimentally observed regularities of the carbon onion core transition into diamond. Items I–II of our mechanism are in compliance with the experimental stage I, which was mentioned at the beginning of this work. Item III describes the second experimental regularity. The third experimental stage corroborates our conclusion that the resulting DLS structures are stable after cooling to room temperature (Table 3).

Note that the transformation of carbon onions into diamond is of great commercial interest [20, 21]. The point is that the presently available methods of producing diamond from graphite require very high pressures and the presence of catalysts. For example, the formation of diamond from C_{60} fullerenes necessitates a nonhydrostatic pressure on the order of 20 GPa [22]. As to the transformation of carbon onion core into diamond, it is a direct transition from graphite to diamond. For this reason, apart from the theoretical interest in the understanding of the mechanism of this transition, its explanation is topical from the applied point of view. The mechanism suggested in this work account for the main experimentally observed regularities of the transition of carbon onion core into diamond.

We are grateful to G.A. Vinogradov, I.V. Stankevich, and M. Menon for discussion and valuable remarks. This work was supported by INTAS (grant no. 00-237) and the State Scientific and Technical Program "Topical Directions in Condensed Matter Physics."

REFERENCES

1. D. Ugarte, Nature **359**, 707 (1992).
2. P. J. F. Harris, S. C. Tsang, J. B. Claridge, and M. L. H. Green, J. Chem. Soc., Faraday Trans. **90**, 1799 (1994).
3. M. S. Zwanger, F. Banhart, and A. Seeger, J. Cryst. Growth **163**, 445 (1996).
4. T. Fuller and F. Banhart, Chem. Phys. Lett. **254**, 372 (1996).
5. V. Z. Mordkovich, A. G. Umnov, T. Inoshota, and M. Endo, Carbon **37**, 1855 (1999).
6. V. Kuznetsov, A. L. Chuvilin, E. M. Moroz, *et al.*, Chem. Phys. Lett. **222**, 343 (1994).
7. H. W. Kroto, Nature **359**, 670 (1992).
8. G. Lulli, A. Parisani, and G. Mattei, Ultramicroscopy **60**, 187 (1995).
9. F. Banhart and P. M. Ajayan, Nature **382**, 433 (1996).
10. M. Zaiser and F. Banhart, Phys. Rev. Lett. **79**, 3680 (1997).
11. P. Wesolowskii, Y. Lyutovich, F. Banhart, *et al.*, Appl. Phys. Lett. **71**, 1948 (1997).
12. R. Astala, M. Kaukonen, and R. M. Nieminer, Phys. Rev. B **63**, 081402 (2001).
13. D. W. Brenner, Phys. Rev. B **42**, 9458 (1990).
14. S. B. Sinott, O. A. Shenderova, C. T. White, and D. W. Brenner, Carbon **36**, 1 (1998).
15. Z. Mao, A. Garg, and S. B. Sinott, Nanotechnology **10**, 273 (1999).
16. H. Terrones and M. Terrones, J. Phys. Chem. Solids **55**, 1789 (1997).
17. H. Terrones, M. Terrones, and W. K. Hsu, Chem. Soc. Rev. **24**, 341 (1995).
18. K. R. Bates and G. E. Scureia, Theor. Chem. Acc. **99**, 29 (1998).
19. R. S. Ruoff, Nature **350**, 663 (1991).
20. R. Clarke and C. Uher, Adv. Phys. **33**, 469 (1984).
21. J. C. Angus and C. C. Hayman, Science **241**, 913 (1988).
22. M. N. Reguerio, P. Monceau, and J. L. Hodeau, Nature **355**, 237 (1992).

Translated by V. Sakun

JETP Letters, Vol. 76, No. 7, 2002, pp. 461–464. From Pis'ma v Zhurnal Éksperimental'noĭ i Teoreticheskoĭ Fiziki, Vol. 76, No. 7, 2002, pp. 538–541.

Ultrafast Laser-Induced Phase Transitions in Tellurium¶

S. I. Ashitkov[1], M. B. Agranat[1, *], P. S. Kondratenko[1], S. I. Anisimov[1], V. E. Fortov[1], V. V. Temnov[2, 3], K. Sokolowski-Tinten[3], B. Rethfeld[3], P. Zhou[3], and D. von der Linde[3]

[1] *High Energy Density Research Center, Joint Institute for High Temperatures, Russian Academy of Sciences, ul. Izhorskaya 13/19, Moscow, 127412 Russia*

**e-mail: utpr@iht.mpei.ac.ru*

[2] *Institute of Applied Physics, Russian Academy of Sciences, ul. Ul'yanova 46, Nizhni Novgorod, 603600 Russia*

[3] *Institute for Laser and Plasma Physics, University of Essen, 45117 Essen, Germany*

Received September 2, 2002

We present experimental investigations of ultrafast phase transitions in tellurium following excitation by an intense femtosecond laser pulse. Femtosecond time-resolved polarization-sensitive microscopy is used to monitor the temporal evolution of optical anisotropy (birefringence) of the irradiated material. The decay of optical anisotropy associated with the loss of order in crystalline tellurium is fluence-dependent and occurs within 0.5–3 ps. © *2002 MAIK "Nauka/Interperiodica".*

PACS numbers: 64.70.Kb; 61.80.Ba; 78.20.Fm

Ultrafast laser processing of materials, especially metals and semiconductors, is a field of condensed-matter physics and material science that has developed rapidly over the last few years. It has proved to be of considerable interest for both applied and fundamental research for a variety of reasons, which are discussed extensively in the literature. An important application of ultrashort laser pulses is connected with the study of ultrafast phase transitions. In our previous work [1], we experimentally studied ultrafast changes of order of monocrystalline graphite under irradiation by a femtosecond laser pulse using a new experimental technique that exploits the optical anisotropy of the crystal.

In this letter, we present the results of a similar study performed on samples of monocrystalline tellurium. The experiments were performed with a chirped-pulse-amplified Ti:sapphire laser system (100-fs pulse duration), using time-resolved polarization-sensitive optical microscopy [1]. The sample surface is excited by an intense *s*-polarized pump laser pulse at 800 nm (angle of incidence 45°) and probed by a weak time-delayed *p*-polarized probe laser pulse at 400 nm (normal incidence). Snapshots of the laser-excited surface are recorded by a digital CCD-camera. Further details of the technique can be found in [1].

The (100) surface of monocrystalline tellurium contains the optical anisotropy axis. Rotating the sample around the surface normal allows variation of the angle φ between the anisotropy axis and the polarization vector of the probe pulse. In this way, the ordinary reflectivity R_o (φ = 90°), extraordinary reflectivity R_e (φ = 0°), as well as the so-called "anisotropic" reflectivity component R_{cr} (φ = 45°) [1], can be measured:

$$R_o = \left|\frac{n_o - 1}{n_o + 1}\right|^2, \quad R_e = \left|\frac{n_e - 1}{n_e + 1}\right|^2, \quad R_{cr} \approx \frac{|2\delta|^2}{|n + 1|^4},$$

where n_o and n_e are the complex refractive indices for ordinary and extraordinary polarization; $\delta = (n_e - n_o)/2$, and $n = (n_e + n_o)/2$.

The complex indices of refraction for unexcited tellurium are as follows [2]: for the pump (λ = 800 nm), $n_o = 5.84 - 1.06i$, $n_e = 6.73 - 2.89i$; for the probe (λ = 400 nm), $n_o = 2.37 - 3.29i$, $n_e = 2.22 - 3.96i$. The skin depths ($\mu = \lambda/4\pi \mathrm{Im}\, n$) are $\mu_o = 60$ nm, $\mu_e = 22$ nm for the pump and $\mu_o = 10$ nm, $\mu_e = 8$ nm for the probe. Thus, the skin depth at the probe wavelength is always less than the skin-depth of the pump pulse.

In Fig. 1a, snapshots of the transient changes of the anisotropic reflectivity in the laser-irradiated area are presented. Corresponding spatial cross sections, representing the fluence dependence of the "anisotropic" reflectivity component at a given time instant, are depicted in Fig. 1b. From Fig. 1b, it can be seen that during the first few picoseconds, the intensity of the "anisotropic" reflectivity component drops drastically in the center of the focal spot (maximum fluence) indicating a corresponding loss of the optical anisotropy, which is interpreted as a loss of crystalline order [1] m the excited surface layer. The threshold fluence with respect to the change of anisotropic reflection is about $F \approx 15$ mJ/cm^2 (a study of melting near the threshold fluence is the subject of our future research, as it demands modernization of an experimental technique).

¶This article was submitted by the authors in English.

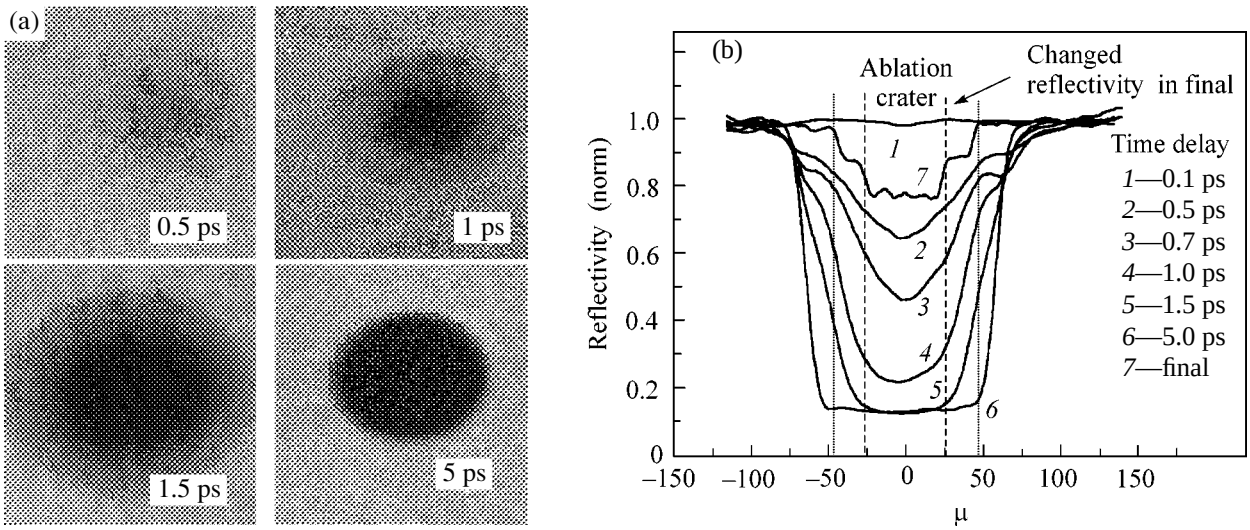

Fig. 1. (a) Transient snapshots and (b) profiles of the "anisotropic" reflectivity R_{cr} of the excited Te surface for different pump–probe time delays for a pump peak fluence of 66 mJ/cm^2.

The recovery of the anisotropic reflectivity back to nearly the initial value indicates crystallization upon resolidification. This process is much slower and takes a few nanoseconds.

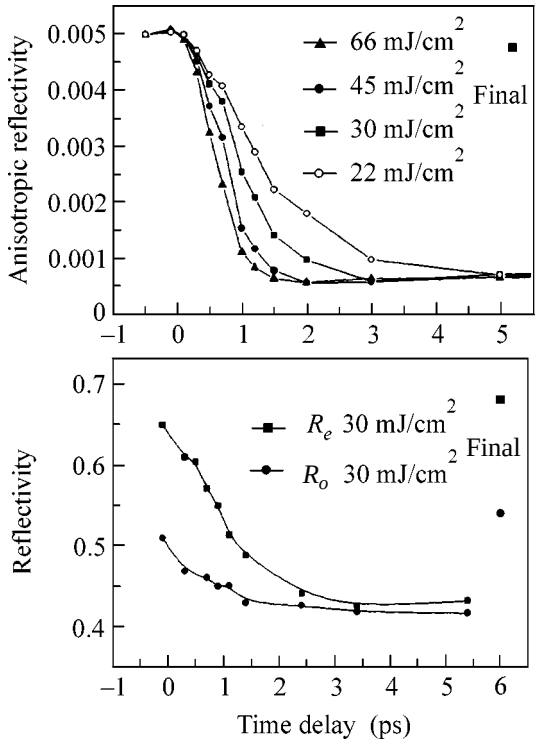

Fig. 2. Temporal evolution of the (a) "anisotropic" and (b) ordinary (R_o) and extraordinary (R_e) reflectivity components for different laser fluences above the melting threshold.

Figure 2 shows the temporal evolution of the ordinary, extraordinary, and "anisotropic" reflectivities for different excitation fluences above the melting threshold. It is clear that the decay time of the "anisotropic" reflectivity component coincides with the time at which the ordinary and extraordinary reflectivities become equal. Within a few picoseconds, the optical anisotropy for the presented fluences disappears, whereas the isotropic reflectivity reaches a constant value. We interpret the observed rapid loss of optical anisotropy and the existence of a stationary isotropic reflectivity at later times as due to the formation of a liquid surface layer with a thickness larger than the penetration depth of the probe pulse. Thus the decay time of the optical anisotropy may be referred to as the *melting time*.

Figure 2a shows the temporal evolution of the anisotropic reflectivity component for different laser fluences and aims to demonstrate the pronounced dependence of the *melting time* on the incident laser fluence. The melting time derived by a simple exponential fit of the measured time dependences in Fig. 2a is plotted in Fig. 3 as a function of the laser fluence. For laser fluences above 45 mJ/cm^2, which is approximately three times the melting threshold, the melting process occurs essentially in less than one picosecond. For laser fluences closer to the melting threshold, the melting time increases up to a few picoseconds.

In order to provide a physical interpretation of the results of our optical measurements, we have analyzed the optical properties of a thin film of liquid tellurium on a crystalline tellurium substrate. The optical constants of liquid tellurium were determined by means of time-resolved interferometry [3]. This technique allows for femtosecond time-resolved measurements of changes (relative to unexcited tellurium) in both the amplitude and the phase of the reflected probe light. We

have performed interferometric measurements for sufficiently high fluences at long delay times up to a few nanoseconds to assure that the laser-melted layer of liquid tellurium has a thickness larger than the skin depth of the probe. Taking the optical constants of crystalline tellurium at $\lambda = 400$ nm as reference values and using the Fresnel formulas, we determine the complex index of refraction for liquid Te at our probe wavelength as $n_{\text{liquid Te}} = 2.6 - 2.1i$. The reflectivities obtained with the measured optical constants for liquid Te are in good agreement with previously reported results [4]. It is important to note that at $\lambda = 400$ nm, the skin-depth in the melt ($\mu_{\text{liquid Te}} = 15$ nm) is larger than in the crystalline solid ($\mu_o = 10$ nm, $\mu_e = 8$ nm) but still less than the skin depth in the solid for the pump.

Let us discuss now the physical mechanisms of melting that operate in tellurium. More precisely, we wish to distinguish between three different possible melting pathways: nonthermal melting, bulk thermal melting via homogenous nucleation, and heterogeneous thermal melting. Nonthermal melting describes a transition to the liquid phase which is driven by an electronically induced instability of the lattice upon excitation of sufficiently dense electron–hole plasma [5] and which has been extensively studied in covalently bonded semiconductors. This kind of melting can be extremely fast (100-fs time scale), because it does not require heating of the lattice prior to the phase transition.

The borderline between thermal and nonthermal processes is determined by the time needed for the energy transfer from the primarily excited electronic system to the lattice. This time can be estimated using the two-temperature model [6, 7]. For femtosecond laser excitation, the characteristic time of temperature equilibration is $\tau = c_e c_i/\alpha(c_e + c_i)$ [8], where c_e and c_i are the heat capacities of the electrons and lattice, respectively, and a is the electron–phonon coupling constant. In tellurium, the heat capacity of the electrons is very small [9], thus the characteristic time for lattice heating is approximately given by $\tau \approx (c_e/\alpha)$. If typical values for α in metals are applied (unfortunately, α is not known for the specific case of tellurium) thermalization times of 1 ps or less are derived. Therefore, for the largest pump fluences studied in this work ($F > 45$ mJ/cm^2), the observed melting time is comparable to the characteristic time of lattice heating, and it is not possible to distinguish between non-thermal and thermal melting processes.

However, for lower fluences, melting needs longer times (>1 ps) and can be regarded as thermal in nature. Usually it is assumed that melting occurs *heterogeneously* starting at the surface where no nucleation barrier exists and proceeds into the bulk with a velocity ultimately limited by the speed of sound. It follows from the above analysis of the optical constants that the observation of stationary isotropic optical properties requires a liquid layer with a thickness of at least

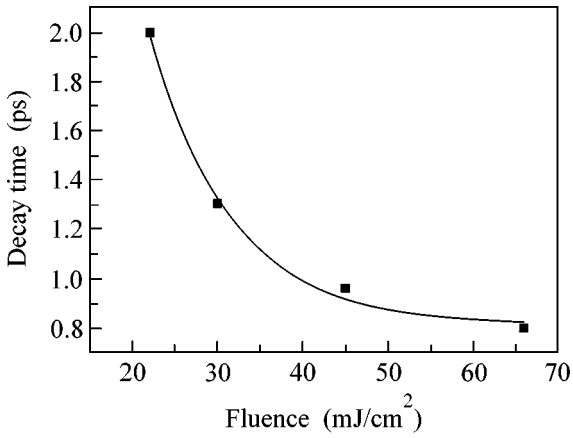

Fig. 3. Melting time as a function of laser fluence (see text for details).

15 nm. The sound velocity in solid tellurium is about $c_s \approx 2000$ m/s [9], which sets a lower limit for the time of heterogeneous melting of about 7–10 ps. Therefore, for the fluence range presented in this work, heterogeneous melting can be excluded, although it may occur for fluences very close to the melting threshold.

In order to explain melting times of just a few picoseconds, which are observed in this work, we invoke the model of thermal melting via *homogenous* nucleation [10]. This model describes the formation of liquid nuclei in the bulk of an overheated solid, i.e., after the hot laser-excited electrons have thermalized with the initially cold lattice via electron–phonon coupling. We would like to stress that the formation of liquid nuclei inside the bulk is generally less probable than the formation of a liquid layer at the free surface. However, under strong superheating, the melting over the skin-depth by homogeneous nucleation can in fact be faster than the melting due to the propagation of a solid–liquid interface from the surface into the bulk of the material. In particular, it was shown recently [10] that for high superheating, corresponding to excitation fluences sufficiently above the melting threshold, the melting time by thermal homogeneous nucleation is essentially limited by the time needed for energy thermalization.

In summary, we have applied ultrafast time-resolved optical anisotropy measurements to study structural transitions in femtosecond laser-excited mono-crystalline tellurium. The presented data indicate that in this material, melting may occur by thermal, homogeneous nucleation.

We thank S.V. Petrov from ITP RAS for tellurium samples. This work was supported by the NATO Grant SA(PST.CLG no. 975059) and the Forschungspool of the University of Essen (V.T.).

REFERENCES

1. S. I. Ashitkov, M. B. Agranat, P. S. Kondratenko, *et al.*, Pis'ma Zh. Éksp. Teor. Fiz. **75**, 96 (2002) [JETP Lett. **75**, 87 (2002)].
2. *Handbook of Optical Constants of Solids*, Ed. by E. D. Palik (Academic, Orlando, 1985).
3. V. V. Temnov, K. Sokolowski-Tinten, and D. von der Linde, to be published.
4. L. A. Silva and M. Cutler, Phys. Rev. B **42**, 7103 (1990).
5. J. A. van Vechten, R. Tsu, and F. W. Saris, Phys. Lett. A **74A**, 422 (1979).
6. S. I. Anisimov, B. L. Kapeliovich, and T. L. Perel'man, Zh. Éksp. Teor. Fiz. **66**, 776 (1974) [Sov. Phys. JETP **39**, 375 (1974)].
7. B. Rethfeld, A. Kaiser, M. Vicanek, and G. Simon, Phys. Rev. B **65**, 214303 (2002).
8. J. J. Klossika, U. Gratzke, M. Vicanek, and G. Simon, Phys. Rev. B **54**, 10277 (1996).
9. *Handbook of Physical Quantities*, Ed. by I. S. Grigoriev and E. Z. Meilikhov (Énergoatomizdat, Moscow, 1991; CRC Press, Boca Raton, 1997).
10. B. Rethfeld, K. Sokolowski-Tinten, D. von der Linde, and S. I. Anisimov, Phys. Rev. B **65**, 092103 (2002).

JETP Letters, Vol. 76, No. 7, 2002, pp. 465–468. Translated from Pis'ma v Zhurnal Éksperimental'noĭ i Teoreticheskoĭ Fiziki, Vol. 76, No. 7, 2002, pp. 542–546.

Electron–Hole Recombination Confinement in Self-Organized AgBr Nanocrystals in a Crystalline KBr Matrix

P. G. Baranov, N. G. Romanov*, V. L. Preobrazhenskiĭ, and V. A. Khramtsov

Ioffe Physicotechnical Institute, Russian Academy of Sciences, St. Petersburg, 194021 Russia

**e-mail: Nikolai.Romamov@mail.ioffe.ru*

Received September 3, 2002

The phenomenon of spatial confinement of the electron–hole recombination in exchange-coupled donor–acceptor pairs was observed by optically detected magnetic resonance in AgBr nanocrystals formed as a result of the self-organized growth in an ionic KBr crystal matrix. The effect is manifested by the maximum distance between recombining donors and acceptors being restricted to the nanocrystal size and by a change in the g value of shallow electron donor centers. Based on an analysis of the exchange interactions, the distribution of distances in the donor–acceptor pairs is determined and the dimensions of nanocrystals are estimated. © *2002 MAIK "Nauka/Interperiodica"*.

PACS numbers: 71.35.Ee; 73.22.–f; 61.46.+w

The phenomenon of spatial confinement of charge carriers is a characteristic feature of low-dimensional semiconductor systems. Self-organized growth of the low-dimensional structures such as quantum dots and nanocrystals is a promising technological process [1]. Silver halides AgCl and AgBr are indirect-bandgap semiconductors possessing unique properties (in particular, the latent image formation), which are widely used in photography [2]. The oriented nanocrystals of silver halides formed as a result of the self-organized growth in the matrix of ionic alkali halide crystals [3–5] are convenient model objects for investigation of the spatial confinement effects by microwave spectroscopy, since the electron and hole centers, as well as localized excitons in the bulk crystals of AgCl and AgBr, have been investigated in much detail [2, 6, 7]. It was of special interest to study the recombination of electron–hole pairs and excitons in such model structures.

Here, we report on the recombination luminescence from self-organized micro- and nanocrystals of AgBr in a KBr crystal matrix studied for the first time by the method of optically detected magnetic resonance (ODMR). It was found that the ODMR spectra of the AgBr nanocrystals are significantly different from the spectra of bulk AgBr crystals, the distinctions being related to the spatial confinement of the electron–hole recombination in the case of nanocrystals.

The crystals of AgBr and KBr:AgBr (2 mol % AgBr in KBr melt) were grown using the Stockbarger technique. The latter samples were synthesized using AgBr single crystals as the dopant material. The micro and nanocrystals of AgBr formed in the KBr matrix as a result of the self-organized growth. The photoluminescence (PL) was excited by UV light from a deuterium lamp and measured with the aid of a monochromator. The microwave (35 GHz) power supplied to a sample was modulated at a frequency of 80–10000 Hz, after which the microwave-induced changes in the PL intensity were monitored by a lock-in amplifier.

Figure 1 presents the PL (a) and ODMR (b) spectra measured using a bulk AgBr crystal sample (curves *1*) and two KBr:AgBr samples (curves *2* and *3*) cleaved

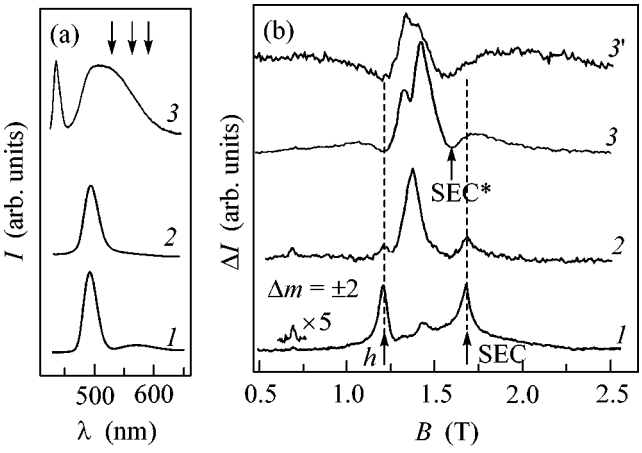

Fig. 1. The (a) PL and (b) ODMR spectra of (*1*) a bulk AgBr crystal and (*2*, *3*) two KBr:AgBr samples cleaved from different parts of the KBr:AgBr boule grown from a KBr melt containing 2 mol % AgBr. T = 1.7 K. The ODMR spectra were measured at ν = 35.2 GHz, P = 400 mW, f_{mod} = 85 (*3*) and 1500 Hz (*3*'), and $B \parallel [001]$; λ = 587 nm. The arrows at curve *3* in (a) indicate the emission wavelengths used to measure the ODMR spectra presented in Fig. 2a; the arrows in (b) indicate the positions of lines corresponding to the localized holes (*h*) and shallow electron centers (SEC and SEC*) in the bulk AgBr and in AgBr nanocrystals, respectively.

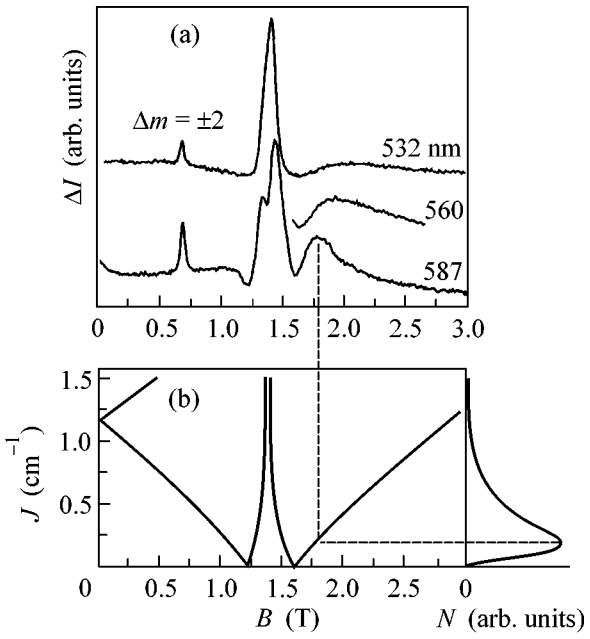

Fig. 2. (a) The ODMR spectra of KBr:AgBr sample 3 measured at λ = 587, 560, and 532 nm; (b) the resonance fields B corresponding to the EPR transitions at 35 GHz for a pair of recombining centers with spins 1/2, g values of 2.08 and 1.57, and various exchange interaction constants J; the right-hand curve shows the number N of the recombining donor–acceptor pairs as the function of J, calculated using the ODMR spectrum measured at 587 nm.

from different parts of the KBr:AgBr boule (the curve number corresponds to a sample number). The ODMR spectra of sample 3 presented in Fig. 1 were measured using a microwave power modulated at 85 and 1500 Hz (curves *3* and *3*', respectively).

As can be seen, both the PL and ODMR spectra of KBr:AgBr sample 2 (curves *2*) are close to the corresponding spectra of the bulk AgBr crystal (curves *1*). The optical emission spectra contain a band with the maximum at 580 nm, assigned to the donor–acceptor (D–A) recombination, and a more intense peak at 500 nm related to the residual (a few ppm) iodine impurity in AgBr. The ODMR spectrum detected using the 580 nm emission band displays the signals (indicated by arrows in Fig. 1b) due to localized holes (h) with g = 2.08 and shallow electron centers (SEC) with g = 1.49, corresponding to the recombination of distant D–A pairs. The ODMR lines in the central part of the spectrum are assigned to triplet excitons [2]. The triplet nature of these lines is confirmed by the presence of a peak due to the forbidden transition with $\Delta m = \pm 2$. The similarity of the PL and ODMR spectra observed in KBr:AgBr sample 2 and the bulk AgBr crystal indicates that rather large microcrystals of a silver halide (AgBr) retaining properties of the bulk material can form as a result of the self-organized growth process in KBr:AgBr (as well as in the KCl:AgCl system studied previously [4, 5]).

The PL and ODMR spectra obtained from KBr:AgBr sample 3 significantly differ from those observed in samples 1 and 2 considered above. The luminescence spectrum of sample 3 exhibits an intense exciton band in the region of 440 nm, which is analogous to that observed in the PL spectrum of AgBr nanocrystals in gelatin and glass matrices [2, 8, 9]. This fact indicates that AgBr nanocrystals with dimensions on the order of 6 nm are present in the KBr crystal matrix. In addition, the ODMR spectra *3* and *3*' (Fig. 1b) show broad asymmetric bands at low and high fields and two more intense peaks in the central part. The shape of the ODMR spectrum significantly changes in response to increase in the chopping frequency: the separation of maxima of the broad signals in low and high fields increases, while the distance between central ODMR peaks decreases.

A similar behavior is observed on decreasing the luminescence wavelength at which the ODMR signal is detected. Figure 2a shows the ODMR spectra measured in sample 3 using the emission at 532, 560, and 587 nm (indicated by arrows at curve *3* in Fig. 1a). These spectra were measured using a chopping frequency of 85 Hz and increased microwave power (400 mW). Similarly to the case of increasing chopping frequency, a reduction in the detection wavelength leads to a decrease in separation of the ODMR peaks in the central part of the spectrum and to an increase in the distance between broad signals in the low and high fields. The minima of the ODMR signals are observed in magnetic fields corresponding to the g value of localized holes in AgBr and g = 1.57, which is different from the g value of shallow electron centers in the bulk AgBr.

The energy levels of a D–A pair in a magnetic field B can be described using a spin Hamiltonian

$$H = g^e \mu_B \mathbf{S}^e \mathbf{B} + g^h \mu_B \mathbf{S}^h \mathbf{B} + J \mathbf{S}^e \mathbf{S}^h, \qquad (1)$$

where $S^e = S^h = 1/2$. Here, the first two terms describe the interaction of electron (on the donor) and hole (on the acceptor) with the magnetic field, while the third term describes the isotropic exchange interaction. In AgBr, the g values of donors and acceptors are isotropic. The positions (resonance fields) of the EPR transitions at a microwave frequency of 35 GHz, calculated by Eq. (1) for g^h = 2.07, g^e = 1.57 and various exchange interaction constants J, are presented in Fig. 2b in the same scale of fields as that used in Fig. 2a for the ODMR spectra. The calculations were performed using the "R-Spectrum" program written by Grachev [10].

For distant D–A pairs, in which the spacing ρ between donor and acceptor is large compared to the sum of their Bohr radii, the exchange interaction is weak. The ODMR spectrum of such a system must display two lines corresponding to the EPR of isolated donors and acceptors, as it is actually observed in the spectra of bulk AgBr and AgBr microcrystals in KBr. A decrease in the distance ρ gives rise to the exchange interaction J which leads to splitting of the energy lev-

els of the D–A pair in a zero field and to splitting of the ODMR signals. In the ODMR spectrum, four lines correspond to each J value, whose positions vary with J as depicted in Fig. 2b. When the L value exceeds that for the Zeeman interaction, the D–A pair states split in a zero field can be described by the total spin $S = 0$ (singlet) and $S = 1$ (triplet). The corresponding ODMR spectrum must contain two lines, whose splitting, due to nonlinearity of the levels $S = 0$ and $S = 1$, $m_S = 0$, must tend to zero with increasing J. In contrast to the case of AgCl, the ODMR spectra of the triplet excitons in AgBr ($J = -1.9$ cm^{-1}) are isotropic and exhibit no splitting of the fine structure. Both the bulk crystals and the microcrystals of AgBr contain coexisting systems of the D–A pairs and the excitons with a fixed exchange splitting.

The exchange interaction depends on overlap of the wave functions of electrons and holes. When the Bohr radius of the donor is much greater than that of the acceptor ($a_D \gg a_A$), the exchange interaction constant exponentially depends on the D–A distance [11]: $J = J_0\exp(-2\rho/a_D)$, where J_0 is the limiting exchange interaction value. A similar exponential relation describes the rate of radiative recombination in the pair [12]: the emission due to the recombination of closer pairs is characterized by a higher recombination rate. This approach is applicable to AgBr crystals, since shallow electron centers are characterized by a hydrogenlike 1s wave function with a large Bohr radius $a_D = 1.7$ nm [6], while the wave function of a hole center is considered as localized.

In the presence of a Coulomb interaction, the emission wavelength decreases with increasing distance between the recombining centers [13]. It should be noted that a strong electron–phonon interaction in AgBr crystals leads to the appearance of broad bands in their PL spectra. The emission at a certain wavelength contains contributions from the D–A pairs with various distances between donors and acceptors, which is manifested as a distribution of exchange interactions in the ODMR spectra measured at a certain emission wavelength.

An analysis of the ODMR spectra measured at various emission wavelengths and chopping frequencies showed that the shape of the observed ODMR signals corresponds to a superposition of the signals from exchange-coupled D–A pairs (SEC and localized holes) with a certain distribution of exchange interactions related to the distribution of distances between donors and acceptors. Indeed, a decrease in the detection wavelength or an increase in the microwave power and/or the chopping frequency leads to a shift of the ODMR signal peak in accordance with the increase in magnitude of the exchange splitting (Fig. 2a).

In the bulk AgBr crystal, D–A pairs are predominantly encountered for which $J \approx 0$, while the fraction of pairs with nonzero exchange is rather insignificant and manifested only by the broadening and characteristic shape of the ODMR line of shallow electron centers and localized holes. The opposite situation is observed for AgBr nanocrystals, where no distant pairs are present because of small crystal size and only pairs featuring considerable exchange interactions are manifested in the ODMR spectra. Here, the region of g values corresponding to isolated donors and acceptors (ODMR of distant pairs) must display minimum signals. A shift of the ODMR minimum in the spectrum of sample 3 toward lower fields as compared to the line of shallow electron centers in the bulk AgBr (cf. SEC and SEC* in Fig. 1b) is probably indicative of an increase in the g value of these centers in AgBr nanocrystals as a result of the spatial confinement.

It was established that the holes in AgCl crystals exhibit self-localization due to the Jahn–Teller effect [2]. In AgCl nanocrystals, the Jahn–Teller effect is partly suppressed which leads to a change in parameters of the spin Hamiltonian [4, 5]. It was previously accepted that no self-localization of holes takes place in the bulk AgBr [2, 14]. However, based on the results of this study, we believe that the holes in AgBr can be self-localized as well. However, in contrast to the situation in AgCl, the dynamic Jahn–Teller effect taking place in AgBr leads to isotropization of the g value, as observed in experiment. The g value of holes in AgBr is close to an average g value of the self-localized holes in AgCl. According to this approach, the exciton in AgBr possesses qualitatively the same structure as the self-localized exciton in AgCl in which the wave function of an electron trapped by a self-localized hole is close to the wave function of a shallow electron center. A smaller magnitude of the singlet–triplet splitting observed in AgBr can be explained by a more strongly delocalized wave function of the electron part of the exciton.

In the region of strong fields ($B > 1.6$ T), the ODMR spectrum exhibits only signals from the shallow electron centers. The ODMR signal amplitude is proportional to the number N of recombining pair with a given exchange J corresponding to the resonance magnetic field B. Using the results of calculations presented in Fig. 2b and the ODMR line shape, it is possible to reconstruct a distribution of the number N of recombining pairs with respect to the exchange interaction constant J. The result of such reconstruction is presented by curve $N(J)$ depicted in the right-hand part of Fig. 2b. With an allowance for the exponential dependence of the exchange interaction magnitude on the D–A distance ρ, we can also determine the distribution of D–A pairs with respect to their spacing.

Figure 3a shows the results of such calculations performed with $a_D = 2$ nm and $|J_0| = 5$ cm^{-1} for the ODMR spectra measured at the three emission wavelengths indicated above. The shape of the distribution profiles is close to Gaussian (dashed lines in Fig. 3a). As can be seen from these distributions, the emission from KBr:AgBr contained no contribution due to the distant pairs, just as is expected for nanocrystals with dimensions on the order of several nanometers; it is also seen

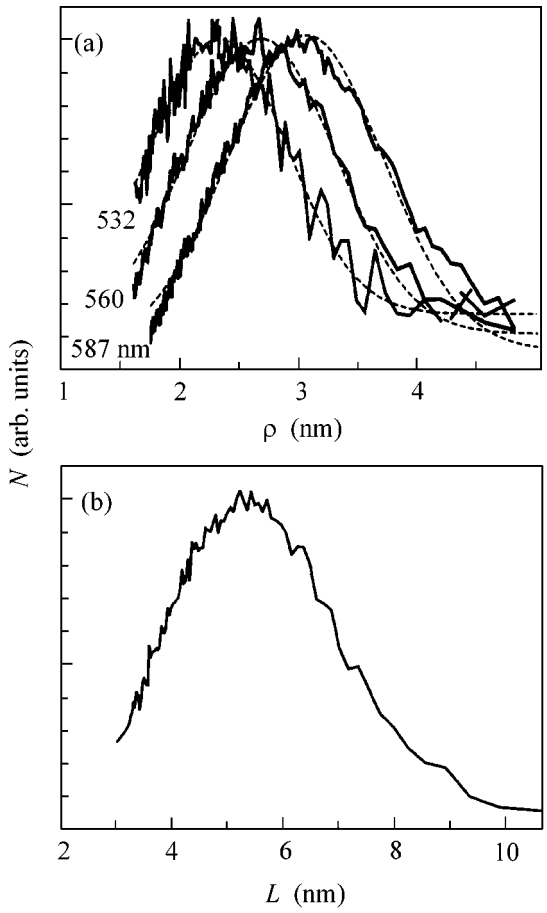

Fig. 3. (a) Distribution of the number of recombining D–A pairs with respect to their spacing determined from the ODMR spectra measured for KBr:AgBr sample 3 using three emission wavelengths (587, 560, and 532 nm). Dashed lines show approximation by the Gaussian profiles; (b) the distribution of AgBr nanocrystals with respect to size in KBr:AgBr sample 3.

that the average ρ value decreases with the PL wavelength used to detect the ODMR signals.

It was natural to suggest that the most probable position of a shallow donor is at the center of an AgBr nanocrystal, while a hole most probably occurs at the surface of this crystal. Assuming that $L \approx 2\rho$, we can estimate the average size of nanocrystals from the resulting $N(J)$ distributions. As can be seen from Fig. 3a, the luminescence at a shorter wavelength is due to nanocrystals with a smaller average size. The total distribution of nanocrystals with respect to their dimensions in KBr:AgBr samples can be determined from an ODMR spectrum measured using the total optical emission from the sample. Figure 3b shows a distribution of the nanocrystal size in KBr:AgBr sample 3, which was obtained upon analysis of the ODMR spectrum *3*.

In contrast to the case of bulk AgBr and AgBr microcrystals, the ODMR spectrum of nanocrystals reveals no contribution due to localized excitons with a fixed exchange interaction magnitude.

Thus, we have established that crystalline KBr boules grown from a KBr:AgBr melt with a large (1–2 mol %) concentration of AgBr impurity contain self-organized AgBr inclusions representing both microcrystals, retaining properties of the bulk material, and nanocrystals in which significant role belongs to the spatial confinement effects. These effects are manifested by the maximum distance between recombining donor–acceptor pairs being restricted to the nanocrystal size and by a change in the *g* value of shallow electron donor centers. Based on an analysis of the exchange interactions in nanocrystals, a distribution of distances in the donor–acceptor pairs is determined and the dimensions of nanocrystals are estimated.

This study was supported in part by the Russian Foundation for Basic Research (project no. 00-02-16950) and by the Federal Program “Physics of Solid State Nanostructures.”

REFERENCES

1. D. Bimberg, M. Grundmann, and N. N. Ledentsov, *Quantum Dot Heterostructures* (Wiley, Chichester, 1999).
2. P. Marchetti and R. S. Eachus, Adv. Photochem. **17**, 145 (1992).
3. P. J. Rodney, A. P. Marchetti, and P. M. Fauchet, Phys. Rev. B **62**, 4215 (2000).
4. P. G. Baranov, V. S. Vikhnin, N. G. Romanov, and V. A. Khramtsov, Pis’ma Zh. Éksp. Teor. Fiz. **72**, 475 (2000) [JETP Lett. **72**, 329 (2000)].
5. P. G. Baranov, V. S. Vikhnin, N. H. Romanov, *et al.*, J. Phys.: Condens. Matter **13**, 2651 (2001).
6. M. T. Bennebroek, A. Arnold, O. G. Poluektov, *et al.*, Phys. Rev. B **53**, 15607 (1996).
7. M. T. Bennebroek, A. Arnold, O. G. Poluektov, *et al.*, Phys. Rev. B **54**, 11276 (1996).
8. A. P. Marchetti, K. P. Johansson, and G. L. McLendon, Phys. Rev. B **47**, 4268 (1993).
9. A. Marchetti, P. J. Rodney, and W. von der Osten, Phys. Rev. B **64**, 132201 (2001).
10. V. G. Grachev, Zh. Éksp. Teor. Fiz. **92**, 1834 (1987) [Sov. Phys. JETP **65**, 1029 (1987)].
11. R. T. Cox and J. J. Davies, Phys. Rev. B **34**, 8591 (1986).
12. W. A. Barry and G. D. Watkins, Phys. Rev. B **54**, 7789 (1996).
13. P. J. Dean, in *Progress in Solid State Chemistry*, Ed. by J. D. McCaldin and G. Somorjaj (Pergamon, Oxford, 1973), Vol. 8, p. 1.
14. W. von der Osten and H. Stolz, J. Phys. Chem. Solids **51**, 765 (1990).

Translated by P. Pozdeev

JETP Letters, Vol. 76, No. 7, 2002, pp. 469–471. From Pis'ma v Zhurnal Éksperimental'noĭ i Teoreticheskoĭ Fiziki, Vol. 76, No. 7, 2002, pp. 547–549.

Observation of a Light-Induced Nonohmic Current in a Toroidal-Moment-Possessing Nanostructure¶

S. A. Emelyanov[1, *], B. Ya. Meltser[2], and S. V. Ivanov[2]

[1] *Division of Solid State Electronics, Ioffe Physicotechnical Institute, Russian Academy of Sciences, Politekhnicheskaya ul. 26, St. Petersburg, 194021 Russia*

** e-mail: sergey.emelyanov@mail.ioffe.ru*

[2] *Center of Nanoheterostructures, Ioffe Institute, Russian Academy of Sciences, Politekhnicheskaya ul. 26, St. Petersburg, 194021 Russia*

Received September 5, 2002

We report on the first observation of light-induced nonohmic current in a semiconductor nanostructure. The effect is revealed in an unbiased asymmetric InAs quantum well under excitation by far-infrared laser radiation in the presence of a tilted magnetic field. It is interpreted in terms of a nonzero toroidal moment of a two-dimensional electron gas. © *2002 MAIK "Nauka/Interperiodica".*

PACS numbers: 73.21.Fg; 73.50.Pz

Even in the framework of classical electrodynamics, it can be shown that for the complete characterization of a system possessing an arbitrary distribution of currents and charges, three independent families of electromagnetic multipoles should be taken into account: electric, magnetic and toroidal moments [1]. The first two families have been well known for a very long time while the third one was introduced not long ago, in 1957, by Ya.B. Zel'dovich [2] to explain the effect of parity violation under weak interactions in nuclear systems (for the concept of toroidal moment, see, e.g., [3, 4] and references therein). Since 1978, a number of theoretical works have been devoted to various aspects of so-called toroidal state of condensed matters, which is characterized by nonzero toroidal moment density (see, e.g., [5]). The most nontrivial effects predicted for toroidal-moment-possessing systems are related to their magnetic properties. One of such effects is so-called superdiamagnetism, which implies a system in nonsuperconducting phase possessive of a giant diamagnetic susceptibility close to the theoretical limit [6].

The idea that an in-plane magnetic field gives rise to toroidal dipole moment in asymmetric nanostructures was first proposed in [7]. It was shown that nonzero toroidal moment is always accompanied by an asymmetry of energy spectrum of the system ($E(k) \neq E(-k)$), and k-dependent excitation of such a system may give rise to a drift electric current in it, as well as to electric polarization. In the limit of low magnetic fields, these effects can be described by the following phenomenological relations:

$$J = \beta T; \tag{1}$$

$$P \sim [BT] \equiv [B[BI]], \tag{2}$$

where T is the time-odd polar vector (toroidal dipole moment), β is a dissipation coefficient, and I is the polar vector perpendicular to the well plane. Thus, k-dependent excitation of an asymmetric nanostructure in the presence of a magnetic field tilted in the XZ plane (Z is the growth axis) may result in a drift current along the Z axis proportional to (B_x), as well as in an electric polarization in the XZ plane which is proportional to $B_x \cdot B_z$. The former effect was observed in asymmetric quantum structures under either photoexcitation [8–10] or excitation by an external electric field [11]. However, no evidence of the latter effect has been observed up to now.

In this letter, we report on the first observation of a light-induced nonohmic current related to the nonzero toroidal moment of a two-dimensional (2D) electron gas. Experiments were performed on (001)-MBE grown single-quantum-well InAs/GaSb structures supplied by thin AlSb barriers to avoid hybridization-related effects [12]. A typical structure consists of a 15-nm InAs channel sandwiched between two 0.3-nm-wide AlSb barriers and capped with a 20-nm GaSb layer. Low-temperature electron-sheet density and mobility were 1.7×10^{12} cm^{-2} and 1.5×10^5 cm^2/V s, respectively. Each device was supplied by a pair of striplike ohmic contacts. A high-power pulsed NH_3 laser optically pumped by a CO_2 laser was used as a source of far-infrared radiation. The laser wavelength was 90.6 μm, pulse duration was about 30 ns, and peak laser radiation intensity was on the order of 100 W/cm^2. Magnetic field was provided by a superconducting solenoid. The experiments were performed at 4.2 K at normal incidence of light on the sample surface. Light-

¶This article was submitted by the authors in English.

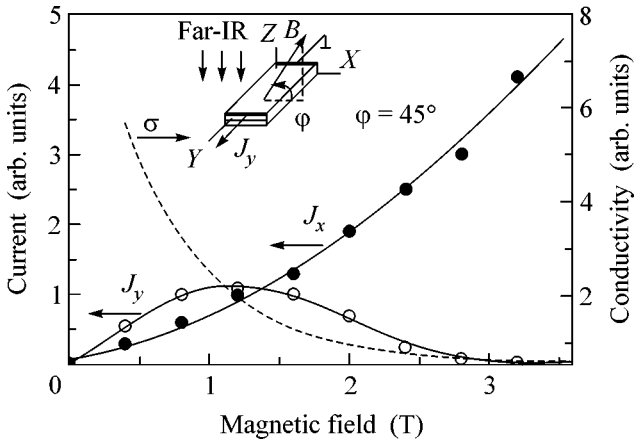

Fig. 1. Light-induced currents as a function of magnetic field B at $\varphi = 45°$. Solid circles: J_x; open circles: J_y. Solid curves are the interpolation of the experimental data. Dotted curve is the device ohmic conductivity as a function of B. The inset shows the geometry of the J_y measurements. The geometry for J_x can be obtained by the clockwise rotation of the sample through 90° about the Z axis.

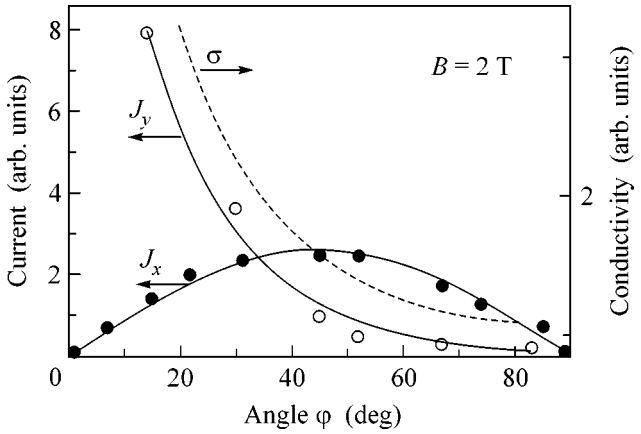

Fig. 2. Light-induced currents as a function of angle φ at $B = 2$ T. Solid circles: J_x; open circles: J_y. Solid curves are the interpolation of the experimental data. Dotted curve is the device ohmic conductivity as a function of φ.

induced in-plane currents in unbiased devices were detected through the voltage drop on a 50 Ω load resistor in a short-circuit regime by a high-speed storage oscilloscope. In-plane current was measured in two directions: either across or along the in-plane component of magnetic field. The former experimental geometry is shown in the inset in Fig. 1. The latter geometry can be obtained by the clockwise rotation of the sample by 90° about the Z axis.

Pronounced current pulses were observed in both the X and Y directions. These pulses copied the shape of initial laser pulses, indicating that the process responsible for their appearance had a steady-state character with a response time shorter than 10^{-7} s. The currents were found to be independent of both light direction and polarization, as well as of the orientation of crystallographic axis in the well plane. This means that the currents were caused not by the asymmetry carried by light but by the inner system asymmetry provided by the electric field built-in across the well [13]. The current along the Y axis (J_y) was odd with respect to the external magnetic field B, while the current along the X axis (J_x) was even with respect to B. Switching of the angle between the magnetic field and the well plane from φ to $-\varphi$ reversed the sign of J_x, while the sign of J_y was retained. The dependences of both J_x and J_y on B at $\varphi = 45°$ and the behavior of the device's ohmic conductivity σ are shown in Fig. 1. It is seen that, at low magnetic fields, J_y is proportional to B, but then it goes to zero with increasing B because of a drastic drop in σ. Surprisingly, J_x is clearly insensitive to σ and increases roughly as B^2. To demonstrate this unambiguously, the angle dependences of both J_x and J_y at $B = 2T$ are plotted in Fig. 2 together with the angle dependence of σ. Once again, J_y decreases with increasing B, whereas J_x is clearly insensitive to σ, and its behavior looks like an ideal sinusoid with double angle φ as an argument.

It is easy to see that our experimental results are in good agreement with phenomenological relations (1) and (2). To clarify the microscopic picture of the effect, let us consider the details of the photoexcitation process. It is well known that a 15-nm-thick InAs quantum well contains a highly degenerate two-dimensional electron gas. A minimum electron-sheet density for the occupation of the second size-quantized level is known to be about 2.2×10^{-12} cm^{-2} [14]. Since in our structures this value is about 1.6×10^{-12} cm^{-2}, only the first size-quantized level is occupied at low temperatures, so that the effects related to the presence of the second level can be ignored. Further, since both J_y and J_x are independent of light (left- or right-hand circular) polarization, the spin-related effects (see, e.g., [15, 16]) can also be ignored. Taking into account that (i) the energy of a light quantum in our experiments is as low as 13.7 meV and (ii) B_z is too low to access cyclotron resonance conditions, one can expect that the phonon-assisted optical transitions (Drude-like process) are the predominant mechanism of light absorption. This means that the photoexcitation process is a k-dependent process. Thus, the current J_y can be identified as a conventional drift photogalvanic current, which is related to the imbalance between the k-dependent optical transitions within the asymmetric energy spectrum.

As for the current J_x, its mechanism is not evident. First, the nonohmic nature of J_x indicates that the electrons should be localized along the X axis. Moreover, the polarization effect predicted in [7] also implies the Landau-quantization-related localization of electrons along the X axis and their quasi-free motion along the Y axis. Thus, as a result of the Lorentz force effect, each

of them is supposed to possess an electric dipole moment, so that the total electric dipole moment of the unexcited electron gas should be zero. On the other hand, the Landau quantization at relatively low B is also confirmed experimentally by the observation of well-resolved Shubnikov–de Haas oscillations in InAs quantum wells in a quantizing magnetic field as low as 1 T or even less [17, 18]. Therefore, despite the fact that the in-plane electron motion is not fully suppressed by the quantizing component of the magnetic field (otherwise J_y should be zero), Landau localization effects may be of importance under experimental conditions. In this sense, the current J_x can be interpreted as being due to the nonzero net electric dipole moment of 2D electron gas resulting from the k-dependent photoexcitation.

However, it should be noted that, in the framework of the concept of toroidal moment, one can propose an alternative microscopic mechanism for the current J_x. Indeed, as was also predicted in [7], the Landau quantization in a toroidal-moment-possessing nanostructure can be accompanied by the spatial separation of electrons along the X axis depending on their wave vector along the Y axis. In this case, each phonon-assisted optical transition in k space should be accompanied by the appropriate hoppinglike transition in real space along the X axis as an integral part of the same absorption act. Therefore, taking into account the asymmetry of the energy spectrum, k-dependent photoexcitation can result in a nonzero net hopping in real space along the X axis. Such a process may also be the reason for the nonohmic current. Thus, the identification of a microscopic mechanism of the light-induced nonohmic current under experimental conditions clearly requires further experiments, which will be done in the near future.

We thank A.P. Dmitriev for useful discussions and S.D. Ganichev and Ya.V. Terent'ev for the contribution to the experimental design. This work was supported in part by the Russian Foundation for Basic Research (project nos. 00-02-17045, 01-02-17933), by the Program "Nanostructures," INTAS (grant no. 99-01146), and SNSF (grant no. 7SUPJ062181).

REFERENCES

1. V. M. Dubovik and A. A. Cheshkov, Fiz. Élem. Chastits At. Yadra **5**, 791 (1975) [Sov. J. Part. Nucl. **5**, 318 (1975)].
2. B. Ya. Zel'dovich, Zh. Éksp. Teor. Fiz. **33**, 1531 (1958) [Sov. Phys. JETP **6**, 1184 (1958)].
3. V. M. Dubovik and L. A. Tosunyan, Fiz. Élem. Chastits At. Yadra **14**, 1193 (1983) [Sov. J. Part. Nucl. **14**, 504 (1983)].
4. V. M. Dubovik, M. A. Martsenyuk, and Bijan Saha, Phys. Rev. E **61**, 7087 (2000).
5. A. A. Gorbatsevich and Yu. V. Kopaev, Ferroelectrics **161**, 321 (1994).
6. V. L. Ginzburg, A. A. Gorbatsevich, Yu. V. Kopaev, and B. A. Volkov, Solid State Commun. **50**, 339 (1984).
7. A. A. Gorbatsevich, V. V. Kapaev, and Yu. V. Kopaev, Pis'ma Zh. Éksp. Teor. Fiz. **57**, 565 (1993) [JETP Lett. **57**, 580 (1993)].
8. A. P. Dmitriev, S. A. Emel'yanov, S. V. Ivanov, *et al.*, Pis'ma Zh. Éksp. Teor. Fiz. **54**, 279 (1991) [JETP Lett. **54**, 273 (1991)].
9. Yu. A. Aleshchenko, I. D. Voronova, S. P. Grishechkina, *et al.*, Pis'ma Zh. Éksp. Teor. Fiz. **58**, 377 (1993) [JETP Lett. **58**, 384 (1993)].
10. O. E. Omel'yanovskii, V. I. Tsebro, V. I. Kadushkin, *et al.*, Pis'ma Zh. Éksp. Teor. Fiz. **63**, 197 (1996) [JETP Lett. **63**, 209 (1996)].
11. A. A. Gorbatsevich, V. V. Kapaev, Yu. V. Kopaev, *et al.*, Zh. Éksp. Teor. Fiz. **120**, 954 (2001) [JETP **93**, 833 (2001)].
12. S. de-Leon, L. D. Shvartsman, and B. Laikhtman, Phys. Rev. B **60**, 1861 (1999).
13. It is not necessary to confirm the presence of built-in electric field in our structures since the existence of a light-induced current independent of both light direction and polarization as well as of the orientation of crystallographic axis, is, in itself, such a confirmation. Most likely, this field is related to an uncontrolled asymmetric ionization of interface donor states (see e.g., H. Kroemer, C. Nguyen, and B. Brar, J. Vac. Sci. Technol. B **10**, 1769 (1992)).
14. A. C. H. Rowe, R. S. Ferguson, and R. A. Stradling, in *Proceedings of the 25th International Conference on the Physics of Semiconductors*, Ed. by N. Miura and T. Ando (Springer, 2001), Part 1, p. 765.
15. S. D. Ganichev, E. L. Ivchenko, S. N. Danilov, *et al.*, Phys. Rev. Lett. **86**, 4358 (2001).
16. S. D. Ganichev, V. V. Bel'kov, E. L. Ivchenko, *et al.*, in *Proceedings of the 9th International Symposium "Nanostructures: Physics and Technology", St. Petersburg, Russia, 2001*, p. 252.
17. J. Luo, H. Munekata, F. F. Fang, and P. J. Stiles, Phys. Rev. B **38**, 10142 (1988).
18. S. Brosig, K. Ensslin, B. Brar, *et al.*, Physica B (Amsterdam) **256–258**, 239 (1998).

JETP Letters, Vol. 76, No. 7, 2002, pp. 472–474. Translated from Pis'ma v Zhurnal Éksperimental'noĭ i Teoreticheskoĭ Fiziki, Vol. 76, No. 7, 2002, pp. 550–552.

Field Electron Emission from Ge–Si Nanostructures with Quantum Dots

A. A. Dadykin*, Yu. N. Kozyrev, and A. G. Naumovets***

** Institute of Physics, National Academy of Sciences of Ukraine, Kiev, 03028 Ukraine*

*** Institute of Surface Chemistry, National Academy of Sciences of Ukraine, Kiev, 03680 Ukraine*

naumov@iop.kiev.ua

Received July 24, 2002; in final form, September 12, 2002

Self-assembled arrays of Ge–Si clusters with sizes of ~ 10 nm and a density of ~ 10^{10} cm^{-2} have been grown by molecular beam epitaxy. Stable steady-state field electron emission from such clusters has been observed and studied. The emission is characterized by resonance current peaks, which are explained by the quantization of the electron energy in nanoclusters. The estimation of the ground level energy from their emission measurements coincides with estimates obtained by other methods. *© 2002 MAIK "Nauka/Interperiodica".*

PACS numbers: 73.22.–f; 73.21.La; 79.70.+q; 81.15.Hi

Interest in Ge–Si nanocluster heterostructures is due to the real possibility of creating principally new devices on their basis using quantum-size effects and working even at T ~ 300 K. Infrared photodetectors working in the region 4–6 μm with an efficiency that exceeds the efficiency of detectors based on III–V heterostructures by 3–4 orders of magnitude have already been developed [1]. This has been achieved by obtaining uniform arrays of Ge quantum dots with a sufficiently narrow size distribution and sizes of <10 nm. At such sizes, in spite of the effective mass of charge carriers, which is larger than that for III–V semiconductors, lateral quantization already removes the forbiddenness of optical transitions polarized in the detector plane. This sharply increases the efficiency of the zero-dimensional system as compared to an object having two-dimensional quantum valleys.

The goal of this work was obtaining arrays of Ge nanoclusters with prescribed parameters and studying their electron-emission properties and the possibility of manifestation of quantum-size effects in field electron emission from quantum dots (artificial atoms).

The samples were grown by molecular beam epitaxy of Ge on the Si(100) surface. Because of the high (4.2%) relative mismatch between the parameters of Ge and Si lattices, three-dimensional Ge clusters are formed directly on the clean Si substrate by the Volmer–Weber mechanism. However, these clusters are readily peeled off the substrate. In order to avoid the exfoliation of clusters, a number of buffer layers of a Si_xGe_{1-x} solid solution were deposited, over which a pure Ge film was sputtered with a thickness of several monolayers. Because of a smaller mismatch between the lattice parameters of the Ge film and the Si_xGe_{1-x} substrate, the film grows by the Stransky–Krastanov mechanism. The films were sputtered at temperatures of 350–750°C, which provide the mobility of atoms sufficient for bringing the system to a thermodynamic equilibrium state. The growth process and the chemical composition were monitored by high-energy electron diffraction and Auger spectroscopy, respectively.

In spite of the significant relaxation of elastic strains at the buffer Si–Ge substrate, starting from a thickness of three–five monolayers the layer-by-layer growth of the Ge film changes for the formation of three-dimensional clusters, which provide the minimization of the free energy of the system by means of a decrease in the energy of elastic strains at cluster tips.

A typical image of the array of nanoclusters obtained with the use of an atomic force microscope (AFM) is shown in Fig. 1a. The clusters have a quasi-pyramidal shape with a height of 2–10 nm, a base size of 10–40 nm, and a tip curvature radius of ~ 1 nm. The density of clusters exceeds 10^{10} cm^{-2}. Both the size of the clusters and the distance between them have a relatively small spread around the mean values; that is, certain self-assembling of the system occurs. In this case, the driving force of self-assembling is the tendency of the system to minimize the free energy through minimizing the energy of the elastic deformation associated with the mismatch between the film and substrate lattices.

It is seen in Fig. 1b that three types of clusters, shaped as a hut, dome, and superdome, are formed in the general case. The preferred growth of any of these types can be provided by changing the process conditions. The tips, that is, the parts of the clusters that primarily consist of Ge, can be considered as quantum dots (artificial atoms). With a tip curvature radius of ~1 nm, the electric fields can reach values of >10^7 V/cm necessary for obtaining field electron emission even at

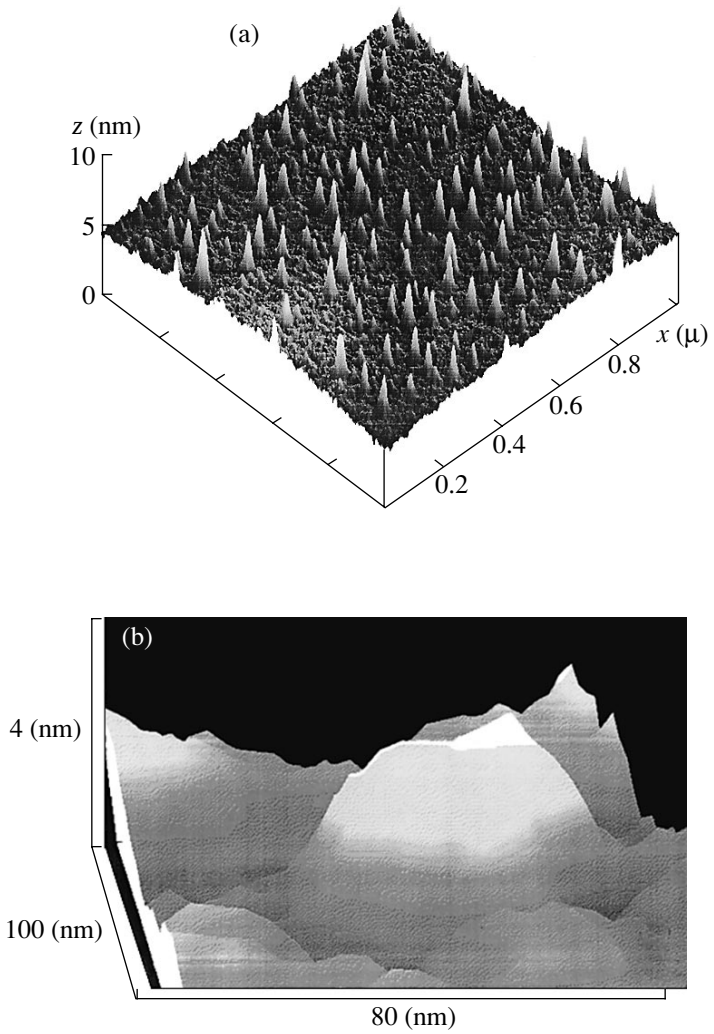

Fig. 1. (a) AFM image of an array of Ge–Si nanoclusters; (b) fragment of the array with hut, dome, and superdome clusters.

relatively small (~10^5 V/cm) macroscopic electric fields. The same estimate for the electric field necessary for the occurrence of tunnel emission is also obtained when individual nanoclusters are considered as artificial atoms similar to a hydrogen atom (see, for example, [2]).

Field electron emission was studied in plane diode cells with an anode covered with a phosphor of the ZnS type to visualize the emission. In all cases, steady-state field electron emission was obtained with a current density of ~1 mA/cm^2 at a mean electric field in the gap between the electrodes of ~10^5 V/cm, which was sufficiently uniform over a surface area of 1 cm^2. A current–voltage characteristic (CVC) of the emission at T = 300 K is given in Fig. 2. A distinctive feature of the emission from Ge quantum dots is the occurrence of current peaks in the CVC. The number of peaks increases with increasing mean height of the grown clusters or with the growth of their height (and the change of their composition) due to coating with the anode material during the passage of high currents. As a result, the CVCs are smoothed. The distance between the current peaks increases with increasing peak number n, which can be seen in Fig. 2. The peaks are more clearly revealed in the CVC constructed in Fowler–Nordheim coordinates $\log(i/U^2) = f(U^{-1})$ (Fig. 3). It may be suggested that the occurrence of current peaks and their position in CVC are associated with the quantization of the energy of electrons in the clusters, which can be considered in our case as quantum dots (artificial atoms). It is notable that the current peaks are clearly revealed in spite of the notable spread of clusters in height. Evidently, this is associated with the fact that the major contribution to emission is made by the currents from the clusters having the smallest tip radius and the largest height.

Because of the complexity of the three-dimensional problem of field electron emission from a quantum-size cluster of a complex shape, we will restrict ourselves to a consideration of the one-dimensional model of a

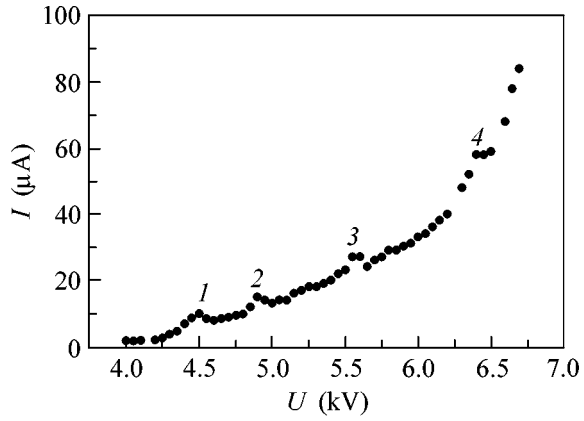

Fig. 2. CVC of field emission from an array of Ge–Si nanoclusters with an area of 0.5 cm^2.

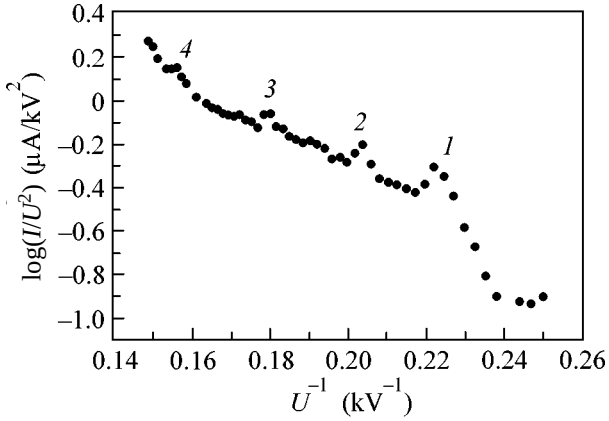

Fig. 3. Characteristic of filed emission from nanoclusters in Fowler–Nordheim coordinates.

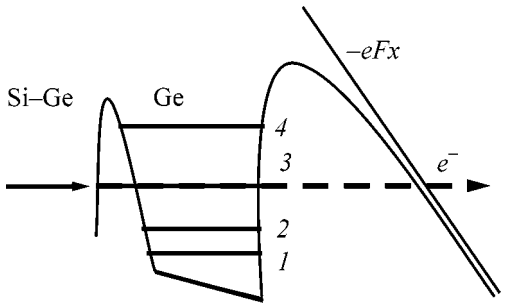

Fig. 4. Energy diagram of field emission from a Ge–Si nanocluster.

potential box. Such a model was used by Duke and Alferieff for the description of field emission through individual adatoms [3]. In our case, such a consideration is acceptable, because a strong electric field is lumped mainly in the region of a cluster tip, and the height of the pyramidal cluster can be considered as the width of the potential well. The difference in the band-gap widths of Si and Ge can be taken as the depth of the potential well for electrons of the Si–Ge heterojunction if the deformation effect on the energy spectrum of charge carriers is neglected, because Si and Ge grown by an epitaxial process exhibit, as a rule, *p*-type conduction due to the occurrence of vacancy defects. In this case, as distinct from the case of *n*-type Si considered in [4], a potential well for electrons is formed in the region of the Si–Ge heterojunction.

The results obtained can be interpreted based on the energy diagram presented in Fig. 4. Because of the penetration of the electric field into the cluster, the discrete electron energy levels in the potential well are displaced, and a current peak appears in the CVC when the level of emergence of electrons from Si becomes coincident with one of the energy levels in the potential well; that is, resonance tunneling occurs.

Under the assumptions adopted, the energy of the ground quantization level in the potential well of the Si–Ge heterosystem becomes equal to $\Delta E \sim 100$ mV, which agrees well with the results of electron tunneling spectroscopy of Si–Ge clusters [5]. The electric field inside the cluster, which displaces the levels by the value of the energy gap between them, can be estimated at $F = \Delta E/h$, where $h \sim 5$ nm is the height of the cluster. This value turns out to be equal to $\sim 3 \times 10^5$ V/cm and virtually coincides with the macroscopic field estimated from the geometry of the test diode. The occurrence of the electric field $F > 10^7$ V/cm necessary for tunnel electron emission into a vacuum can be explained based on the geometry of clusters with a vertex corner radius of <1 nm.

Thus, field electron emission from Ge–Si nanocluster heterostructures found in this work can serve as an efficient method for studying quantum-size effects in such structures and as the physical basis for creating new nanoelectronic devices.

The authors are grateful to Yu.M. Litvin and P.M. Litvin for AFM photographs of nanoclusters.

This work was supported by the National Academy of Sciences of Ukraine, target project no. VTs/85.

REFERENCES

1. P. Boucaud, V. Le Thanh, S. Sauvage, *et al.*, Appl. Phys. Lett. **74**, 401 (1999).
2. A. S. Davydov, *Quantum Mechanics* (Fizmatgiz, Moscow, 1963; Pergamon, Oxford, 1976).
3. C. D. Duke and M. E. Alferieff, J. Chem. Phys. **46**, 923 (1967).
4. A. V. Dvurechenskiĭ and A. N. Yakimov, Fiz. Tekh. Poluprovodn. (St. Petersburg) **35**, 1143 (2001) [Semiconductors **35**, 1095 (2001)].
5. A. I. Yakimov, V. A. Markov, A. V. Dvurechenskii, and O. P. Pchelyakov, J. Phys.: Condens. Matter **6**, 2573 (1994).

Translated by A. Bagatur'yants

JETP Letters, Vol. 76, No. 7, 2002, pp. 475–480. From Pis'ma v Zhurnal Éksperimental'noĭ i Teoreticheskoĭ Fiziki, Vol. 76, No. 7, 2002, pp. 553–558.

On the Aizenman Exponent in Critical Percolation¶

L. N. Shchur* and T. Rostunov

Landau Institute for Theoretical Physics, Russian Academy of Sciences, Chernogolovka, Moscow region, 142432 Russia
**e-mail: lev@itp.ac.ru*

Received September 5, 2002

The probabilities of clusters spanning a hypercube of dimension two to seven along one axis of a percolation system under criticality were investigated numerically. We used a modified Hoshen–Kopelman algorithm combined with Grassberger's "go with the winner" strategy for the site percolation. We carried out a finite-size analysis of the data and found that the probabilities confirm Aizenman's proposal of the multiplicity exponent for dimensions three to five. A crossover to the mean-field behavior around the upper critical dimension is also discussed. © *2002 MAIK "Nauka/Interperiodica".*

PACS numbers: 64.60.Ak; 64.60.Fr

Percolation occurs in many natural processes, from electrical conduction in disordered matter to oil extraction from a field. In the latter, the coefficient of oil extraction from oil sands (the ratio of the actually extracted to the estimated oil) can be as much as 0.7 for light oil and as low as 0.05 for viscous heavy oil. An increase in this coefficient by any new point requires appreciable investment. Additional knowledge about the percolation model can reduce the amount of additional investment.

A remarkable breakthrough in the theory of critical percolation was made in the last decade thanks to a combination of mathematical proofs, exact solutions, and large-scale numerical simulations. Recently, Aizenman has proposed a new exponent that describes the probability $P(k, r)$ of a critical percolation d-dimensional system with the aspect ratio r being spanned by at least k clusters [1],

$$\ln P(k, r) \propto -\alpha_d k^{\zeta} r, \qquad (1)$$

where α_d is a universal coefficient depending only on the universality class, and $\zeta = d/(d-1)$.

In two dimensions, Aizenman's proposal (1) was proved mathematically [1], confirmed numerically [2], and derived exactly [3] using the conformal field theory and Coulomb gas arguments. This exponent seems to be related to the exponents of two-dimensional copolymers [4]. In three dimensions, proposal (1) was checked numerically in [5] and, more recently and more precisely, in [6].

The upper critical dimension of percolation is $d_c = 6$, which follows from the comparison of the exponents derived on the Cayley tree with those satisfying scaling laws (see, e.g., [7] and [8]). The fractal dimension D_f of percolating critical clusters is equal to 4 above d_c, and the number of percolating clusters becomes infinite at $d > d_c$. This fact would imply that $\zeta = 0$ at $d = 6$ if we supposed (rather naively) that Aizenman's formula applies at the upper critical dimension. Supposing that this is true and taking into account that the values of ζ for $d = 2$ and $d = 3$ are, respectively, 2 and 1.5, we can place all three points on the straight line $\zeta = (6 - d)/2$, as depicted in Fig. 1. We can then estimate the respective values of ζ for $d = 4$ and $d = 5$ at $\zeta = 1$ and $\zeta = 0.5$; these values are far from those predicted by Aizenman's formula, which gives 4/3 and 5/4, respectively. In contrast, based on simulations, Sen [9] claims that $\zeta = 2$ for all dimensions from two to five.

The main purpose of our simulations is to estimate the exponents for the dimensions from two to six with an accuracy sufficient for distinguishing between the values predicted for $d = 4$ and $d = 5$ by Aizenman's formula and a naive application of cluster fractal-dimen-

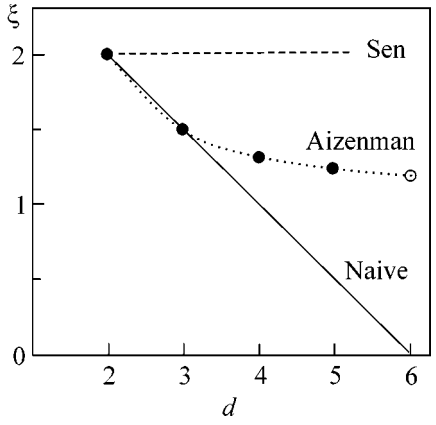

Fig. 1. Variation of Aizenman exponent ζ with the space dimension d, as predicted by Aizenman (circles and dotted line), claimed by Sen (dashed line), and discussed in the text (solid line).

¶This article was submitted by the authors in English.

sion arguments and by the straight-line fit, as discussed above.

In the rest of the paper, we briefly summarize the highlights of our study, then present some details of our research, and finally discuss the results for the Aizenman exponent and the physics of a crossover from the Aizenman picture to the mean-field picture.

Our main results can be summarized as follows.

1. *Modified combination of the Hoshen–Kopelraan algorithm and Grassberger's strategy.* We use the Hoshen–Kopelman (HK) algorithm [10] to generate clusters and Grassberger's "go with the winner" strategy [6] to track spanning clusters. We add a new tag array in the HK algorithm, which allows the reduction of the tag memory order from L^d to L^{d-1}, where L is the linear size of the hypercubic lattice. As a result, the amount of memory is about two orders less for large values of L, and the program is about four times faster—the complexity of the algorithm is compensated by the lower memory capacity needed for swapping to and from the auxiliary array.

2. *Efficient realization of combined shift-register random-number generators.* We use an exclusive-or ($\oplus$) combination z_n of two shift registers:

$$x_n = x_{n-9689} \oplus x_{n-5502},$$
$$y_n = y_{n-4423} \oplus y_{n-2325}, \quad z_n = x_n \oplus y_n \tag{2}$$

(see [11] and the references therein). We reduce the computational time for generating random numbers by a factor of 3.5 through an efficient technical modification: we use the SSE command set that is available on processors of the Intel and AMD series starting from the Intel Pentium III and AMD Athlon XP.

3. *Extraction of the exponents for dimensions three to five*. We first use finite-size analysis to estimate the logarithm of the probability $P(k, r)$ in the limit of infinite lattice size L. We then fit data as a function of the number of spanning clusters k to obtain the Aizenman exponent ζ.

4. *Confirmation of Aizenman's proposal*. The estimates of the exponent for dimensions $d = 2, 3, 4$, and 5 coincide well with those proposed by Aizenman.

5. *Qualitative interpretation of Aizenman's conjecture.* Cardy interpreted Aizenman's result qualitatively in two dimensions on the basis of the assumption that the main mechanism for reducing the number of percolation clusters is the termination some of them. The same result can be derived for the cluster confluence (or merging) mechanism. This means that, in low dimensions, the percolation clusters consist of a number of closed paths (loops), while, in higher dimensions, clusters are more similar to trees. Indeed, it is well known that the probability of obtaining a loop becomes lower for higher dimensions and goes to zero in the limit of infinite dimensions (Cayley tree) [7, 8].

6. *Crossover to mean-field behavior.* We found evidence that the probability of clusters spanning a hypercubic lattice tends to unity in the limit of high dimensions, as follows from the well-accepted picture. We did not find any dramatic changes in the probabilities around the upper critical dimension $d_c = 6$ but rather found evidence for a crossover. Therefore, Aizenman's formula (1) can also apply to dimensions higher (but not too much higher) than the upper critical dimension and describe approximately the probabilities of spanning clusters in large, though finite-size systems.

We follow with the details of the critical percolation, simulations, and data analysis.

Spanning probability. We can define the probability $P(k, r; L)$ that k clusters traverse a d-dimensional hyperrectangle $[0, L]^{d-1} \times [0, Lr]$ in the Lr direction [1]. Provided that the scaling limit exists (this was proved recently by Smirnov for the percolation in plane [12]), the probability $P(k, r)$ can be defined as a limit of $P(k, r; L)$ as $L \longrightarrow \infty$. Aizenman proposed that $P(k, r)$ should behave according to (1) in the dimensions from three to five. The validity of formula (1) for the percolation plane was well established in [1, 3, 2].

Numerical results ([5] and [6]) for the exponent ζ for critical percolation on cubic lattices seems to confirm Aizenman's proposal for the value of $\zeta = 1.5$.

Actually, we can consider the probability $P(k, r)$ as the probability of obtaining k clusters at the distance r from the left side of the hyperrectangle if clusters grow to the right. Only two processes can change the number of clusters: cluster merging and cluster termination.

The differential dP of the probability is

$$dP \propto P(k, r)k^{1/(d-1)}kdr, \tag{3}$$

where the right-hand side represents the product of the probability $P(k, r)$ and the differential of the total border hyperarea of k clusters, each with the hyperarea differential $k^{1/(d-1)}dr$. This expression follows from the fact that the unit area of measure is proportional to the characteristic transverse length of "infinite" clusters. Therefore, the transverse area remains constant as k changes, while the longitudinal length increment in these units is $\propto k^{1/(d-1)}dr$. Integrating Eq. (3), we recover probability (1). Thus, $P(k, r)$ describes the probability that k clusters do not merge together.

The same probability can be obtained by the process of cluster termination, as given by Cardy in plane [3], which can easily be extended to dimensions $d > 2$.

This means that the exponent ζ cannot be larger than the one proposed by Aizenman, and $\zeta = d/(d-1)$ is the upper bound for the exponent.

Algorithms and realizations. The classical realization of the HK algorithm [10] requires memory for two major structures: an array for keeping a $(d-1)$-dimensional cluster slice and a tag array. The total memory required by the algorithm is $\propto L^{d-1} + p_c rL^d$, where p_c is the site percolation threshold value. Therefore, for large rL, one of the main advantages of the HK algorithm (i.e., relatively low memory consumption) is negated

Table 1

d	k	$L_{\min}$	$L_{\max}$	δL	p_c	Ref.
2	1–5	16	256	16–32	0.59274621(13)	[13]
3	1–6	8	64	4, 8	0.3116080(4)	[14]
4	1–6	8	48–56	4, 8	0.196889(3)	[15]
5	1–6	4	32, 24	4, 8	0.14081(1)	[15]
6	1–6	4	15–16	3–5	0.109017(2)	[16]
7	1–4	4	10	1	0.0889511(9)	[16]

Minimal $L_{\min}$ and maximal $L_{\max}$ linear sizes of the percolation lattice and the interval δL between two consecutive values of L depending on the dimension d and number of clusters k. The values of p_c are taken from the references in the last column.

by the second term. Our modification of the original algorithm allows the memory for the tag array to be reduced to about $3p_cL^{d-1}$.

Instead of keeping all tags in memory and selecting new tags with increasing tag numbers, we create two arrays, of which one keeps the tag value and the other one keeps the number N of the slice where the corresponding tag was last used. When we build a cluster, we update this array with $N = N_{\text{current}}$ for the tags used. If $N < N_{\text{current}} - 1$, then this tag is not on the front surface of the sample, and it will never be used again, so that we can, therefore, reuse it. We note that cluster-size information should be taken into account before reusing the associated tag, if the size information is required.

We use the "go with the winner" strategy [6] as follows. If the system has k spanning clusters for some aspect ratio $r = n\delta r$, it is stored in memory and is grown for δr. If the resulting configuration has k spanning clusters, it is stored, and the growth process continues. Otherwise, we return to the previously saved state. Using this procedure, we calculate the probability $P_i(\delta r)$ that the system propagates at the distance rL from the position $r = (i - 1)\delta r$. Finally, we obtain $P(r = n\delta r) = \prod_{i=1}^{n} P_i(\delta r)$. By choosing sufficiently small values of δr, we can achieve rather high probabilities of $P_i(\delta r)$ (which can be determined from a few realizations), while the total probability may be very small (down to $\propto 10^{-100}$ in our case).

The random-number generator was optimized for the SSE instruction set as follows. Because the length of all four RNG legs is $\{a|b\}_{\{x|y\}} > 4$, the nth step of the RNG does not intersect the $(n + 3)$th step. Therefore, we can pack four consecutive 32-bit values of $\{x_{n-\{a_x|b_x\}}\}$ and $\{y_{n-\{a_y|b_y\}}\}$ into 128-bit XMM registers, process them simultaneously [see Eq. (2)] and thus obtain z_n, z_{n+1}, z_{n+2}, and z_{n+3} within one RNG cycle.

Data analysis. The lattice size was varied from $L_{\min}$ to $L_{\max}$ with the step δL. In Table 1, particular values of the simulation parameters are presented together with the interval of the number of clusters k depending on the dimension d. The direct result of the simulations is the probabilities $P(k, r; L)$ that exactly k clusters connect two opposite surfaces (separated by the distance rL) of the rectangle with size L^{d-1} in the "perpendicular" direction, in which we apply periodic boundary conditions. We use the values of site percolation thresholds on hypercubic lattices from [13–16], as shown in Table 1.

Data analysis consists of three steps. First, we compute the slope $s(L)$ of $\ln P(k, r; L)$ for a given dimension d, number of clusters k, and linear lattice size L. An example of such a function is given in Fig. 2 for $\ln P(5, r; 16)$ in the dimension four. We also plot the logarithm of the probability $P_+(k, r; L) = \sum_{k' \geq k} P(k', r; L)$ of the event that at least k clusters span the (hyper)rectangle at the distance rL. To calculate $s(L)$, we use data only in the interval of the aspect ratio r between 1.5 and 5. We note that the probability of five clusters spanning a rectangle with linear size $L = 16$ at a distance of $5 \times 16 = 80$ is extremely small $\approx 10^{-52}$.

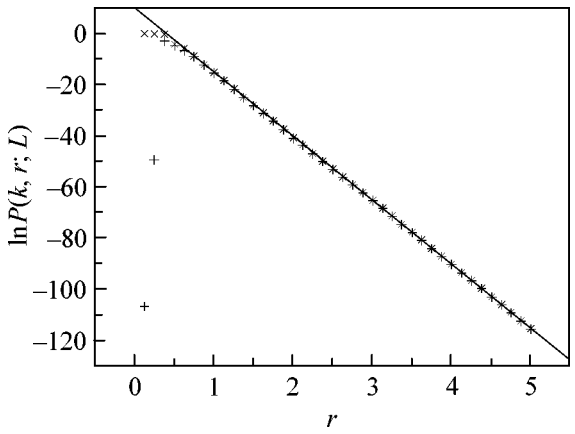

Fig. 2. The logarithms of the probabilities of exactly k clusters $P(k, r; L)$ (+) and of at least k dusters $P_+(k, r; L)$ (×) for the dimension $d = 4$ and the number of clusters $k = 5$ as functions of the aspect ratio r, as discussed in the text.

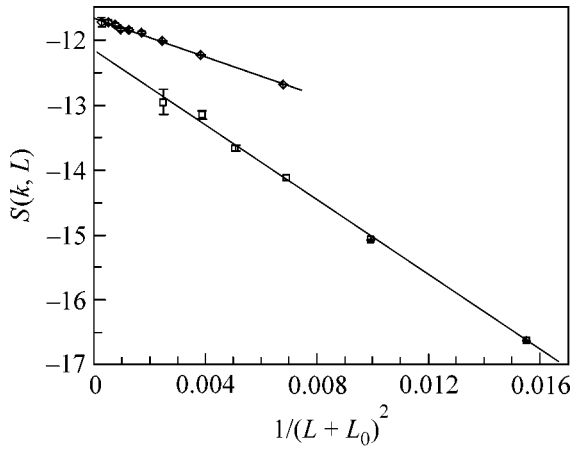

Fig. 3. Plot of $s(k; l)$ for $k = 3$ clusters in the dimension four as a function of $1/(L + L_0)$ with the fitting parameter $L_0 = 4.12$ (□) and for $k = 4$ clusters in the dimension six with $L_0 = 4.03$ (◇). Straight lines result from fitting to the corresponding data, as discussed in the text.

Second, we compute probabilities in the limit of an infinite system size L, fitting slopes $s(k)$ with the expression (see Fig. 3)

$$s(k; L) = s(k) + \frac{B}{(L + L_0)^t}, \quad (4)$$

where B, t, and L_0 are fitting parameters [17, 5, 18]. The resulting values of the slopes $s(k)$ are presented in Table 2. The number of runs used to compute each particular entry in Table 2 varied from 10^6 to several tens for higher dimensions.

We checked the accuracy of our simulations, as well as the validity of the approach for site percolation on a square lattice. Table 3 shows a comparison of our results for the slope s with the exact values and with earlier simulations, in which the other modification of the HK algorithm, but not the Grassberger strategy, was used. We note that our results coincide well with the exact results and give a higher accuracy for larger values of k in comparison with the previous numerical results, despite the smaller computation time. Our data for $k = 1$ is less accurate because of the smaller statistics (10^6 runs, compared to 10^8 samples in [5]). This is a direct demonstration of the effectiveness of the Grassberger strategy for large values of k.

Finally, we use values in Table 2 to determine the Aizenman exponent ζ by fitting the data in each column to

$$s = A(k^2 - k_0)^{p/2} \quad (5)$$

in two and three dimensions, as proposed by Grassberger [6], and to

$$s = A(k^p - k_0) \quad (6)$$

in higher dimensions. Here, A, k_0, and p are fitting parameters. We take only the leading behavior in k into account.

Spanning, proliferation, and crossover to mean-field behavior. The results of the final fit to (5) and (6) are shown in Table 4. The second row for each particular dimension d is the fit with the power p fixed to the Aizenman exponent value. This is done to check the fit stability. Indeed, the values of A and k_0 coincide within one standard deviation for the dimensions two to five.

The larger deviations of parameters for the dimensions six and seven may be attributed to the appearance of cluster proliferation—the number of clusters is known [1] to grow as L^{d-6} in dimensions $d > d_c = 6$. We plot the coefficient α_d [defined by Eq. (1)] in Fig. 4 as a function of the dimension d. The probability of exactly one cluster spanning at the given distance r becomes smaller as the dimension increases from two to five and larger for larger dimensions, as can be seen from the first row ($k = 1$) of Table 2 and from the lower curve in Fig. 4. For any fixed d, the value of α_d approaches some limit for the dimensions two to five and $k > 2$, which suggests the values of corrections to the leading behavior in k (see Eqs. (5) and (6)).

Table 2

k	d				
	3	4	5	6	7
1	–1.377(1)	–1.774(3)	–1.859(9)	–1.76(2)	–1.48(4)
2	–6.919(6)	–6.330(15)	–5.57(6)	–4.73(8)	–3.55(11)
3	–13.655(15)	–11.64(4)	–9.95(12)	–8.27(12)	–6.25(16)
4	–21.47(3)	–17.77(6)	–14.65(20)	–11.95(25)	–9.3(3)
5	–30.23(3)	–24.02(8)	–19.9(3)	–15.75(30)	
6	–40.02(6)	–31.0(1)	–25.0(3)	–22.7(2)	

Values of $s(k)$ for different numbers of clusters k and dimensions d for site percolation on hypercubic lattices with periodic boundary conditions in directions perpendicular to the spanning direction.

The fact that the value of ζ, which we formally extracted from our data for $d = 6$, more or less coincides with $\zeta = d/(d-1) = 6/5$, as is formally calculated using the Aizenman expression, may be interpreted as an indication that the number of clusters depends logarithmically on the lattice size L. One can expect that the logarithmic behavior is visible only for somewhat larger values of L than we have used so far (see Table 1). With the values of L of the order we used in simulations, we see effectively the same picture as for the lower dimensions—clusters span according to the Aizenman formula. This means that at small (or moderate) values of L, the main mechanism is as discussed above: cluster merging and termination. And only at sufficiently large system sizes we will see cluster proliferation. An indication of that can be seen from the values of α_d in the dimension seven in Fig. 4. The probabilities become closer, and this can be attributed to cluster proliferation and treated as a crossover to the mean-field behavior.

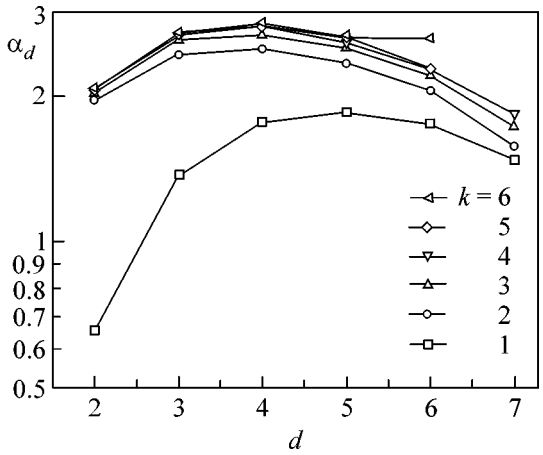

Fig. 4. The coefficient α_d (as a function of the dimension d) extracted from the probabilities $P(k, r)$ for different numbers of clusters k.

Discussion. The results have shown the validity of Aizenman's proposal in the dimensions three to five (results on a plane were already proved rigorously) and do not support Parongama Sen's claims based on their simulations (Fig. 1). We have found evidence of cluster proliferation for the dimension seven. The analysis can be extended to the number of spanning clusters to distinguish exponential decay with the system size of the number of clusters for the dimension five, logarithmic growth of them for the dimension six, and linear growth for the dimension seven. The same technique can be used to numerically establish such a crossover to the mean-field picture, although a significantly longer computational time than we used is needed for this. In fact, the linear growth of the multiplicity of spanning clusters for seven-dimensional critical percolation was confirmed numerically in preprint [19] posted at the *arXiv* preprint library a few days after our cond-mat/0207605.

We are grateful to P. Grassberger and R. Ziff for useful discussions of algorithms. We also thank S. Korshunov and G. Volovik for the discussion of the results. This work was supported by the Russian Foundation for Basic Research.

Table 3

k	This paper	Exact from [3]	From [5]
1	–0.6541(5)	–0.6544985	–0.65448(5)
2	–7.855(3)	–7.85390	–7.852(1)
3	–18.32(1)	–18.3260	–18.11(15)
4	–32.99(3)	–32.9867	
5	–51.83(2)	–51.8363	

Values of $s(k)$ in two dimensions for different k calculated in this paper using the exact Cardy formula [3] and estimated in [5] for site percolation on a tube.

Table 4

d	A	k_0	p	d	A	k_0	p
2	2.090(4)	0.244(5)	2.0012(10)	5	2.8(1)	0.40(4)	1.24(3)
	2.0940(5)	0.2489(7)	2		2.78(2)	0.38(2)	5/4
3	2.81(4)	0.64(4)	1.489(7)	6	2.8(8)	0.5(3)	1.12(14)
	2.757(2)	0.587(3)	3/2		2.41(5)	0.33(6)	6/5
4	3.06(20)	0.41(6)	1.315(30)	7	1.4(10)	0.08(116)	1.4(4)
	2.949(5)	0.373(3)	4/3		2.03(12)	0.50(13)	7/6

Values of the fitting parameters A and k_0 and the power p as defined in Eqs. (5) and (6) for the dimension d.

REFERENCES

1. M. Aizenman, Nucl. Phys. B **485**, 551 (1997); cond-mat/9609240.
2. L. N. Shchur and S. S. Kosyakov, Int. J. Mod. Phys. C **8**, 473 (1997); cond-mat/9702248.
3. J. Cardy, J. Phys. A **31**, L105 (1998); cond-mat/9705137.
4. B. Duplantier, Phys. Rev. Lett. **82**, 880 (1999); cond-mat/9812439.
5. L. N. Shchur, in *Computer Simulation Studies in Condensed-Matter Physics XII*, Ed. by D. P. Landau, S. P. Lewis, and H.-B. Schüttler (Springer-Verlag, Heidelberg, 2000); cond-mat/9906013.
6. P. Grassberger, Comput. Phys. Commun. **147**, 64 (2002); cond-mat/0201313; P. Grassberger and W. Nadler, cond-mat/0010265.
7. D. Stauffer and A. Aharony, *Introduction to Percolation Theory* (Taylor & Francis, London, 1992).
8. A. Bunde and S. Havlin, in *Fractals and Disordered Systems*, Ed. by A. Bunde and S. Havlin (Springer-Verlag, Berlin, 1996, 2nd ed.).
9. P. Sen, Int. J. Mod. Phys. C **8**, 229 (1997); cond-mat/9704112.
10. J. Hoshen and R. Kopelman, Phys. Rev. B **14**, 3438 (1976).
11. L. N. Shchur, Comput. Phys. Commun. **121–122**, 83 (1999); hep-lat/0201015.
12. S. Smirnov, C. R. Acad. Sci., Ser. I **333**, 239 (2001); http://www.math.kth.se/~stas/papers/percras.ps.
13. M. E. J. Newman and R. M. Ziff, Phys. Rev. Lett. **85**, 4104 (2000); cond-mat/0005264.
14. C. D. Lorenz and R. M. Ziff, J. Phys. A **31**, 8147 (1998); cond-mat/9806224.
15. G. Paul, R. M. Ziff, and H. E. Stanley, Phys. Rev. E **64**, 026115 (2001); cond-mat/0101136.
16. P. Grassberger, cond-mat/0202144.
17. R. M. Ziff, Phys. Rev. Lett. **69**, 2670 (1992).
18. One could expect an increase in finite-size effects as k increases. Indeed, this was found by R. Ziff (private communication) in two dimensions for large values of $k \approx 10$.
19. G. Andronico, A. Coniglio, and S. Fortunato, hep-lat/0208009.

JETP Letters, Vol. 76, No. 7, 2002, pp. 481–483. Translated from Pis'ma v Zhurnal Éksperimental'noĭ i Teoreticheskoĭ Fiziki, Vol. 76, No. 7, 2002, pp. 559–561.

Cloning of Qubits of a Quantum Computer

V. N. Dumachev* and S. V. Orlov

Voronezh Militia Institute, Ministry of Internal Affairs of the Russian Federation, Voronezh, 394065 Russia

** e-mail: dum@comch.ru*

Received July 29, 2002; in final from, September 9, 2002

A system of unitary transformations providing two optimal copies of an arbitrary input cubit is obtained. An algorithm based on classical Boolean algebra and allowing one to find any unitary transformation realized by the quantum CNOT operators is proposed. © *2002 MAIK "Nauka/Interperiodica".*

PACS numbers: 03.67.Lx

It is known that an arbitrary quantum state

$$|\psi\rangle_0 = \alpha|0\rangle_0 + \beta|1\rangle_0 \quad (1)$$

cannot be copied exactly (cloned). The no-cloning theorem was proved in [1]. However, Buzek and Hillery [2] found a unitary transformation entangling two qubits $|\psi\rangle_{12} = |00\rangle_{12}$ with the input qubit $|\psi\rangle_0$ so that the output state has the form

$$|\Psi^{\text{out}}\rangle = |\Phi_0\rangle_{01}|0\rangle_2 + |\Phi_1\rangle_{01}|1\rangle_2, \quad (2)$$

where

$$\begin{aligned} |\Phi_0\rangle &= \sqrt{\frac{1}{6}}(2\alpha|00\rangle + \beta|01\rangle + \beta|10\rangle), \\ |\Phi_1\rangle &= \sqrt{\frac{1}{6}}(2\beta|11\rangle + \alpha|01\rangle + \alpha|10\rangle). \end{aligned} \quad (3)$$

The reduced qubit density operators ρ_0^{out}, ρ_1^{out}, and ρ_2^{out} at the output are related to the input density operator ρ^{in} as

$$\rho_{0,1}^{\text{out}} = \frac{5}{6}\rho^{\text{in}} + \frac{1}{6}\rho_\perp^{\text{in}},$$

$$\rho_2^{\text{out}} = \frac{2}{3}\rho^{\text{in}} + \frac{1}{3}\rho_\perp^{\text{in}}.$$

Here, $\rho_\perp^{\text{in}} = |\psi_\perp\rangle_0\langle\psi_\perp|$, where $|\psi_\perp\rangle_0 = \alpha|1\rangle_0 - \beta|0\rangle_0$ is the state orthogonal to the input state, $\alpha = e^{i\varphi}\sin(\vartheta/2)$, and $\beta = \cos(\vartheta/2)$. The quality of obtained copies is specified by the cloning accuracy *F*, which is determined by the overlap of the input and output states [3]

$$F = \frac{1}{4\pi}\int_0^{2\pi} d\varphi \int_0^{\pi} \langle\psi^{\text{in}}|\rho^{\text{out}}|\psi^{\text{in}}\rangle \sin\vartheta\, d\vartheta.$$

Thus, the output qubits ρ_0^{out} and ρ_1^{out} consist of 5/6 fraction of the input qubit ρ^{in} and 1/6 fraction of an admixture. The qubit $|\psi\rangle_2$ is auxiliary and called cloning. Gisin and Massar [4] proved analytically that representation (3) of the output qubits is optimal, i.e., maximizes the average accuracy of the correspondence between the input and output qubits.

The sequence of actions for cloning qubits is represented in the form of a universal quantum cloning machine. For its operation, it is necessary to prepare preliminary the entangled state of two qubits

$$|\Psi^{\text{prep}}\rangle = C_1|00\rangle + C_2|01\rangle + C_3|10\rangle + C_4|11\rangle \quad (4)$$

by applying unitary operators to zeroth qubits:

$$|\Psi^{\text{prep}}\rangle = R_1(\theta_3)P_{21}R_2(\theta_2)P_{12}R_1(\theta_1)|00\rangle_{12}.$$

Here,

$$R(\theta) = \begin{pmatrix} \cos\theta & \sin\theta \\ -\sin\theta & \cos\theta \end{pmatrix}$$

is the turning operator of a qubit and

$$P_{12}|x, y\rangle = |x, x \oplus y\rangle \quad (5)$$

is the CNOT operator, where $\oplus$ is the modulus-2 summation. The resulting set of equations

$$\begin{aligned} \cos\theta_1\cos\theta_2\cos\theta_3 + \sin\theta_1\sin\theta_2\sin\theta_3 &= C_1, \\ \sin\theta_1\cos\theta_2\cos\theta_3 - \cos\theta_1\sin\theta_2\sin\theta_3 &= C_2, \\ \cos\theta_1\cos\theta_2\sin\theta_3 - \sin\theta_1\sin\theta_2\cos\theta_3 &= C_3, \\ \cos\theta_1\sin\theta_2\cos\theta_3 + \sin\theta_1\cos\theta_2\sin\theta_3 &= C_4, \end{aligned} \quad (6)$$

has the solution

$$\begin{aligned} \cos^2\theta_1 &= \frac{C_2^2 - C_3^2}{1 - 2C_3^2 - 2C_4^2} + \cos^2\theta_3\frac{1 - 2C_2^2 - 2C_4^2}{1 - 2C_3^2 - 2C_4^2}, \\ \cos^2\theta_2 &= \frac{C_3^2 + C_4^2 - \cos^2\theta_3}{1 - 2\cos^2\theta_3}, \end{aligned} \quad (7)$$

Table 1

N	(C_1, C_2, C_3, C_4)	$\cos^2\theta_1$	$\cos^2\theta_2$	$\cos^2\theta_3$	$\mathrm{sign}(\cos\theta_i, \sin\theta_i)$	$\lvert\Psi^{\mathrm{out}}\rangle$
1	$\frac{1}{\sqrt{6}}(2, 1, 1, 0)$	$\frac{1}{2}\left(1 \mp \frac{1}{\sqrt{2}}\right)$	$\frac{1}{2} \mp \frac{\sqrt{2}}{3}$	$\frac{1}{2}\left(1 \mp \frac{1}{\sqrt{2}}\right)$	$(---, +++)$ $(+++, +-+)$	$P_{21}P_{02}P_{10}\lvert\Psi^{\mathrm{in}}\rangle$ $P_{12}P_{20}P_{01}\lvert\Psi^{\mathrm{in}}\rangle$
2	$\frac{1}{\sqrt{6}}(2, 1, 0, 1)$	$\frac{1}{2}\left(1 \mp \frac{1}{\sqrt{5}}\right)$	$\frac{1}{2}\left(1 \mp \frac{\sqrt{5}}{3}\right)$	$\frac{1}{2}\left(1 \mp \frac{2}{\sqrt{5}}\right)$	$(+++, -+-)$ $(+++, +++)$	$P_{21}P_{10}P_{02}\lvert\Psi^{\mathrm{in}}\rangle$ $P_{10}P_{20}P_{02}P_{01}\lvert\Psi^{\mathrm{in}}\rangle$
3	$\frac{1}{\sqrt{6}}(2, 0, 1, 1)$	$\frac{1}{2}\left(1 \mp \frac{1}{\sqrt{5}}\right)$	$\frac{1}{2}\left(1 \mp \frac{\sqrt{5}}{3}\right)$	$\frac{1}{2}\left(1 \mp \frac{1}{\sqrt{5}}\right)$	$(+++, -+-)$ $(+++, +++)$	$P_{12}P_{01}P_{20}\lvert\Psi^{\mathrm{in}}\rangle$ $P_{01}P_{02}P_{20}P_{10}\lvert\Psi^{\mathrm{in}}\rangle$
4	$\frac{1}{\sqrt{6}}(1, 2, 1, 0)$	$\frac{1}{2}\left(1 \pm \frac{1}{\sqrt{5}}\right)$	$\frac{1}{2}\left(1 \mp \frac{\sqrt{5}}{3}\right)$	$\frac{1}{2}\left(1 \mp \frac{2}{\sqrt{5}}\right)$	$(---, +++)$ $(+++, +-+)$	$P_{20}P_{10}P_{01}P_{0\bar{2}}\lvert\Psi^{\mathrm{in}}\rangle$ $P_{21}P_{10}P_{0\bar{2}}\lvert\Psi^{\mathrm{in}}\rangle$
5	$\frac{1}{\sqrt{6}}(1, 2, 0, 1)$	$\frac{1}{2}\left(1 \pm \frac{1}{\sqrt{2}}\right)$	$\frac{1}{2} \mp \frac{\sqrt{2}}{3}$	$\frac{1}{2}\left(1 \pm \frac{1}{\sqrt{2}}\right)$	$(+++, -+-)$ $(+++, +++)$	$P_{12}P_{\bar{2}0}P_{01}\lvert\Psi^{\mathrm{in}}\rangle$ $P_{21}P_{0\bar{2}}P_{10}\lvert\Psi^{\mathrm{in}}\rangle$
6	$\frac{1}{\sqrt{6}}(1, 1, 2, 0)$	$\frac{1}{2}\left(1 \mp \frac{2}{\sqrt{5}}\right)$	$\frac{1}{2}\left(1 \mp \frac{\sqrt{5}}{3}\right)$	$\frac{1}{2}\left(1 \pm \frac{1}{\sqrt{5}}\right)$	$(---, +++)$ $(+++, +-+)$	$P_{01}P_{02}P_{20}P_{\bar{1}0}\lvert\Psi^{\mathrm{in}}\rangle$ $P_{12}P_{0\bar{1}}P_{20}\lvert\Psi^{\mathrm{in}}\rangle$
7	$\frac{1}{\sqrt{6}}(1, 1, 0, 2)$	$\frac{1}{2}\left(1 \pm \frac{2}{\sqrt{5}}\right)$	$\frac{1}{2}\left(1 \mp \frac{\sqrt{5}}{3}\right)$	$\frac{1}{2}\left(1 \pm \frac{1}{\sqrt{5}}\right)$	$(+++, -+-)$ $(+++, +++)$	$P_{12}P_{0\bar{1}}P_{\bar{2}0}\lvert\Psi^{\mathrm{in}}\rangle$ $P_{01}P_{02}P_{\bar{2}0}P_{\bar{1}0}\lvert\Psi^{\mathrm{in}}\rangle$
8	$\frac{1}{\sqrt{6}}(1, 0, 2, 1)$	$\frac{1}{2}\left(1 \mp \frac{1}{\sqrt{2}}\right)$	$\frac{1}{2} \mp \frac{\sqrt{2}}{3}$	$\frac{1}{2}\left(1 \pm \frac{1}{\sqrt{2}}\right)$	$(+++, -+-)$ $(+++, +++)$	$P_{21}P_{02}P_{\bar{1}0}\lvert\Psi^{\mathrm{in}}\rangle$ $P_{12}P_{20}P_{0\bar{1}}\lvert\Psi^{\mathrm{in}}\rangle$
9	$\frac{1}{\sqrt{6}}(1, 0, 1, 2)$	$\frac{1}{2}\left(1 \pm \frac{1}{\sqrt{5}}\right)$	$\frac{1}{2}\left(\mp\frac{\sqrt{5}}{3}\right)$	$\frac{1}{2}\left(1 \pm \frac{2}{\sqrt{5}}\right)$	$(+++, -+-)$ $(+++, +++)$	$P_{21}P_{\bar{1}0}P_{0\bar{2}}\lvert\Psi^{\mathrm{in}}\rangle$ $P_{20}P_{10}P_{0\bar{1}}P_{0\bar{2}}\lvert\Psi^{\mathrm{in}}\rangle$
10	$\frac{1}{\sqrt{6}}(0, 1, 1, 2)$	$\frac{1}{2}\left(1 \pm \frac{1}{\sqrt{2}}\right)$	$\frac{1}{2} \mp \frac{\sqrt{2}}{3}$	$\frac{1}{2}\left(1 \pm \frac{1}{\sqrt{2}}\right)$	$(---, +++)$ $(+++, +-+)$	$P_{21}P_{0\bar{2}}P_{\bar{1}0}\lvert\Psi^{\mathrm{in}}\rangle$ $P_{12}P_{\bar{2}0}P_{0\bar{1}}\lvert\Psi^{\mathrm{in}}\rangle$
11	$\frac{1}{\sqrt{6}}(0, 1, 2, 1)$	$\frac{1}{2}\left(1 \mp \frac{1}{\sqrt{5}}\right)$	$\frac{1}{2}\left(1 \mp \frac{\sqrt{5}}{3}\right)$	$\frac{1}{2}\left(1 \pm \frac{2}{\sqrt{5}}\right)$	$(---, +++)$ $(+++, +-+)$	$P_{21}P_{\bar{1}0}P_{02}\lvert\Psi^{\mathrm{in}}\rangle$ $P_{20}P_{10}P_{0\bar{1}}P_{02}\lvert\Psi^{\mathrm{in}}\rangle$
12	$\frac{1}{\sqrt{6}}(0, 2, 1, 1)$	$\frac{1}{2}\left(1 \pm \frac{2}{\sqrt{5}}\right)$	$\frac{1}{2}\left(1 \mp \frac{\sqrt{5}}{3}\right)$	$\frac{1}{2}\left(1 \mp \frac{1}{\sqrt{5}}\right)$	$(---, +++)$ $(+++, +-+)$	$P_{12}P_{01}P_{\bar{2}0}\lvert\Psi^{\mathrm{in}}\rangle$ $P_{01}P_{02}P_{\bar{2}0}P_{10}\lvert\Psi^{\mathrm{in}}\rangle$

$$\cos^2\theta_3 = \frac{1}{2}\left(1 \pm \frac{1 - 2C_3^2 - 2C_4^2}{1 - 4(C_1^2C_4^2 + C_2^2C_3^2)} \times \sqrt{1 - 4(C_1^2C_4^2 + C_2^2C_3^2) + 8C_1C_2C_3C_4}\right).$$

At the second stage, the quantum cloning machine mixes input qubit (1) with prepared state (4):

$$\lvert\Psi^{\mathrm{in}}\rangle = \lvert\psi\rangle_0\lvert\Psi^{\mathrm{prep}}\rangle = \alpha(C_1\lvert000\rangle + C_2\lvert001\rangle + C_3\lvert010\rangle + C_4\lvert011\rangle) + \beta(C_1\lvert100\rangle + C_2\lvert101\rangle + C_3\lvert110\rangle + C_4\lvert111\rangle), \quad (8)$$

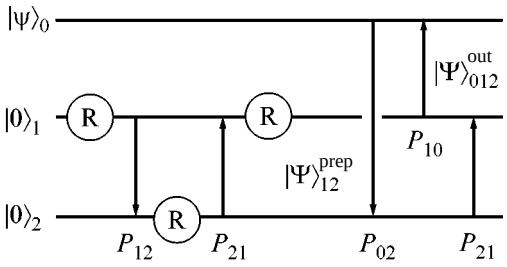

Scheme of the optimized variant of the Buzek–Hillery cloning machine. Only two CNOT operators participating in the production of the output state $|\Psi\rangle_{012}^{out}$ from $|\psi\rangle_0$ and $|\Psi\rangle^{prep}$ involve the input qubit $|\psi\rangle_0$. The arrows point to the goal qubit of the CNOT operator.

so as to obtain optimal state (2) at the output

$$|\Psi^{out}\rangle = |\Phi_0\rangle_{01}|0\rangle_2 + |\Phi_1\rangle_{01}|1\rangle_2$$
$$= \sqrt{\frac{1}{6}}(2\alpha|000\rangle + \beta|010\rangle + \beta|100\rangle \quad (9)$$
$$+ 2\beta|111\rangle + \alpha|011\rangle + \alpha|101\rangle).$$

Comparing Eqs. (3) and (9), we obtain only 12 different combinations of admissible parameters C_1, C_2, C_3, and C_4, for which solution (7) gives the angles for operators $R_1(\theta_1)$, $R_2(\theta_2)$, $R_1(\theta_3)$ (see columns 2–5 in Table 1). The sixth column of Table 1 shows the signs of the rotation angles of $R(\theta)$.

Now, we obtain transformations converting input state (8) (with known C_1, C_2, C_3, and C_4) to output state (9) only in terms of CNOT operators (5). We represent the total transformation operator as

$$|\Psi^{out}\rangle_{xyz} = P(x, y, z)|\Psi^{in}\rangle_{xyz}$$
$$= |p_1(x, y, z), p_2(x, y, z), p_3(x, y, z)\rangle,$$

where $p_i(x, y, z)$ are the logical functions of three Boolean variables.

Let us find this function for the first row of Table 1.

Table 2. Truth table for functions p_i

x	y	z	p_1	p_2	p_3
0	0	0	0	0	0
0	0	1	0	1	1
0	1	0	1	0	1
0	1	1	*	*	*
1	0	0	1	1	1
1	0	1	1	0	0
1	1	0	0	1	0
1	1	1	*	*	*

Note: Asterisks mean arbitrary values.

Since the CNOT operator can realize only linear Boolean functions, only two of eight different combinations are suitable. For one of them, we represent the set of disjunctive normal forms in terms of the Zhegalkin polynomials:

$$p_1 = \bar{x}\&y\&\bar{z} \vee \bar{x}\&y\&z \vee x\&\bar{y}\&\bar{z} \vee x\&\bar{y}\&z = x \oplus y,$$
$$p_2 = \bar{x}\&\bar{y}\&z \vee \bar{x}\&y\&z \vee x\&\bar{y}\&\bar{z} \vee x\&y\&\bar{z} = x \oplus z,$$
$$p_3 = \bar{x}\&\bar{y}\&z \vee \bar{x}\&y\&\bar{z} \vee x\&\bar{y}\&\bar{z} \vee x\&y\&z$$
$$= x \oplus y \oplus z.$$

Then,

$$|\Psi^{out}\rangle_{xyz} = |p_1, p_2, p_3\rangle$$
$$= |x \oplus y, x \oplus z, x \oplus y \oplus z\rangle = P_{21}P_{02}P_{10}|\Psi^{in}\rangle_{xyz}.$$

The other rows in Table 1 are filled similarly. To describe the CNOT operator with inversion, we introduce the notation

$$P_{12}|x, y\rangle = P_{12}|x, \bar{y}\rangle = |x, x \oplus \bar{y}\rangle = P_{12}R_2\left(\frac{\pi}{2}\right)|x, y\rangle,$$

where $R\left(\frac{\pi}{2}\right) = \begin{pmatrix} 0 & 1 \\ -1 & 0 \end{pmatrix}$ is the NOT operation.

The lower half of row 2 in Table 1 describes the operation of the Buzek–Hillery quantum cloning machine [5], whereas the upper half of row 2 describes its optimized variant. It is seen that the output state $|\Psi^{out}\rangle$ can be obtained by three CNOT transformations, only two of which involve the input qubit (see figure). The equatorial qubits of the first row were studied in [6] without discussing the method of their production.

In summary, we obtained the set of unitary transformations producing two copies of an arbitrary input qubit. This transformation is optimal, because it maximizes the average accuracy of correspondence between the input and output qubits. The algorithm allowing one to find any unitary transformation realized by the quantum CNOT operators is proposed on the basis of classical Boolean algebra.

REFERENCES

1. W. K. Wooters and W. H. Zuker, Nature **299**, 802 (1982).
2. V. Buzek and M. Hillery, Phys. Rev. A **54**, 1844 (1996).
3. R. F. Werner, quant-ph/9804001.
4. N. Gisin and S. Massar, Phys. Rev. Lett. **79**, 2153 (1997).
5. V. Buzek, S. L. Braunstein, M. Hillery, and D. Bruβ, Phys. Rev. A **56**, 3446 (1997).
6. Heng Fan, Keiji Matsumoto, and Xiang-Bin Wang, quant-ph/0101101.

Translated by R. Tyapaev